PULSAR WIND TORI AND THE SPIN-KICK CONNECTION

A DISSERTATION
SUBMITTED TO THE DEPARTMENT OF PHYSICS
AND THE COMMITTEE ON GRADUATE STUDIES
OF STANFORD UNIVERSITY
IN PARTIAL FULFILLMENT OF THE REQUIREMENTS
FOR THE DEGREE OF
DOCTOR OF PHILOSOPHY

Chi-Yung Ng
November 2006

I certify that I have read this dissertation and that, in my opinion, it is fully adequate in scope and quality as a dissertation for the degree of Doctor of Philosophy.

(Roger W. Romani) Principal Adviser

I certify that I have read this dissertation and that, in my opinion, it is fully adequate in scope and quality as a dissertation for the degree of Doctor of Philosophy.

(Tom Abel)

I certify that I have read this dissertation and that, in my opinion, it is fully adequate in scope and quality as a dissertation for the degree of Doctor of Philosophy.

(Roger Blandford)

Approved for the University Committee on Graduate Studies.

Abstract

Neutron stars in general have space velocities much higher than their progenitors. This is believed to be the result of momentum kicks imparted during core collapse. However, the nature of the kick remains an open question. Abetted by recent progress in measuring pulsar proper motions and spin orientations, it has become possible to make improved comparison between the pulsar's linear and angular momentum vectors; this places constrains on the kick physics and hence probes the core collapse dynamics. To investigate the spin-kick connection, we improved the Crab pulsar's proper motion measurement using *HST* astrometry with over 6 years of observations. The updated result indicates the pulsar velocity is off the spin axis by $26^\circ \pm 3^\circ$. For the spin vector measurements, recent *Chandra* observations reveal toroidal termination shocks and polar jets in many young pulsar wind nebulae, with the symmetry axes indicating the pulsar spin axes. We developed a procedure for fitting simple Doppler boosted 3-D torus models to the X-ray data. This provides robust and nearly model independent measurements of pulsar spin orientations. All the results suggest correlation between pulsar motions and spin directions. We assemble this evidence for young isolated pulsars and test several scenarios for a birth kick driven by accretion and cooling of the proto-neutron star, where the momentum thrust is proportional to the neutrino cooling luminosity. The simulations include the effects of pulsar acceleration and spin-up. The fit to the pulsar spin and velocity samples suggests a $\sim$10% anisotropy in the neutrino flux is required, with a finite pre-kick spin of $10 - 20$ rad s^{-1}, a kick timescale of $1 - 3$ s and kick-induced spin.

To my dearest CC

Acknowledgements

I would like to express my sincere gratitude to my advisor Roger Romani, for his patient guidance and continuous encouragement through the course of this research work. I would also like to thank Steve Healey for his support and delightful discussion on various topics. A special thanks goes to Matthew Turk for the computer animations.

Contents

List of Tables

List of Figures

Chapter 1

Introduction

1.1 The Nature of Neutron Stars

The first pulsar was discovered in 1967 by Jocelyn Bell at the University of Cambridge (Hewish et al. 1968). Figure 1.1 shows the historical discovery. Although the signal was once considered as from an extraterrestrial civilization, it did not take long to be identified as from a rapidly spinning neutron star (Gold 1968), which had been postulated long time ago by Baade & Zwicky (1934). As illustrated in Figure 1.2, the strong electromagnetic field of the neutron star accelerates particles to very high speed, resulting in radio emission beamed along the magnetic axis. Since in general the magnetic axis does not align with the pulsar spin axis, the radiation beams sweep around like a lighthouse as the neutron star rotates, resulting in a pulsed signal observed on Earth.

Neutron stars are the remnants of core collapse supernova. During the final stage of a massive star's (over $\sim 8\ M_{\odot}$) evolution, light elements are fused into heavier and heavier elements subsequently in the core. This process terminates at iron, which has the lowest energy per nucleon, hence no energy is produced from further nuclear reaction. The stellar structure in this case is shown in Figure 1.3. As more iron is formed in the core, the pressure generated by nuclear reaction can no longer support the star against gravity and core collapse follows. As the central density reaches $\rho_{\rm nuc} \sim 2.8 \times 10^{14}$ g cm^{-3}, the pressure increases rapidly and eventually sufficient to

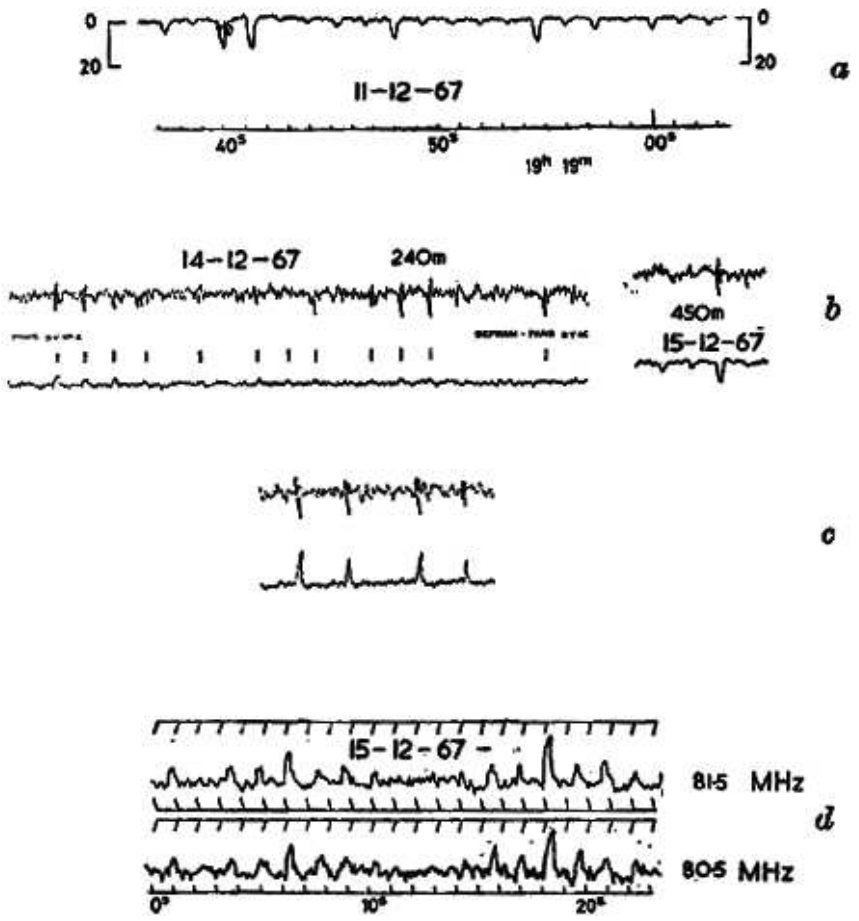

Figure 1.1 Discovery observations of the first pulsar, which is now known as PSR B1929+21 (adapted from Hewish et al. 1968).

'bounce' the inner core and drive a shock wave into the infalling outer core (Shapiro & Teukolsky 1983). This reverses the infall and causes catastrophic explosion, which is known as a Type II supernova explosion. It is an extremely violent event and the energy released is a few times 10^{53} ergs, where $> 99\%$ is in the form of neutrinos and only $< 1\%$ goes to the kinetic energy of the ejectors. After the explosion, the core left behind composed entirely of neutrons. If the core mass is less than $\sim 3M_{\odot}$, it may be supported by neutron degeneracy pressure preventing from further collapse. Thus a neutron star is formed.

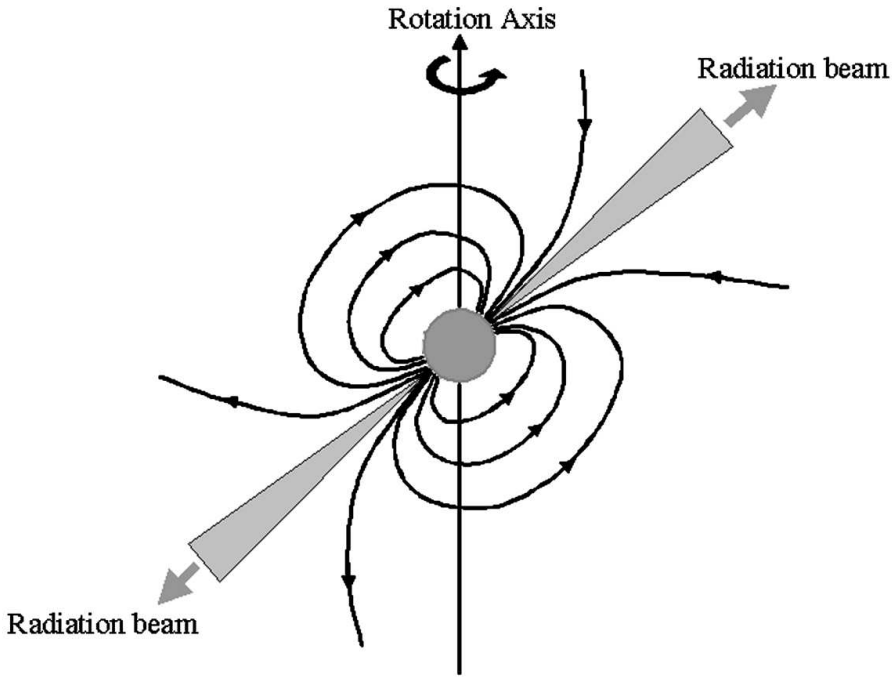

Figure 1.2 The pulsar lighthouse effect.

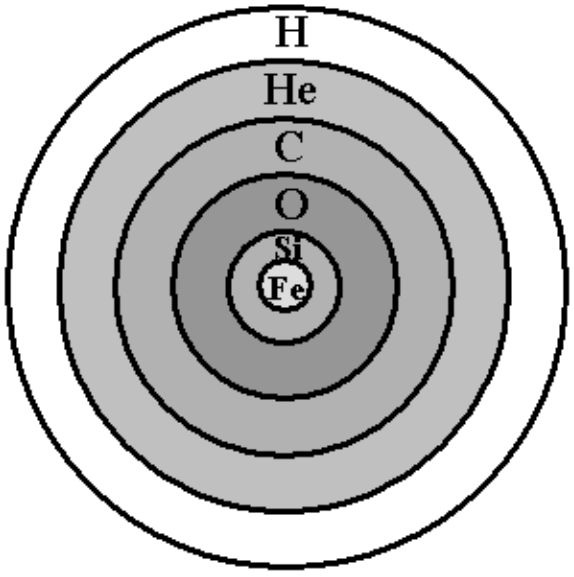

Figure 1.3 Pre-supernova stellar structure (not to scale).

With a mass of $\sim 1.4 M_{\odot}$ and radius of $\sim$ 10 km, neutron star is the most compact object in the universe that has a surface. The dense interior, strong gravity and high magnetic field of neutron star make it an ideal laboratory to study the laws of physics under extreme conditions.

1.2 Neutron Stars Are Fast

Neutron stars are the fastest moving stellar objects, with typical velocities of several hundreds of km per second. Arzoumanian, Chernoff, & Cordes (2002) modeled the pulsar velocity and found that the observed samples are well fitted by a two-component distribution of 90 and 500 km s^{-1}. The result implies that 15% of the pulsars have velocities greater than 1000 km s^{-1}. A recent statistical study of 233 isolated neutron stars' proper motions by Hobbs et al. (2005) suggested a instead unimodal distribution, concluding that the mean 3-D velocity is 400 km s^{-1} (Fig. 1.4). This value is much larger than the typical space velocity of the progenitor stars, which is only a few km per second. In some most extreme cases, pulsar transverse velocities of up to 1600 km s^{-1} have been claimed. One famous example is PSR 2224+65 in the Guitar Nebula. Based on the dispersion measure (DM)-estimated distance, Cordes, Romani, & Lundgren (1993) inferred the pulsar velocity of 1600 ± 370 km s^{-1}. This made it arguably the fastest pulsar that has ever been detected. Another example is PSR B1508+55, whose recent measurements provided the most direct evidence of high pulsar speed. Using the VLBI astrometry, Chatterjee et al. (2005) obtained pulsar parallax and proper motion measurement, thus giving a model independent estimate of the pulsar velocity of 1083^{+103}_{-90} km s^{-1}.

1.3 Pulsar Kicks

For a massive object of $M \simeq 1.4 M_{\odot}$, a neutron star traveling at the very high speed of $\sim 3 \times 10^{-4}\ c$ requires an enormous amount of momentum. It is generally believed that the momentum is deposited in a relatively short timescale, a so-called pulsar kick, during the neutron star birth or shortly after. However, the nature of the kick

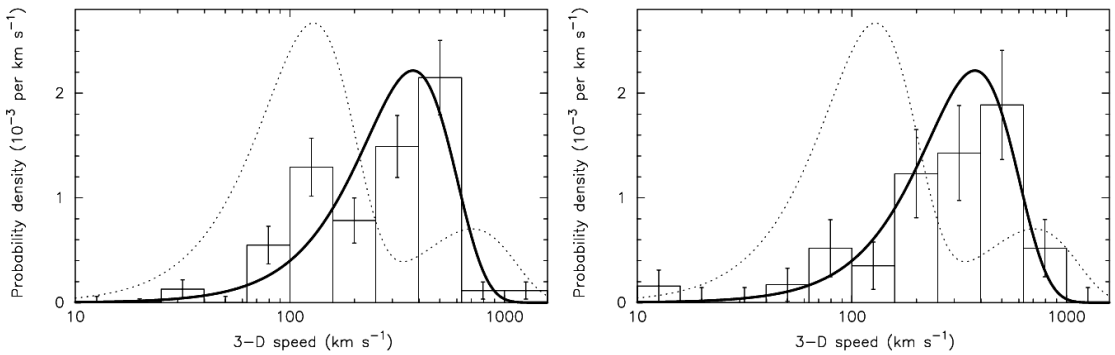

Figure 1.4 The 3D velocity distribution of pulsars, adapted from Hobbs et al. (2005). *Left:* observed 1D velocity distribution; *right:* observed 2D velocity distribution. *Dotted lines:* best-fit result from Arzoumanian, Chernoff, & Cordes (2002); *solid lines*: best-fit result from Hobbs et al. (2005).

remains an interesting open question. Various kick mechanisms have been proposed, including binary disruption, natal kicks and postnatal kicks.

Blaauw (1961) and Boersma (1961) showed that if one star in a binary system undergoes supernova explosion, the disruption of the system could result in ejection of the companion star at the orbital velocity. This is known as the Blaauw mechanism. Attempts have been made to associate the pulsar velocity with binary break-ups (e.g. Radhakrishnan & Shukre 1986; Bailes 1989). Although simulation results suggest that it is viable for kick velocities of a few hundred km per second (Dewey & Cordes 1987; Tauris & Takens 1998; Fryer, Burrows, & Benz 1998), it is very unlikely to obtain the fastest pulsars even under the optimal conditions (Chatterjee et al. 2005).

In the natal kick scenario, the pulsar kick is due to asymmetric mass ejection or neutrino emission during the supernova explosion (Janka et al. 2005). Hydrodynamic simulations suggest that low mode ($l = 1, 2$) convective instabilities during core collapse could lead to global large-scale anisotropies, resulting in ejecta-driven kicks (Scheck et al. 2004) and the pulsar velocity could be above 500 km s^{-1} (Scheck et al. 2004, 2006). However, other 3-D supernova simulations suggest that the core asymmetry leads to asymmetric neutrino emission. This tends to damp out the kick and does not produce neutron star velocities exceeding 200 km s^{-1} (Fryer 2004).

Alternatively, the pulsar kicks could also be driven by the asymmetric neutrino emissions themselves. Arras & Lai (1999a,b) suggest that due to parity violation in weak interactions, the neutrino opacities depends on the magnetic field asymmetrically. The total asymmetry in the neutrino flux is $\sim 0.1 B_{15} \bar{E}_\nu^{-2} + 0.002 B_{15}/T$, where $B = 10^{15} B_{15}\,\mathrm{G}$ is the magnetic field strength, $\bar{E}_\nu$ is the mean neutrino energy in MeV and T is the temperature in MeV. Since most of the energy from the supernova explosion is released in the form of neutrinos, only a few percent asymmetry in the emission is sufficient for a kick velocity of a thousand km per second. However, the above expression indicates that an extremely high magnetic field ($10^{15}\,\mathrm{G}$) is required for the proto-neutron star. It remains unclear how such a high field strength could be archived from the current understanding of the proto-neutron star physics. Pulsar kicks beyond the standard model have also been proposed, including exotic physics such as asymmetric off-resonant emission of sterile neutrinos (e.g. Nardi & Zuluaga 2001; Fuller et al. 2003; Kusenko 2004).

Possible postnatal kick effects include the electromagnetic rocket, which is the asymmetric electromagnetic radiation caused by off-center rotating magnetic dipole (Harrison & Tademaru 1975). As a result, when the neutron star spin down energy is radiated away through electromagnetic braking, a kick is imparted along the spin axis. Lai, Chernoff, & Cordes (2001) showed that the kick depends strongly on the rotation period. In order to achieve the kick velocity of a few hundred km per second, an initial spin period as short as $\sim 1\,\mathrm{ms}$ is required, which makes this model not likely to be feasible.

1.4 Observational Properties and Techniques

As in many astrophysical problems, comparison to observations is the best way to constrain the models. The pulsar velocity distribution has posed some energetic constraints on the kick problem already. If there are any additional correlations between the velocity and other observational properties, this could provide further probes to the kick physics. Although previous studies concluded no correlation between pulsar velocity and magnetic moment, nor between velocity and spin periods

(Cordes & Chernoff 1998), Spruit & Phinney (1998) argued that for long duration kicks with timescale of seconds, the pulsar spin and velocity vectors tend to align due to rotational averaging. The alignment angle between the two vectors is thus an important observable that relates to the kick timescale and possibly help to rule out some of the models (Lai et al. 2001). In order to test this idea, one observational challenge is to obtain precise measurements of the two vector quantities.

1.4.1 Velocity Measurements

The common techniques of pulsar velocity measurement include interstellar scintillation, pulsar timing and astrometry. When radiation passes through interstellar plasma, the random fluctuations of electron density result in scintillation. This gives the information about pulsar velocity relative to the interstellar plasma (e.g. Ord, Bailes, & van Straten 2002). However, in most cases, only a 1-D speed is obtained and there is no information about the velocity direction.

For 'quiet' pulsars with small timing irregularities, the proper motion can also be obtained from accurate timing. As the Earth moves around the Sun, the light travel time from the pulsar varies. This results in periodic timing residual and the pulsar proper motion is obtained by fitting the residual amplitude (e.g. Fig. 1.5). Recently Hobbs et al. (2004) introduced a 'whitening' technique which allows the timing method to be applied even in the presence of some timing noise. Some recent analyses of pulsar timing observations obtain several dozen useful proper motions (Hobbs et al. 2004; Zou et al. 2005).

Among the proper motion measurement techniques, astrometry usually gives the most accurate results. In some cases, parallaxes are obtained at the same time, together these provide model independent measurements of the pulsar space velocity. For a pulsar at 1 kpc with velocity 100 km s^{-1}, its proper motion is 20 mas yr^{-1}. Recent progress in phase referenced VLBI astrometry provides by far the most precise measurement down to submilliarcsecond level (Brisken et al. 2002; Chatterjee et al. 2005). Hence for a radio bright pulsar within $2-3$ kpc, an accurate proper motion measurement could be obtained within a year or two. As an alternative,

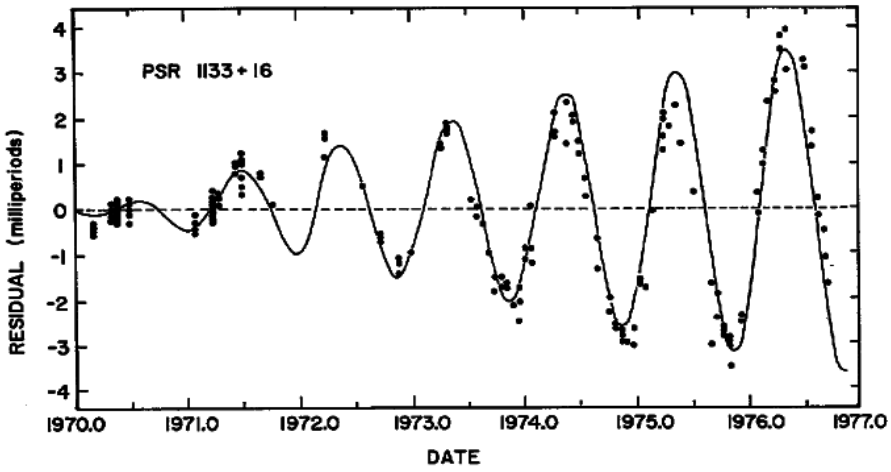

Figure 1.5 Timing residuals for PSR 1133+16, adapted from Helfand, Taylor, & Manchester (1977).

optical astrometry with the *Hubble Space Telescope (HST)* can also provide proper motion measurements for young neutron stars with optical counterparts. With its superb resolving power of a few percent of an arcsecond, precise proper motions may be measured with a time base of just a few years (Mignani, Caraveo, & de Luca 2000; Ng & Romani 2006).

In some cases when none of the above methods is available, a very rough proper motion direction may still be inferred using the offset from the supernova remnant (SNR), provided that there is an association and the SNR has a well-defined geometrical center. Moreover, if there is an age and distance estimate for the system, a quantitative estimate of the space velocity may be made (e.g. Romani & Ng 2003). Finally, in a few pulsar wind nebula (PWN) systems, the X-ray morphology such as bow shock and trailing plerion can indicate the pulsar velocity direction too. Famous examples includes IC 443 (Gaensler et al. 2006), N157B (Wang et al. 2001) and G359.23−0.82 ('the mouse' Gaensler et al. 2004). The cometary trails observed in these systems are believed to be elongated PWNe due to the pulsar's proper motion.

1.4.2 Spin Measurements

As compare to the proper motion measurements, it is much more difficult to obtain the pulsar spin vectors, which are not direct observables. A classic approach is from the radio polarimetric observations. Adopting the rotating vector model, the most rapid sweep of the intrinsic polarization angle corresponds to the closest approach of the magnetic field to the line of sight. That is the point where the spin axis and the line of sight are in the same plane as the curved magnetic field line. Hence the projected pulsar spin direction on the sky plane is inferred after careful correction for the interstellar Faraday rotation. As an example, the radio polarization profile of the Vela pulsar is shown in Figure 1.6.

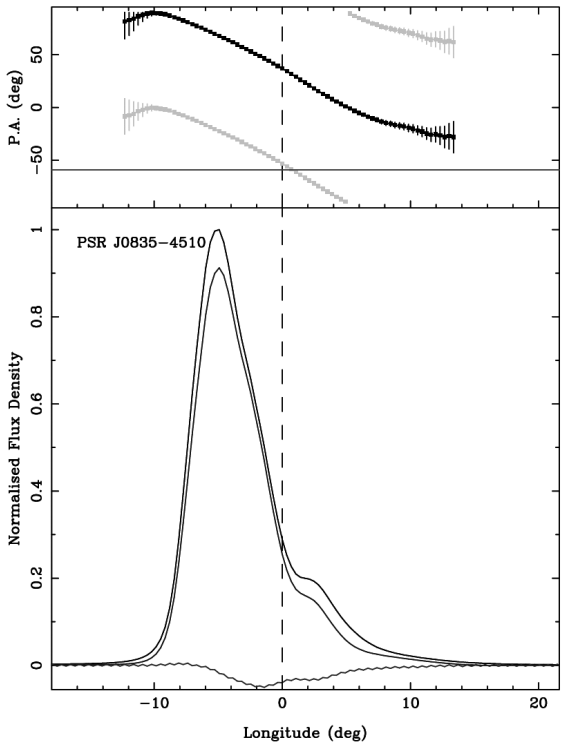

Figure 1.6 Polarization profile of the Vela pulsar, adapted from Johnston et al. (2005).

Despite early claims of no correlation between the polarization angle and proper motion, likely due to large systematic uncertainties, recent improved polarization

studies have provided convincing statistical evidence for the alignment between the two (Johnston et al. 2005). However, this method is still highly phenomenological and suffers major systematic uncertainties. Moreover, the two emission modes have PAs perpendicular to each other, resulting in an intrinsic $\pi/2$ ambiguity in the measurement.

The discovery of pulsar jets and toroidal termination shocks in many PWNe by the *Chandra X-ray Observatory (CXO)* shines new light on the problem. Two finest examples are the Crab and Vela pulsars. The X-ray observations reveal their jet and torus structure, with the symmetry axes indicating the spin orientations (Weisskopf et al. 2000; Pavlov et al. 2000; Helfand, Gotthelf, & Halpern 2001). More importantly, alignment between pulsar spin and proper motion is claimed in both cases (Caraveo & Mignani 1999; Pavlov et al. 2000). As this is very unlikely to be happened by chance, Lai et al. (2001) discussed the implications for constraints of the kick physics.

For a vector comparison between the spin and velocity on the plane of the sky (the radial velocity is not measurable), the pulsar initial spin periods is also needed, which remains a very difficult parameter to estimate. Currently, only a handful of pulsars that have initial spin period estimates (e.g. Table 7 in Faucher-Giguère & Kaspi 2006). As it happens, most of these have PWN structure indicating their spin orientations, but many do not have a precise proper motion measurement.

1.5 Outline

As motivated by the cases of the Crab and Vela pulsars, this study investigate the kick problem from a kinematic point of view, with particular focus on the spin-kick connection. We first improve the measurements of pulsar proper motions and spin orientations, then we study the kick physics with a simple kick model and constrain the parameters using the observation data.

In Chapter 2, we will discuss the improved proper motion measurement of the Crab pulsar, based on *HST* exposures spanning over 6 years. For spin measurement, we have developed a pulsar wind torus fitting technique which will be described in

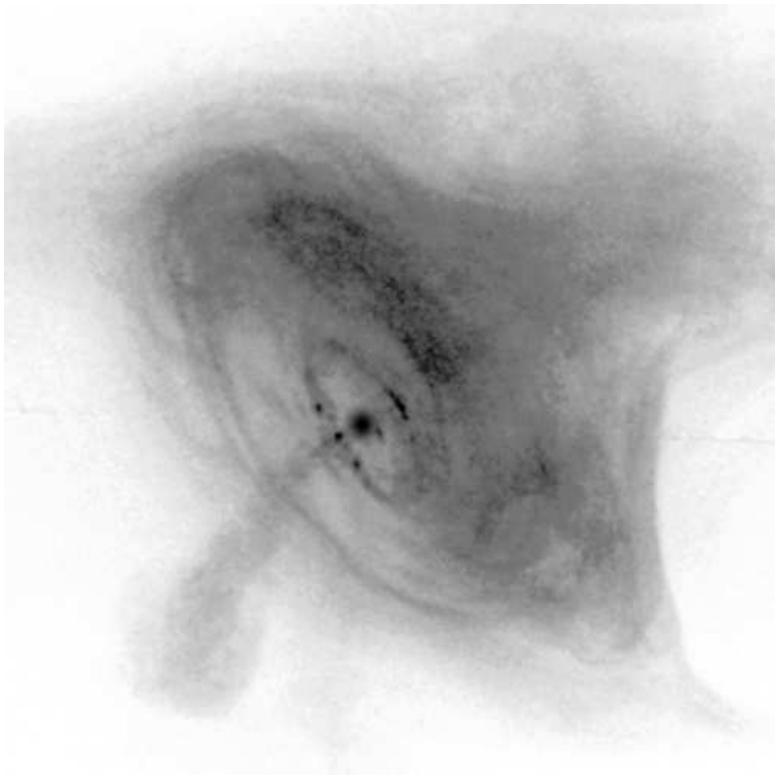

Figure 1.7 *Chandra* ACIS image of the Crab pulsar and its PWN. (Credit: NASA/CXC/ASU/J. Hester et al.)

Chapter 3. This method provides a robust and nearly model independent tool to obtain pulsar spin orientation from the X-ray data. As an application, more pulsar spin measurement will be discussed in Chapter 4. With the improve data sample, we try to constrain the kick physics. Simulations of simple neutrino kick scenario will be discussed in Chapter 5. Finally, we will address the conclusions and outlook about the places for future improvements in Chapter 6. Related works on PWN observations and proper motion measurements of PSRs B1706−44 and J0538+2817 are presented in Appendices A and B.

Chapter 2

Proper Motion of the Crab Pulsar Revisited

This chapter is based on "Proper Motion of the Crab Pulsar Revisited", C.-Y. Ng & Roger W. Romani 2006, ApJ, 644, 445.

2.1 Introduction

Pulsars are fast-moving objects with space velocities up to an order of magnitude larger than their progenitors. It has long been suggested that this is the result of a momentum kick at birth. One way to probe the kick physics is to compare the pulsar's velocity and spin axis orientations. The kick timescale is constrained by the alignment between the two vectors. For the Crab pulsar, stunning images from the *Chandra X-ray Observatory* reveal the torus-like pulsar wind nebula. The symmetry axis indicates the 3-D orientation of the pulsar spin axis, and more interestingly, suggests an alignment with the proper motion. Ng & Romani (2004) fitted the pulsar wind torus and derived a quantitative measurement of the spin axis at position angle (PA) 124.°0 or 304.°0 $\pm$ 0.°1. In contrast, the pulsar's proper motion is not as well measured. Previous works by Wychoff & Murray (1977) and Caraveo & Mignani (1999) (hereafter CM99) have large uncertainties. The former examined photographic plates over 77 years and obtained the result of 13 ± 4 mas yr^{-1}, at

PA $293^\circ \pm 18^\circ$. CM99 performed relative astrometry on the Wide Field Planetary Camera 2 (WFPC2) images from the *Hubble Space Telescope* (*HST*) and found a proper motion of $\mu_* = 18 \pm 3$ mas yr^{-1} at $292^\circ \pm 10^\circ$ using dataset spanning 1.9 years.

The high angular resolution cameras on board the *HST* make it possible to determine the pulsar proper motion in a short period of time. In the past few years, many new observations of the Crab pulsar have been collected with the telescope. The *HST* data archive in fact contains WFPC2 Crab images spanning some 7 years, and new Advanced Camera for Surveys (ACS) images are now being taken. Also, recent studies have improved our understanding of the WFPC2 camera's geometric distortions (Anderson & King 2003, hereafter AK03). Thus, with a longer timebase and improved calibration, this study aims to update CM99's result on the proper motion of the Crab pulsar.

2.2 The Datasets

Using *HST*/WFPC2 images, relative astrometry can be made to an accuracy of $0\farcs005$ for objects on the same chip (Baggett et al. 2002, section 5.4). We have searched the Multi-mission Archive at Space Telescope (MAST) and found more than 70 WFPC2 observations of the pulsar from 1994 to 2001, making this the best instrument for the this study. However, these images were taken using a variety of optical filters, which have slightly different plate scales and geometric distortion. Therefore, we restrict our analysis to a single one. The F547M filter is the best choice, since it has the most observations and the longest time span of 7 years. Table 2.1 lists all the observations with this filter; epochs with similar pointing parameters are grouped. Obs 8a, which is observed with the POLQ filter, is also listed in the table as it is used in CM99. We have included the first ACS observation in the table as well.

Table 2.1 WFPC2 observations of the Crab pulsar with the F547M filter.

Obs.	Date	Exp. (s)	Detector	# Ref. Stars	Roll Angle	Chip x	Chip y	Group
1	1994-03-09	2000	WF2	11	-116.8	463	160	
2	1995-01-06	1600	WF3	8	-51.2	163	130	1
3	1995-01-06	2000	WF3	7	-51.2	151	118	1
4	1995-08-14	2000	PC	5	-48.7	470	371	
5	1995-11-05	2000	PC	2	-25.3	340	300	
6	1995-12-29	2000	PC	4	128.7	297	600	2
7	1996-01-20	2000	PC	4	128.7	297	601	2
8	1996-01-26	2000	PC	4	128.7	297	603	2
8a	1996-01-26	2000	WF2	13	-153.3	495	546	
9	1996-02-01	2000	PC	4	128.7	297	601	2
10	1996-02-22	2000	PC	4	128.7	297	602	2
11	1996-04-16	2000	PC	4	128.9	266	599	2
12	2000-02-06	2200	WF3	15	-47.3	373	273	3
13	2000-02-15	2200	WF3	15	-47.3	372	273	3
14	2000-02-26	2200	WF3	15	-47.3	371	271	3
15	2000-03-07	2200	WF3	15	-47.3	372	272	3
16	2000-03-17	2200	WF3	15	-47.3	373	273	3
17	2000-08-07	2300	WF4	6	-136.7	63	136	4
18	2000-08-18	2400	WF4	6	-136.7	63	136	4
19	2000-08-29	2400	WF4	6	-136.7	64	136	4
20	2000-09-09	1837	WF3	8	132.7	217	342	5
21	2000-09-21	2071	WF3	8	132.7	219	342	5
22	2000-10-01	1854	WF3	8	132.7	217	342	5
23	2000-10-12	2400	WF3	8	132.7	217	341	5
24	2000-10-23	2007	WF3	8	132.7	217	342	5
25	2000-11-15	1927	WF3	8	132.7	217	342	5
26	2000-11-25	2300	WF3	8	132.7	226	334	5
27	2000-12-06	2100	WF3	8	132.7	217	340	5
28	2000-12-18	2100	WF3	15	-47.3	372	274	6
29	2000-12-28	2100	WF3	15	-47.3	372	273	6
30	2001-01-09	2400	WF3	15	-47.3	378	275	6
31	2001-01-19	2400	WF3	15	-47.3	388	276	6
32	2001-01-30	2400	WF3	15	-47.3	388	276	6
33	2001-02-10	2400	WF3	15	-47.3	384	278	6
34	2001-02-21	2400	WF3	15	-47.3	388	276	6
35	2001-03-04	2400	WF3	15	-47.3	389	275	6
36	2001-03-15	2400	WF3	15	-47.3	390	275	6
37	2001-03-26	2400	WF3	15	-47.3	390	275	6
38	2001-04-06	2400	WF3	15	-47.3	390	275	6
39	2001-04-17	2400	WF3	15	-47.3	390	276	6
40	2001-04-19	2400	WF2	6	-137.6	133	41	
41	2003-08-08	2200	ACS	14	-92.6			

2.3 Data Reduction

To start, we attempted to reproduce the CM99 results. We used the same images (obs 1, 4 & 8a) and the same reference stars and attempted to follow their analysis as closely as possible. The data retrieved from the MAST are processed with the On-The-Fly Reprocessing (OTFR) system to ensure up-to-date calibration. The task

`crrej` is employed to remove the cosmic rays and co-add images for each epoch. Geometric distortion is then corrected by remapping the images, using the task `wmosaic` in the STSDAS package. Coordinates of the pulsar and the four reference stars are obtained from a 2-D Gaussian fit with the task `fitpsf` in IRAF. Finally, the best-fit positions are rotated according to the roll angles in image headers and the frames are offset to align the reference stars with obs 1.

By following CM99's procedure in this way, we obtain

$$\mu''_\alpha \equiv \mu_\alpha \cos\delta = -11 \pm 15 \text{ mas yr}^{-1}, \ \mu_\delta = 2.0 \pm 90 \text{ mas yr}^{-1},$$

i.e. no significant detection of the proper motion. This is obviously inconsistent with CM99. The extremely large uncertainty is caused by star 1, which suffers a relative shift of 2 pixels from obs 1 to obs 8a. Comparison with other field stars shows that the shift is systematic and due to large changes in the field distortion caused by the extra polarizer filter POLQ used in obs 8a. This underscores the fact that different filters are incompatible and should not be compared directly without filter-specific distortion maps. If we exclude frame 8a and fit only the first two images, the star residuals after frame alignment are 7.6 mas. With four reference stars, the formal statistical uncertainty on frame alignment is $\sim$ half as large, but as systematic distortions dominate the alignment error, the pulsar astrometry is no better than the 7.6 mas level. We feel that this is a more realistic assessment of the astrometric errors in these data than the CM99 values. This gives $\mu''_\alpha = -10.2 \pm 4.9$ mas yr^{-1}, $\mu_\delta = 2.0 \pm 5.6$ mas yr^{-1} a rather low significance detection of the Crab proper motion. In any case, we see no way to avoid large errors in star astrometry and frame registration with simple Gaussian fits to only a few star images.

2.3.1 Our Approach

Since many F547M frames are now available, we can make a more careful assessment of the proper motion, restricting to a single filter configuration and examining similar telescope pointings. Also, we should avoid performing distortion corrections with

the task `wmosaic`, which degrades the resolution by re-sampling the image. Instead, we followed an approach similar to Kaplan, van Kerkwijk, & Anderson (2002) that involves no re-sampling of the data. Star coordinates are first measured on the chip reference frame. These pixel positions are then corrected for geometric distortion, followed by the standard transformation for frame alignment.

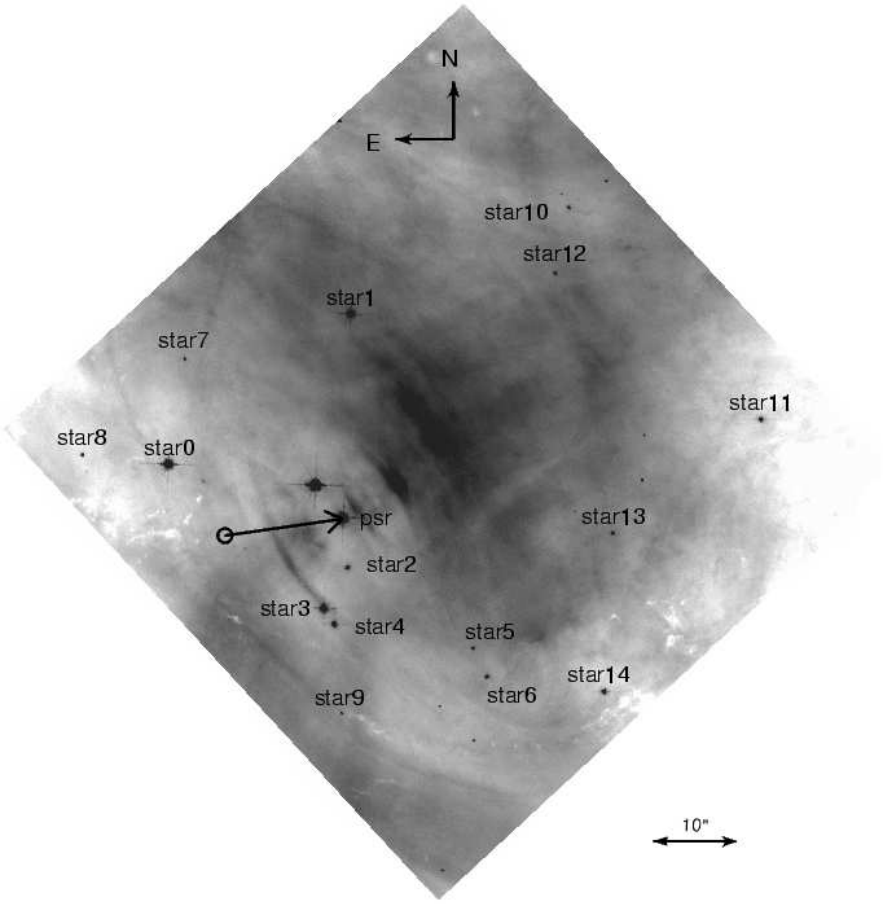

Figure 2.1 Co-added WF3 images of group 6 observations. The Crab pulsar and 15 reference stars are labeled. The arrow indicates the best-fit pulsar proper motion since birth, with the uncertainty in the birth site represented by the circle.

As labeled in Figure 2.1, 15 stars with high signal-to-noise ratio (S/N) are chosen as reference points. After cosmic ray removal, images of the same epoch are co-added. Then we employed 2-D Gaussian fit with the task `fitpsf` for centering the objects. We found that the pulsar position is not sensitive to the knot at the SE,

since the point source is much brighter. More generally, the nebular background does not appear to significantly affect the astrometry of the bright stars used here, as tested by varying the extraction regions and background fitting algorithm. On the other hand, the pulsar and a few brightest stars are saturated in the exposures. To test whether the saturation affects our Gaussian fit astrometry, we attempted fitting with saturated pixels masked using the Data Quality Files. We found that the changes to individual star positions are much smaller than the estimated errors in our astrometry (§ 2.3.4) and the residuals in frame alignment are in fact slightly lower without masking. Therefore, we did not mask out any pixels in the fit.

2.3.2 Distortion Correction

After the star coordinates are obtained, we must correct for geometric distortion before frame alignment. The tasks `metric` and `wmosaic` in the STSDAS package are commonly used for geometric distortion correction of the WFPC2. However, in addition to the degradation resulting from re-sampling, the distortion corrections are based on Gilmozzi, Ewald, & Kinney (1995), with an rms residual of ∼10 mas. We clearly need higher accuracy for the proper motion measurement. The recent study of AK03 gives a much better solution with accuracy better than 0.02 WF pixels, i.e. 2 mas. It is argued in Kaplan et al. (2002) that the chromatic variation in the distortion is modest for filters at similar wavelengths, so we applied the AK03 solution for the F555W filter in our analysis. The pixel coordinates are first corrected for the 34th row defect (Anderson & King 1999), then the geometric distortion is removed using the third-order polynomials in AK03.

2.3.3 Frame Alignment

To proceed to relative astrometry, each frame is aligned to a common sky position, measuring four fitting parameters (scale, x-, y-shift and rotation). The reference star positions and proper motions (which even for typical $\sim$ 10 km s^{-1} local Galactic velocity dispersion can be detectable over the full data span) are not, of course known *a priori*, and so are also determined in the global fit to the data frames.

All parameters are fitted simultaneously by global χ^2 minimization. If we attempt to use all F547M data (Table 2.1), we find large reference star residuals for frames with different roll angles and when the pulsar is present in different camera chips (Fig. 2.2). This is almost certainly due to residual uncorrected geometric distortion. Thus in order to minimize the systematic errors, we have to further limit the fit to a subset of the data with similar pointing parameters. Groups 3 & 6 are the place to start, since they have identical roll angles and contain most of the frames. However, we also included group 1 in the fit since it has a similar roll angle with groups 3 & 6 and the very long (6 year) time base can help to overwhelm the residual distortion errors from the somewhat different chip placement of the pulsar in these frames.

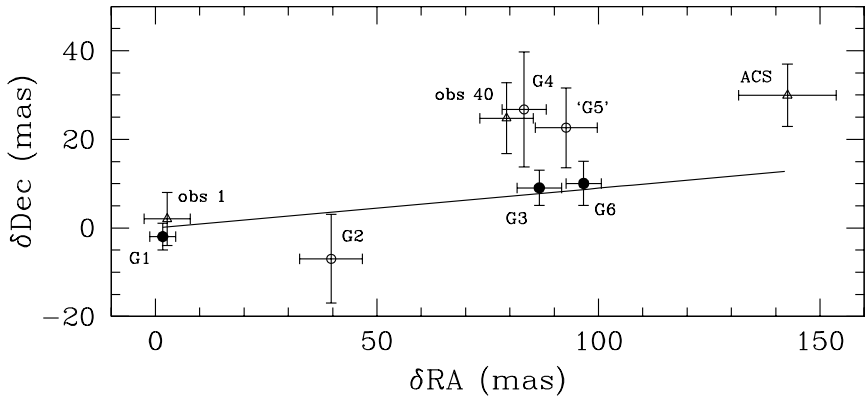

Figure 2.2 Position of the Crab pulsar relative to observation 2. The reference star positions and proper motions are fitted from groups 1, 3, and 6, while individual frames are aligned with observation 2. Filled circles: groups 1, 3, and 6; open circles: groups 2, 4, and '5' (the mean of observations 21, 23, and 25 is shown); open triangles: observations 1, 40, and 41. The best-fit pulsar proper motion (solid line) is fitted to the filled-circle data only. The other epochs have large unmodeled geometric distortions that affect the relative pulsar astrometry, as shown (see text). Note, however, that these epochs do confirm the general proper motion trend.

2.3.4 Sources of Error

Before discussing the results, it is important to have a quantitative estimate of the uncertainties in the star astrometry. The main sources of error are star position

measurement and residual geometric distortion.

The formal statistical errors in measuring the star centroids are essentially negligible (< 1 mas) since all the stars have high S/N. Also, as noted above, the results are quite insensitive to the background fitting method. Following CM99, we used different aperture sizes, but found that the best-fit positions only varied by 1 mas for apertures $> 3\times$ the full width half-maximum (FWHM). Of course the true errors in star centroiding are much larger than that suggested by the centering algorithm χ^2, since the PSF is substantially under-sampled by the WFPC2 pixels, giving large Poisson fluctuations at the peak. The true astrometric uncertainty is in fact best measured by comparing star pixel coordinates among group 6 frames, since these (many) frames have an identical telescope pointing and thus residual image distortion cannot introduce position shifts between frames. This exercise gives an rms variance in each coordinate of 4.3 mas, our best estimate of the single star centroiding error.

Simple Gaussian fit could in principal dominate this error, so we tried a different centering method using Tiny Tim (Krist 1995) simulated point-spread functions (PSFs). The results are very similar to the Gaussian astrometry. For example comparison of obs 35 & obs 37 shows rms scattering of 3.2 & 4.6 mas for Gaussian and PSF fit respectively. This suggests that Gaussian fits do not significantly degrade the accuracy of the centroiding of these bright stars (although they do not, of course capture systematic PSF-dependent centroid shifts).

As mentioned, a simple fit to all of the F547M data shows that frames with different telescope pointings do not match well. This implies that some residual geometric distortion remains even after applying the AK03 solution. Of course, we do not expect to recover their full accuracy since our dataset is taken with another filter. Also, their study used an effective PSF (ePSF) determined from the actual exposures (of ω Centauri). Since the centroiding depends on the PSF used, the distortion map is specific to a particular ePSF scheme. Unfortunately, the Crab frames contain too few stars to build up a local ePSF.

To probe the level of astrometric error introduced by the residual distortion, we compared star positions measured from exposures with different roll angles. As an

example, we consider obs 23 (from group 5) & obs 37 (from group 6), which have a $\sim$180° relative rotation. Superposition of the two frames gives a rms variance of 10 mas for the 8 common reference stars. However, we noticed that some bright stars exhibit large systematic residuals. In particular, star 0 & star 3 are shifted for 20 & 15 mas respectively in the y-direction after alignment. A comparison of the pulsar positions in the two exposures also yields a similar amount of shift in the same direction. Given that the brightness of the pulsar is comparable to star 0, we speculate that the systematic error is due to some fine structures in the PSFs of the bright stars. To further characterize the shift, we performed the same analysis on other frames between the two groups and found that the pulsar, star 0 & star 3 always have large systematic residuals in the same direction. To check if a realistic model PSF fitting could improve the results (as the position-dependent model PSF is plausibly closer to the true PSF), we repeated the same process with centroiding using the Tiny Tim simulated PSFs. However, comparison of obs 23 with obs 37 gives a larger rms variance of 14 mas and the systematic shifts in the pulsar, star 0 & star 2 persist. Clearly the detailed structures that cause systematic errors of the bright stars are unmodeled by the simulated PSFs. We conclude that Tiny Tim PSF fit is not an improvement over Gaussian fit for our case.

On the other hand, comparison of frames in the same group shows small variance in the star positions, although the offset in telescope pointings are as large as 20 pixels within a group. This argues against saturation or PSF under-sampling effects dominating the shifts and suggests that the position-dependent PSF distortions are more moderate. Furthermore, AK03 found that their distortion solution is stable over a period of years and the orbital effects such as jitter and breathing induce scale variations less than 10^{-4} (i.e. $<$1 mas for our relative star positions). We therefore suspect that the large roll angle-dependent residuals are due to non-axisymmetric structures in the bright star PSFs, not modeled in the Gaussian or Tiny Tim fits. However, group 1 is at a very similar roll angle to groups 3 & 6 and should therefore avoid the relative shift found in the bright-star PSFs. We thus included it in our fit, even though it may contain residual position-dependent PSF distortions. We estimated this residual distortion by discarding star 0 in the frame comparison. This

reduces the scatter to 7.6 mas when obs 23 is compared with obs 37. After removing the astrometric error in quadrature, this implies that residual distortion contributes ∼6 mas to the uncertainty when the AK03 correction is applied to Gaussian-fitted star positions under the F547M filter. To conclude, groups 1, 3 & 6 have sufficiently similar telescope pointings such that the residual distortion is minimal; group 5 is at a very different roll angle and groups 2 & 4 use different chips. They thus have large, uncorrected residual distortions and we must exclude them from the fit.

To remove this residual distortion, the full effective PSF approach (Anderson & King 2000) would be required. Unfortunately, the dearth of field stars makes it difficult to build a useful PSF library. We therefore proceed with Gaussian fits to seek the best current results. However, as this study was being completed, we learned that Anderson and colleagues are attempting a full ePSF study of the Crab field and we expect that this can provide additional astrometric accuracy.

2.4 Results

Figure 2.2 shows the pulsar positions at different epochs, with the star positions and proper motions fixed from the groups 1, 3 & 6 fit, and frame registration determined by standard transformations of individual epochs. The uncertainties are given by rms scatterings of the reference star coordinates in the corresponding epoch. In each case we re-scale the errors accounting for the number of degrees of freedom absorbed by the fitted parameters. Since there are only two independent frames in group 1, a substantial fraction of the position uncertainty is absorbed by the reference star proper motion terms in the fit. In addition, for group 1 the pulsar position on the chip differs substantially (although the observation roll angle is similar) so residual geometrical distortions almost certainly affect the pulsar astrometry, as described above. Thus the re-scaled statistical errors (*solid error flags*) are likely significantly too small. So we add, in quadrature, the 4.3 mas centroiding error and the 6 mas residual distortion error estimated above for a more realistic 7.4 mas error estimate (*dashed error flags*). This gives a more conservative error in the proper motion fit.

Linear regression is employed to determine the pulsar's proper motion. The

best-fit result

$$\mu''_\alpha = -15.0 \pm 0.8 \text{ mas yr}^{-1}, \ \mu_\delta = 1.3 \pm 0.8 \text{ mas yr}^{-1}$$

is plotted by the solid line in the graphs. While μ''_α is consistent with previous studies, μ_δ is about 5 times smaller, resulting in a significantly different position angle for the proper motion. (For reference, we obtained $\mu''_\alpha = -15.8 \pm 0.3$ mas yr^{-1}, $\mu_\delta = 1.4 \pm 0.3$ mas yr^{-1} if the statistical errors of group 1 are used).

We also checked the fit with only group 3 & 6 data, since residual distortion cannot affect our astrometry in these images. For this restricted data set, the proper motion

$$\mu''_\alpha = -10.9 \pm 2.2 \text{ mas yr}^{-1}, \ \mu_\delta = 1.0 \pm 2.0 \text{ mas yr}^{-1}$$

is shown by the dotted line in Figure 2.3. The errors are of course larger with the shorter time base, but systematic errors *cannot* contribute significantly. Note that μ''_α differs by $\sim 1.7\sigma$. μ_δ is not significantly changed, and still differs substantially from previous estimates. The best-fit pulsar proper motions (two years' position offsets) with the associated uncertainties are shown by dashed, solid and dotted arrows in Figure 2.3 for CM99 and the two above cases, respectively. The proper motion directions in our two fits are in excellent agreement, with a posiiton angle $275^\circ \pm 3^\circ$. For comparison, the CM99 best-fit value (which is similarly uncorrected to the local standard of rest) lies 5.7σ away, although given their much larger errors the measurements only disagree at the 1.6σ level.

To convert the proper motion to its local standard of rest, Galactic rotation and solar peculiar motion corrections have to be applied. Here a flat rotation curve is assumed, with $\Omega_0 = 220$ km s^{-1} and $R_0 = 8.5$ kpc (Fich, Blitz, & Stark 1989) and the solar constants are taken to be 10 ± 0.36, 5.25 ± 0.62 & 7.17 ± 0.38 km s^{-1} (Dehnen & Binney 1998). Applied to our group 1, 3 & 6 fit, this gives our final result of

$$\mu''_\alpha = -14.7 \pm 0.8 \text{ mas yr}^{-1}, \ \mu_\delta = 2.0 \pm 0.8 \text{ mas yr}^{-1}$$

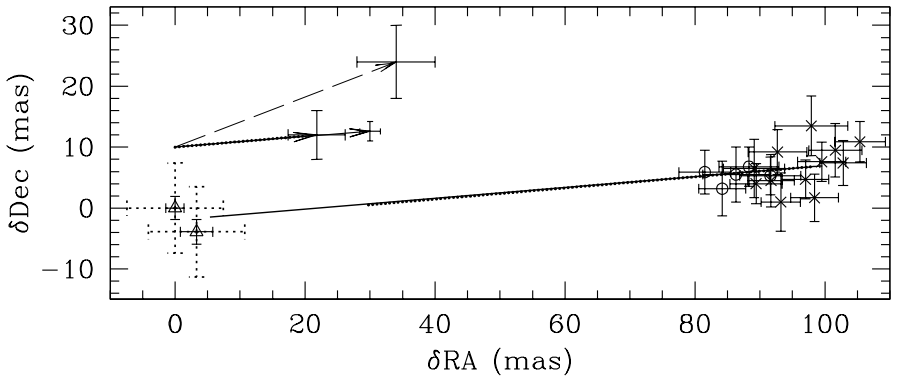

Figure 2.3 Best-fit proper motion of the Crab pulsar. The pulsar's positions relative to observation 2 are plotted for different epochs (open triangle: group 1; open circle: group 3; cross: group 6). The solid and dotted error flags of group 1 are statistical and systematic errors as discussed in the text. The best-fit proper motions for the group (1, 3, 6) and (3, 6) fits are shown by the solid and dotted lines, respectively; the length represents the motion from observation 2 (MJD 49723) to observation 39 (MJD 52016). The dashed, solid, and dotted arrows indicate the best-fit pulsar motions in 2 years for CM99 and our two fits, respectively, all without Galactic rotation and solar motion corrections.

or

$$\mu_* = 14.9 \pm 0.8 \text{ mas yr}^{-1} \text{ at PA } 278^\circ \pm 3^\circ.$$

At the nominal distance of 2 kpc, this gives the pulsar's space velocity as 140 ± 8 km s^{-1}. For reference, the group 3 & 6 solution has $\mu_* = 10.8 \pm 2$ mas yr^{-1}, at PA $279^\circ \pm 10^\circ$ in its local standard of rest.

2.5 Discussion

Our study, using WFPC2 observations spanning > 6 years, improved geometric distortion corrections and a more realistic assessment of errors, suggests a new value for the Crab pulsar's proper motion differing from that of previous studies. We have not been able to reproduce the estimate of CM99. We believe that the errors were substantially underestimated in their proper motion study which used only four stars

in three data frames spanning 1.9 years. We must conclude that our new position angle measurement $278^\circ \pm 3^\circ$ supersedes this earlier estimate.

This is important, since the apparent alignment of the Crab pulsar's proper motion and spin axis (as measured from the pulsar wind nebula) has significantly driven the thinking about linear momentum-angular momentum correlations expected in different birth kick models. Indeed, as the index case, the Crab pulsar has suggested that many pulsars may have spins and kicks aligned at birth. A simplified interpretation (Spruit & Phinney 1998; Romani 2005) suggests that during core collapse, the momentum imparted by the kick is rotationally averaged, resulting in alignment between velocity and spin vectors. Hence the alignment angle is an important observational parameter that places constraints on the characteristic timescale of the kick. Ng & Romani (2004) derived the Crab pulsar's spin axis at PA $124\overset{\circ}{.}0 \pm 0\overset{\circ}{.}1$ (equivalent to $304\overset{\circ}{.}0 \pm 0\overset{\circ}{.}1$) by pulsar wind torus fitting. Comparing with the best-fit proper motion leads to a misalignment of $26^\circ \pm 3^\circ$, which is substantially larger than the previously suggested value. This is also greater than that of several other pulsars, including the Vela pulsar (Ng & Romani 2004). Note that the measured angle is the projection on the sky plane of the true 3-D alignment angle. The latter cannot, of course, be deduced unless the pulsar's radial velocity is known. However, using the 3-D orientation of the nebula's symmetry axis (Ng & Romani 2004), simple geometry shows that for a random pulsar radial velocity between -500 km s^{-1} to 500 km s^{-1} there is only 8% chance to obtain a 3-D alignment angle *s*maller than the projected value. In fact, the 3-D misalignment is always greater than 23° for any value of the radial velocity. The large alignment angle relaxes the constrains on pulsar kick during core collapse. Since the initial spin period for the Crab pulsar is about 19 ms, our result suggests that a short kick timescale is allowed, possibly much less than 1s. Of course, a more detailed treatment of the spin induced by the off-center kick can complicate the interpretation (Spruit & Phinney 1998; see Chapter 5).

Our analysis is clearly not the last word on the important question of the Crab pulsar's proper motion. Improved astrometry, with more accurate distortion correction, and an improved time base employing newly scheduled ACS images should

allow the use of all the *HST* images and further reduce the proper motion errors. Perhaps a final measurement with the WFPC2, with the pointing parameters of group 1 would also be useful, ensuring the minimal sensitivity to systematic errors. Pursuit of such measurement is quite important since our result, at a minimum, calls in to question the widely accepted alignment of the Crab pulsar's spin and velocity.

Chapter 3

Fitting Pulsar Wind Tori

This chapter is based on "Fitting Pulsar Wind Tori", C.-Y., Ng & Roger W. Romani 2004, ApJ, 601, 479.

3.1 Introduction

The Crab nebula has long been known to have a subluminous zone and termination shock surrounding its central pulsar. One of the striking successes of the *Chandra X-ray Observatory* (*CXO*) mission has been to show that this shock is likely an equatorial band and that similar structures are seen around a number of young pulsars (e.g. Weisskopf et al. 2000; Pavlov et al. 2001; Helfand, Gotthelf, & Halpern 2001; Gotthelf 2001). Romani & Ng (2003) argued that the apparent symmetry of such PWNe, if interpreted as equatorial tori, allowed a robust fit for the 3-D orientation of the pulsar spin axis $\vec{\Omega}$ and showed that measurement of this axis can be effected even for quite faint pulsar wind nebulae (PWNe). They also argued that, taking PSR J0538+2817 as an example, comparison of the spin axis with the proper motion vector $\vec{v}$ can be a sensitive probe of pulsar physics (see Spruit & Phinney 1998; Lai et al. 2001). In particular, when the alignment is due to rotational averaging of the transverse momentum, tight alignments imply momentum kicks lasting many times the pulsar initial spin period. Such time constraints on the kick timescale can exclude otherwise plausible models. We wish here to systematize this

comparison by outlining how robust fits for model parameters can be obtained even for relatively low-count *CXO* PWNe images.

The characteristic scale of the wind termination shock around a pulsar of spin-down power $\dot{E}$ is

$$r_T \approx (\dot{E}/4\pi c P_{ext})^{1/2}.$$

This structure should be azimuthally symmetric about the pulsar spin axis when $P_{ext} \geq P_{ram} = 6 \times 10^{-10} n v_7^2 \mathrm{g/cm/s^2}$, i.e. when the pulsar is subsonic at speed $100 v_7$ km s^{-1}. Pulsars will seldom be sufficiently slow to show toroidal shocks in the general ISM (where they will have PWN bow shocks), but young pulsars often satisfy the azimuthally symmetric torus condition in high pressure SNR interiors. van der Swaluw et al. (2003) have provided analytic descriptions of conditions in SNR interiors, modeling the pulsar parameters required for a subsonic PWN as the SNR evolves.

3.2 Fitting Model and Technique

The discovery papers showing obvious toroidal PWN structure have, of course, often provided estimates of the torus scale, position angle and inclination. However, most of these estimates were simple eyeball matches or, at best 2-D fits of ellipses in the image plane. The ubiquity of clearly equatorial structures with toroidal symmetry and the robust physical interpretation in terms of a static termination shock in an equatorial wind argue that direct fits of the implied 3-D structure are most appropriate. Further, quantitative comparison with other pulsar observables requires error estimates for the geometric parameters, which are often not provided. Finally, we seek to constrain the orientations of central tori in PWNe, even when they are not immediately obvious. All of these considerations require a robust fitting procedure with (statistical) error estimates.

We adopt a default model of a simple equatorial torus with a Gaussian emissivity profile in cross-section. Clearly, this is not a sufficiently detailed model to describe the complete PWN structure in the highest resolution images. In fact, for

Crab, Vela and a few fainter PWNe we find that multiple tori component significantly improve the model fits. Also, we do not fit the detailed radial variation of the torus emissivity and wind speed. Such extensions of the model could be useful for comparison with numerical models of relativistic shock flow (e.g. Komissarov & Lyubarsky 2003; Shibata et al. 2003). However, these models are far from complete, and for the fainter PWNe the existing count statistics do not warrant such model extensions. Accordingly we adopt the generic torus fit and apply this to six pulsars, with increasingly poor image statistics. Since for the bright PWNe fine structure beyond a simple torus is visible, we must assume that these models are incomplete descriptions of the fainter objects as well. However, the simple torus gives an adequate description of the data and, assuming that this model captures the gross nebular structure, we obtain quantitative estimates of the orientation and wind flow parameters. The estimates are quite robust to perturbations in the input fit assumptions. Note also that simpler structures are included as subsets of our fit parameter space, e.g. a simple uniform halo, which is reproduced by a face-on torus with small radius and large blur. Such models are strongly excluded statistically, even for the faintest sources.

As shown in Figure 3.1, we characterize the termination shock (torus) by a polar axis at a position angle Ψ ($0^\circ - 180^\circ$, measured N through E), with inclination angle ζ ($0^\circ - 180^\circ$) from the observer line of sight. The torus is simply described by a radius r and a finite thickness or 'blur' of Gaussian cross section, dispersion δ, about the central ring. We assume that the surface brightness (averaged over its cross section) is uniform in azimuth. However, the post-shock flow is still expected to be mildly relativistic and so an azimuthally symmetric ring will vary in apparent intensity, due to Doppler boosting. Synchrotron emission of intensity I_0 and photon spectral index Γ in the rest frame will have an apparent intensity

$$I \propto (1 - \mathbf{n} \cdot \beta)^{-(1+\Gamma)} I_0$$

(Pelling et al. 1987) where $\beta = \mathbf{v}/c$ is the bulk velocity of the post shock flow and $\mathbf{n}$ is the unit vector to the observer line of sight.

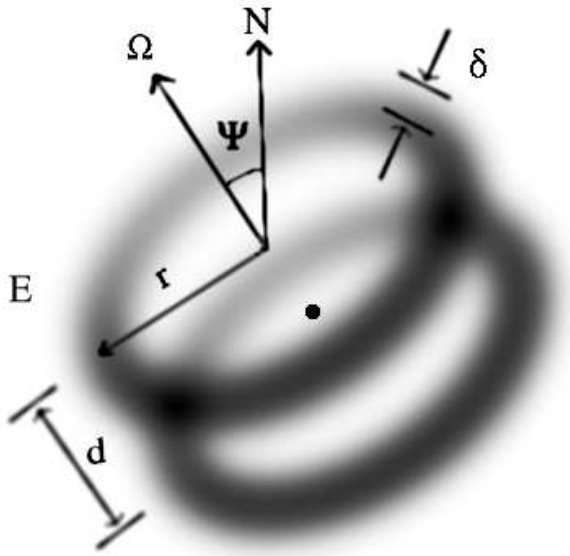

Figure 3.1 Torus geometry. The figure shows the plane-of-the-sky projection of a double torus with fit parameters and angles labeled, and ζ (not shown) is the angle between the sky-plane normal (the Earth line of sight $\hat{z}$) and Ω.

In practice we set up a coordinate grid with x, y oriented with the CCD frame and z along the observer line-of-sight. This is rotated to a grid aligned with the torus

$$\begin{aligned} x' &= -x\cos\Psi - y\sin\Psi \\ y' &= (x\sin\Psi - y\cos\Psi)\cos\zeta + z\sin\zeta \\ z' &= -(x\sin\Psi - y\cos\Psi)\sin\zeta + z\cos\zeta \end{aligned}$$

with x' along the line of nodes, and z' along the torus axis. In this frame the emissivity toward the Earth is

$$I(x',y',z') = \frac{N}{(2\pi\delta)^2 r}\left(1 - \frac{y'\sin\zeta}{\sqrt{x'^2+y'^2}}\beta\right)^{-(1+\Gamma)} \exp\left[-\frac{z'^2 + (\sqrt{x'^2+y'^2}-r)^2}{2\delta^2}\right]$$

where N is normalized to the total number of counts in the torus component. We actually assume a fixed $\Gamma = 1.5$, typical of PWNe and leave β as a model parameter.

These parameters define the basic 3-D torus of PWN emission. To form the 2-D torus image for data fitting, we integrate the emissivity though the line of sight to get the counts in each pixel, i.e.

$$C(x,y) = \sum_z I(x',y',z')$$

The model image also generally includes a uniform background and a point source for the pulsar, whose intensity distribution is the PSF appropriate to the detector position and source spectrum. For Crab and Vela, the point sources have strong pile-up and we can optionally blank a small region around the point source. There are a few special cases of this basic model. In several PWNe (most notably Vela), the termination shock has a double torus, presumably spaced above and below the spin equator. We model this with identical tori, symmetrically offset along the torus axis about the pulsar by distance d, following Helfand, Gotthelf, & Halpern (2001). In the case of the Crab, the structure includes two, apparently inner and outer, tori. Finally in several cases relatively bright polar jets complicate the analysis. We can add model jet emission along the torus axis, blank the jet regions or include jet region photons as a fixed background. We do not at present fit these components separately but their inclusion makes for more appealing model images. The torus parameters are robust to the inclusion or exclusion of the 'jet' region photons.

Thus the basic torus model includes parameters Ψ, ζ, r, δ, β and a background. Additional parameters can include the point source counts or double torus separation. To keep the model parsimonious, we apply the constraint that the total model counts $\Sigma_{xy} C_{xy}$ match the image counts (except for the Crab, where bright complex background structure is not adequately modeled by a constant background). Our fitting procedure uses maximum likelihood, with a merit function formed from the summed log probabilities of the observed counts d_{xy} in each image pixel. We use Poisson statistics

$$P(d_{xy}) = \frac{C_{xy}^{d_{xy}}\ e^{-C_{xy}}}{(d_{xy}!)}\ ,$$

passing to Gaussian statistics for an expected pixel count $C_{xy} \geq 20$ in the CCD

image. In this way the distribution of fluctuations in the fitted model parameters passes smoothly to χ^2 statistics in the limit of high count images. The merit function is minimized, using the simulated annealing package in Numerical Recipes (Press et al. 1992). The initial parameter estimates are chosen by eye and the simplex generally relaxes quickly to the stable final solution, with a robust insensitivity to the initial conditions. The one exception is the blur thickness δ, which has a tendency to grow to absorb the unmodeled larger scale PWN enhancement present in many of the brighter nebulae. As this parameter is not particularly useful in the physical description of the shock, we fixed it at the initial (visual estimate) value in a number of cases. The other fit parameters are quite insensitive to δ over a broad range $\delta < r$.

Equally important are the parameter error estimates. We obtain these via fits to Monte Carlo Poisson realizations of the best fit-model. After 500 random simulations and fits we examine the distribution of the fit parameters. These distributions are well-behaved, with near-Normal distributions about the original fit parameters. We quote here 1σ confidence intervals corresponding to 68% CL. These are projected (i.e. true multi-parameter) estimates of the statistical errors in the fit parameters. At very high confidence levels ($> 99\%$) the parameters become poorly constrained, especially for the fainter PWNe. Nevertheless we find that the estimated statistical errors are quite reliable well beyond 2σ. Systematic errors, due to jets, complex backgrounds, or other unmodeled structures are of course not included, but these statistical estimates appear dominant for all but the brightest PWNe and thus provide useful estimates of the parameters of the *torus component* which captures the gross structure of the central PWN.

The simulations also reveal correlations between the fitting parameters. Ψ is, as expected, well decoupled from the other parameters. ζ and β are substantially co-variant with correlation coefficients as large as 0.7 since both affect the brightness ratio between the front and back sides of the tori. Fluctuations toward large inclination thus have reduced β. Similarly for the PWNe with large inclinations, ζ and r are covariant (coefficient 0.3 to 0.7) since the projected angle of the torus' bright edge $r\cos\zeta$ is well constrained by the images. Our reported 1σ errors include

Table 3.1. Best-fit parameters and errors.

object	$\Psi(^\circ)$	$\zeta(^\circ)$	$r(''$)	$\delta(''$)	β	PS/torus	sep ($''$)
Crab (inner)	$124.0^{+0.1}_{-0.1}$	$61.3^{+0.1}_{-0.1}$	$15.60^{+0.03}_{-0.03}$	1.5*	$0.490^{+0.005}_{-0.006}$	$\cdots/1.0\times10^5$	$\cdots$
Crab (outer)	$126.31^{+0.03}_{-0.03}$	$63.03^{+0.02}_{-0.03}$	$41.33^{+0.02}_{-0.03}$	5.9*	$0.550^{+0.001}_{-0.001}$	$\cdots/1.1\times10^7$	$\cdots$
Vela	$130.63^{+0.05}_{-0.07}$	$63.60^{+0.07}_{-0.05}$	$21.25^{+0.03}_{-0.02}$	3.0*	$0.44^{+0.004}_{-0.003}$	$\cdots/1.3\times10^6$	$11.61^{+0.03}_{-0.03}$
J1930+1852	91^{+4}_{-5}	147^{+3}_{-3}	$4.6^{+0.1}_{-0.1}$	$1.1^{+0.1}_{-0.1}$	$0.62^{+0.04}_{-0.03}$	1701/602	$\cdots$
J2229+6114	103^{+2}_{-2}	46^{+2}_{-2}	$9.3^{+0.2}_{-0.2}$	2.5*	$0.49^{+0.02}_{-0.02}$	2221/1113	$\cdots$
B1706−44	175^{+3}_{-4}	55^{+3}_{-3}	$3.5^{+0.2}_{-0.1}$	0.74*	$0.65^{+0.03}_{-0.04}$	384/168	$\cdots$
J0538+2817	155^{+8}_{-8}	99^{+8}_{-8}	$6.3^{+1.0}_{-0.7}$	$1.7^{+0.3}_{-0.7}$	$0.54^{+0.09}_{-0.08}$	2442*/52	$\cdots$

* – held fixed in the global fit.

these projected correlations.

Fit parameters and errors are reported for six PWNe with a range of brightness in Table 3.1. We start with the 'obvious' tori of Crab and Vela, continue with the 'apparent' tori of PSR J2229+6114 and PSR J1930+1852 and extend to two faint 'plausible' tori from pulsars for which existing estimates of the proper motion make spin axis measurements of particular interest (Fig 3.2). There are perhaps 10 additional PWNe where such analysis could be fruitful, and we expect several more useful torus measurements will be made as the *CXO* mission matures. In the present analysis, all images are from archival ACIS-S data sets, energy cut to 0.5−5 keV. For the Crab we use ObsID 1998 (25 ks), for Vela we combine ObsIDs 1987 and 2813−2820 (180 ks). For the other objects we use the following observations: G54.1+0.3 (ObsID 1985, 40ks), PSR J2229+6114 (ObsID 2787, 100 ks), PSR B1706−44 (ObsID 757, 15 ks), PSR J0538+2817 (ObsID 2796, 20ks). We mention here special features of individual fits.

The two Crab tori are fitted sequentially, with the outer torus fitted first and then used as a fixed background for the inner torus fits. The model shown combines both components. The fitted tori are close to co-planar and have very small statistical parameter errors due to the high image counts. The Vela tori are spaced

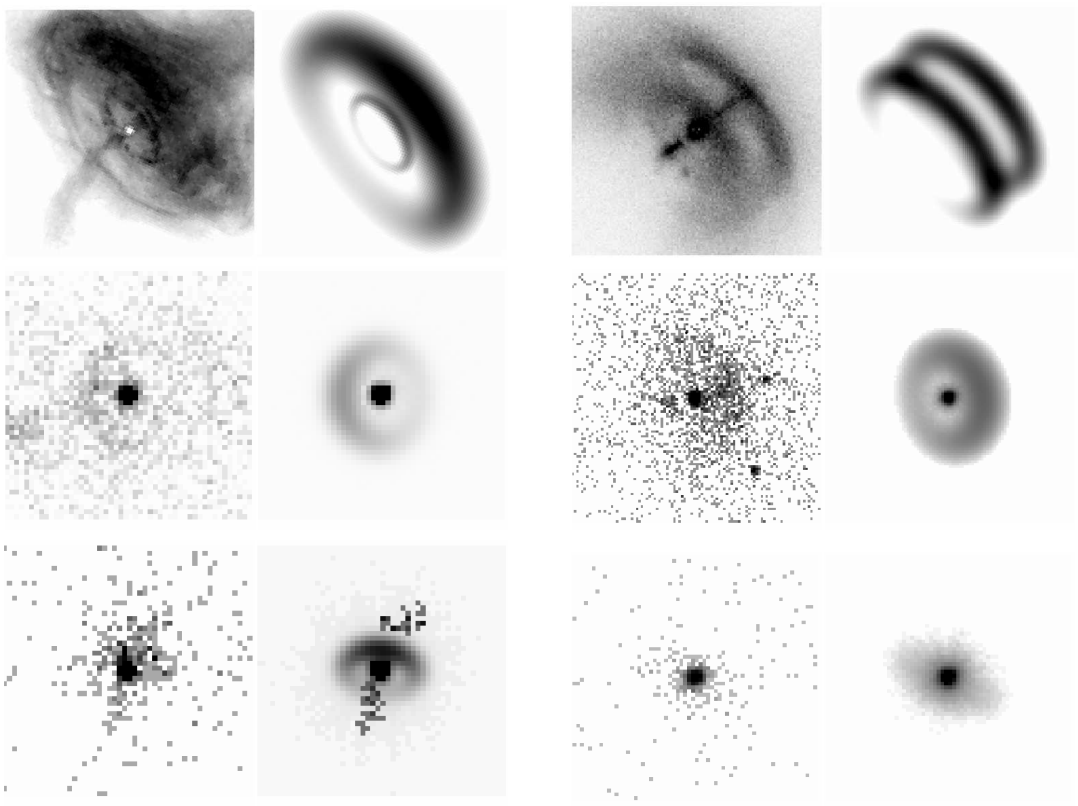

Figure 3.2 Pulsar wind tori. *CXO* ACIS images (*left*) and best-fit models (*right*) for the Crab, Vela, G54.1+0.3, PSR J2229+6114, PSR B1706−44, and PSR J0538+2817 (*left to right, top to bottom*).

symmetrically about the pulsar, centered along the symmetry axis; we quote the value d in arcseconds projected on the sky. For the Crab and for Vela, the high S/N images show complicated fine detail in the tori and unmodeled fainter structures in the surrounding PWN. We have tested the fit sensitivity to these structures by, eg. blanking the jet regions, adjusting the blur thickness and shifting starting fit parameters. We find surprisingly small sensitivity to these changes in the torus fits: the fit values are quite robust, although clearly the very small statistical errors will be dwarfed even by the modest systematic biases.

For SNR G54.1+0.3 and PSR B1706−44, the global minima of the merit functions pull the tori to small radii to absorb excess counts in the PSF wings of the central pulsar. By excluding torus count contributions to the merit function for

pixels at $< 2''$, we obtain the minima listed in the table, which match the visual structure of the nebulae. PSR B1706−44 also has bright regions above and below the fit torus, which can be interpreted as polar jets and that produce a modest fraction of counts attributable to the putative torus. To minimize the sensitivity of the torus fit to these 'jet' photons, we add these counts as a fixed background in the model, as can be seen in the corresponding model image.

The PWN of PSR J0538+2817 is quite faint, providing only $\sim 2\%$ of the point source counts. Accordingly, the geometry of the torus is sensitive to the amplitude of the PSF, and so the point source normalization cannot be fitted simultaneously. Instead the PSF amplitude is first fitted in the central $1''$. This (pile-up corrected) PSF is held fixed during the torus fitting. Consistency is checked by re-fitting with the point source in the presence of the torus background, confirming that the amplitude is unaffected. Romani & Ng (2003) have previously described this PWN, arguing that the spatial and spectral distinction from the PSF wings make the nebula highly significant, despite its low count rate. The fit errors in Table 1 are slightly larger than those in Romani & Ng (2003), because of the additional fit parameters and the multi-dimensional errors. In particular, slightly smaller errors ($\sim 6^\circ$ vs. $\sim 8^\circ$) can be obtained by direct fits to Ψ alone. However, an equatorial extension of the PWN is strongly required in the fit, the Ψ estimate remains robust to perturbations of the starting conditions and a simple uniform halo (small ζ) is strongly excluded – the figure of merit degrades to the 3.6σ level, referenced to our multi-parameter error flags, for models with $\zeta \approx 0$.

3.3 Application of Fit Parameters and Conclusions

In our fitting, we find that (for ζ not too small) the position angle Ψ is the most robust parameter. We believe that even if the simple torus model is inadequate to fully describe all nebulae, this measurement of the position angle of transverse PWN extension is very robust. Thus comparison of the projected fit axis with the proper

motion axis remains an important application. For Crab, the Caraveo & Mignani (1999) *HST* measurement of the Crab proper motion lies at $\Psi_{PM} = 292^\circ \pm 10^\circ$. This is 12° or 1.2σ off of our inner ring axis. Similarly for Vela, we compare with the new radio interferometric proper motion of Dodson et al. (2003a) at $\Psi_{PM} = 302^\circ \pm 4^\circ$, which has both higher astrometric accuracy and a corrected treatment of Galactic rotation effects from earlier optical estimates. This vector lies $8\overset{\circ}{.}6$ from our fitted torus axis, a $\sim 2.1\sigma$ discrepancy. Several other comparisons are semi-quantitative at present; we discuss these below.

Neither PSR J1930+1852 in G54.1+0.3 nor PSR J2229+6114 in G106.3+27 has a directly measured proper motion. Further, these SNR are complex with no clear shell structure, so a velocity vector has not been estimated from an offset birth site. In contrast, Dodson & Golap (2002) and Bock & Gvaramadze (2002) have re-examined the controversial association between PSR B1706−44 and G343.1−2.3, and argued that this partly shell-like SNR is larger than previously believed, placing the pulsar well in the interior and making the association more plausible. The former authors find a southern extension suggesting a more complete circular shell; the vector from the center of this structure is at $\Psi_{PM} \sim 150^\circ$. The latter authors suggest a proper motion parallel to the expansion of the nearby bright shell rim, $\Psi_{PM} \sim 170^\circ$. These position angles are $\sim 10^\circ - 20^\circ$ from our fit axis, but since the SNR evidently suffered asymmetric expansion, both of these geometrical estimates are uncertain. Thus while the axes are in general agreement, a direct measurement of the proper motion is essential for any serious comparison. PSR J0538+2817, in contrast, resides in S147 which has a quite symmetrical structure. Romani & Ng (2003) estimated a proper motion axis from the offset at $-32^\circ \pm 4^\circ$, i.e. $< 1\sigma$ off of the PWN axis measured here. Kramer et al. (2003) have recently managed to extract a timing proper motion for this pulsar which confirms the association with S147, although the PA is poorly determined. Here, both higher statistics X-ray imaging and an astrometric proper motion are needed to effect a precision test.

There are two other young pulsars in shell SNR with recent proper motion measurements, PSR B1951+32 in CTB 80 and PSR B0656+14 in the Monogem Ring.

PSR B1951+32 has a proper motion at $\Psi_{PM} = 252° \pm 7°$ away from its SNR birth-site (Migliazzo et al. 2002) and is presently interacting with the dense swept-up shell. Thus the prominent bow shock seen in *HST* imaging is not unexpected; one would not expect a toroidal wind shock. It is plausible that a 'jet' wind could punch through the bow shock and Hester (2000) has proposed that the Hα 'lobes' bracketing the bow shock mark the pulsar polar jets. Under this interpretation we measure the spin axis is at $\approx 265° \pm 5°$, which is 13° ($\sim 1.4\sigma$) away from the proper motion axis.

With a new parallax distance measurement, Brisken et al. (2003) and Thorsett et al. (2003) find that PSR B0656+14 is enclosed within the $\sim$ 66pc-radius Monogem ring. The surprisingly small proper motion at $\Psi_{PM} = 93\overset{\circ}{.}1 \pm 0\overset{\circ}{.}4$ implies a transverse velocity of only 60 km s^{-1}. If the pulsar has a more typical $\sim$ 500 km s^{-1} space velocity, it must be directed along the Earth line-of-sight; indeed, the parallax distance is consistent with the near side of the Monogem ring. At its characteristic age, the pulsar should still be within the remnant interior for radial velocities as large as $\sim$ 600 km s^{-1}. This SNR exploded in the low density local ISM, so we expect the PWN to be toroidal with a characteristic radius of $\sim 3''$. Interestingly, a short *CXO* observation shows a faint, nearly circular halo around the pulsar at this scale (Pavlov, Zavlin, & Sanwal 2002), suggesting a face-on torus. Scheduled *CXO* observations have the sensitivity to map this structure, which we predict will be consistent with a torus tilt of $\sim 15°$.

Table 3.2 collects the projected proper motion and spin-axis position angle ($\vec{v}$, $\vec{\Omega}$) estimates along with estimates of the line-of-sight inclination for these young pulsars. The trend toward alignment (small $|\Delta\Psi_{\Omega \cdot v}|$) is strong, albeit imperfect. Formally, one should impose *a prior* on the maximum total space velocity v before evaluating the likelihood of a position angle range $\{\Delta\Psi\}$. If the 3-D angle between $\vec{v}$ and the projected position angle is θ, then a physical upper limit on the plausible $v = v_\perp \cos\theta / \cos\Psi$ restricts the allowed range of θ. However, in practice all of these pulsars have relatively small $v = v_\perp$, so the disallowed range is negligible and the probability of a position angle range is simply $2(\Delta\Psi_{max} - \Delta\Psi_{min})/\pi$.

If only the 1σ maximum $|\Delta\Psi|$ are considered, then for Crab and Vela alone, there

Table 3.2. Proper motion and spin axis angles.

Pulsar	Ψ	$\Psi_{PM}{}^{\dagger}$	$\lvert\Delta\Psi_{\Omega\cdot v}\rvert$	ζ	ζ_R	ζ_R Ref.
B0531+21	124.0 ± 0.1	292 ± 10	12 ± 10	61.3 ± 0.1	62	1
B0656+14	···	93.1 ± 0.4	···	small	16	2
J0538+2817	155 ± 8	$328\pm \sim 4$	7 ± 9	99 ± 8	97	3
B0833−45	130.6 ± 0.1	302 ± 4	8.6 ± 4	63.6 ± 0.1	56	4
B1706−44	175 ± 4	$160\pm \sim 10$	$15\pm \sim 11$	55 ± 0.2	75	5
B1951+32	$85\pm \sim 5$	252 ± 7	$13\pm \sim 9$	···	···	···

References. — † see text; (1) Romani & Yadigaroglu (1995); (2) Lyne & Manchester (1988); (3) Kramer et al. (2003); (4) Krishnamohan & Downs (1983); (5) S. Johnston, private commmunication.

is a 3% chance of obtaining alignments as close as those seen from isotropically distributed $\vec{v}$, $\vec{\Omega}$. However if the other three angle estimates of Table 3.2 are included, the chance probability falls to 0.04%. On the other hand, the weighted combination of these measurements gives $\langle|\Delta\Psi_{\Omega\cdot v}|\rangle = 10\overset{\circ}{.}0 \pm 2\overset{\circ}{.}7$, significantly different from 0. This finite misalignment probes the characteristic timescale of the neutron star birth kick, adopting the Spruit & Phinney (1998) picture of rotational averaging. As discussed in Romani & Ng (2003), the kick timescale constraints are very sensitive to the initial spin periods of the individual pulsars. We defer a detailed comparison with kick models to a later communication.

A reliable measurement of the spin axis inclination ζ can also be particularly valuable for these young pulsars. Many of these objects are high energy (hard X-ray and γ-ray) emitters and the modeling and interpretation of the pulse profiles is quite sensitive to ζ (Romani & Yadigaroglu 1995). Radio techniques (polarization sweeps and pulse width fitting) are often used to estimate ζ, but these are subject to substantial interpretation uncertainties. For example polarization sweep results are affected by 90° mode jumps in various pulse components, which can often only be resolved with single pulse studies. Perhaps this complexity is not surprising, since the radio emission, at relatively low altitude, is sensitive to higher order multipoles

and the details of the magnetic polar cap structure. In the wind zone all such details are likely lost. If high energy emission is generated in outer magnetosphere ($\sim 0.1 - 0.3 r_{LC}$) gaps, then since r_{LC}/r_{NS} is large, high order multipoles should die away and the pulse profiles should be sensitive only to magnetic inclination and ζ.

We list some radio inclination estimates in Table 3.2 – however we caution that substantially different values are available in the literature for many of these pulsars. For Crab and PSR J0538+2817 the agreement with our fit ζ appears good. For Vela and PSR B1706−44 the discrepancies are large. Interestingly, Helfand, Gotthelf, & Halpern (2001) match the axis ratio of the projected PWN torus by eye and find $\zeta = 55°$ in good agreement with the radio estimate; however this value is very strongly excluded in our fits. Our relative ζs for Vela and PSR B1706−44 do however make sense in the outer magnetosphere picture (Romani & Yadigaroglu 1995), with PSR B1706−44 at smaller ζ producing a narrower double γ-ray pulse and a larger phase delay from the radio. We can further make some predictions for objects not yet observed at γ-ray energies. If our PWN ζ estimates hold up, we would expect γ-ray emission from PSR J2229+6114 to show a merged double pulse, somewhat narrower than that of PSR B1706−44 (as appears to be the case in the hard X-ray), while PSR J0538+2817 should show a wide, Vela-like double pulse. PSR J1930+1852 in G54.1+0.3 may be very faint in the γ-ray since its small $180° - \zeta = 33°$ suggests that any outer-magnetosphere γ-ray beams miss the Earth line-of-sight. Finally PSR B0656+14, which is many times fainter in > 100MeV γ-rays than expected from its spin-down luminosity, is widely believed to be viewed nearly pole-on. In this orientation the strong outer-magnetosphere γ-ray beams would not be visible, although we should see γ emission from the pair production fronts in the radio zone above the polar cap. New *CXO* imaging may allow a quantitative fit to the PWN, supporting the apparent small ζ.

Also physically interesting are the estimates for the post-shock velocities β. For the Crab nebula, our fit value compares well with the $\beta \sim 0.5$ found for the motions of wisps near the torus (Hester et al. 2002), although clearly our very small statistical fit errors must under-predict the true uncertainty. Moreover, it is puzzling that we get slightly larger β for the outer ring. One certainly expects the flow speeds to

drop rapidly in the outer nebula and *CXO*/*HST* data do show pattern velocities as small as $\beta \sim 0.03$ in the outer parts of the X-ray nebula. For Vela, no estimates of β from torus motions have yet been published, but Pavlov et al. (2003) find $\beta \sim 0.3 - 0.6$ for features in the outer jet, which bracket the torus β found here. The interpretation of the outer jet speed is apparently complicated by a varying orientation with respect to the line of sight. Likely the inner jet/counter-jet provide a cleaner comparison with the torus β; several authors have noted the larger counter-jet brightness suggests that it is approaching the observer. Using the time-averaged image in Figure 3.2, measuring a $5''$ length equidistant from the pulsar on each jet and subtracting the interpolated background from either side, we find a counter-jet/jet count ratio $f_B = 2.3$. For a continuous, time-average jet of photon index Γ the Doppler boosting ratio is

$$f_B = [(1 + \beta \cos\zeta)/(1 - \beta \cos\zeta)]^{\Gamma+1}$$

(the power $\Gamma+2$ applies for isolated bright blobs). Pavlov et al. (2003) report a inner jet spectral index $\Gamma \approx 1.1$, which with our fit ζ gives $\beta_J = 0.45$, in remarkably good agreement with our torus β. It is worth noting, however, that even these inner jets show significant variation, so a time-resolved study of pattern speeds and brightness is likely needed for a precise jet β.

No clear pattern yet emerges from the β estimates presented here, although there is a weak anticorrelation between the light cylinder magnetic field and β (correlation coefficient ≈ -0.3). If significant, this may suggest an anticorrelation between pair multiplicity, expected to be large in the narrow gaps of high $\dot{E}$, short period pulsars, and the wind speed. Ultimately, comparison of β in different PWN components at different latitudes, and between PWNe, promises to become an important new probe of pulsar electrodynamics.

For Vela, and a few fainter objects, the presence of a double ring already suggests some increase in pair multiplicity away from latitude $0°$. If we de-project the ring separation as seen from the pulsar, we get a brightness peak (mid-plane of the torus)

at co-latitude

$$\theta_{\rm Tor} = \tan^{-1}(2r\sin\zeta/d) \approx 74^\circ.$$

This is about 10° larger than our best fit ζ. For Vela, the polarization sweep rate maximum suggests a magnetic axis impact angle $\beta = \zeta - \alpha = -4^\circ$. Notice that this is on the same side of the line-of-sight ($\alpha > \zeta$) as our fit torus. Thus we might plausibly associate the two tori with a near-radial outflow of high pair multiplicity plasma from the magnetosphere open zones. Perhaps further observation and modeling could distinguish between pairs produced in a vacuum gap near the star surface (polar cap) with plasma produced in an outer magnetosphere gap above the null-charge surface. For example, the outer magnetosphere gaps should populate field lines at angles $> \alpha$, consistent with the observed $\theta_{\rm Tor} > \alpha$. If α is close to $\pi/2$ (e.g. Crab, PSR J0538+2817) the pair plasma from the two poles should merge, leading to a single thicker torus.

In conclusion, the ubiquitous azimuthally symmetric torus (+jet) structures seen about young pulsars provide an important new probe of the viewing geometry. We have described a procedure for fitting simple geometric models to X-ray images that match the gross structure of the central regions of many PWNe and provide robust estimates for model parameters. These models clearly do not capture all of the rich, and dynamic, structural details seen in the brighter nebulae, such as Crab and Vela. However the fitting procedure does reduce biases of by-eye 'fits' and does allow extraction of geometrical parameters from quite faint objects. Accordingly, such fits should allow us to measure spin axis orientations for a larger set of pulsars and use these angles to probe models of the neutron star kick and of pulsar magnetospheric physics.

Chapter 4

Application of Pulsar Wind Torus Fitting

In the previous chapter we discussed the pulsar wind torus fitting method and its application to a few X-ray observations. In order to have a more comprehensive study, we attempt to quantify the systematic errors in this chapter and apply the fitting to more *CXO* PWN observations.

For bright objects such as the Crab and Vela pulsars, the signal-to-noise ratio (S/N) is high and statistical errors in the fit are insignificant. Hence the uncertainties are dominated by systematic errors. On the other hand, the fit for faint objects is limited by the Poisson statistics as well as the systematic errors. In our fitting scheme, the latter are usually due to some unmodeled features in the data, such as polar jets, diffuse background, or an imperfect PSF model. Therefore by removing the corresponding components in the fit, their contributions to the uncertainties may be estimated.

In this study we went through the *CXO* data archive and identified a list of observations with apparent toroidal termination shocks in PWNe (Table 4.1). There are a few other objects with jets and/or possible tori (e.g. PSR B1509−58), but for these cases closer examinations suggest that the pulsar motions maybe trans- or super-sonic, hence static torus fits are not appropriate. The data are cleaned up with standard reduction procedures using CIAO and the background lightcurves are

Table 4.1. Archival dataset used in this study.

Pulsar	SNR	ObsID	Instrument	Exposure (ks)
Crab	Crab Nebula	1998	ACIS	25
Vela	Vela	1987, 2813−2820	ACIS	180
J1930+1852	G54.1+0.3	1985	ACIS	40
J2229+6114	G106.3+2.7	2787	ACIS	100
B1706−44	G343.1−2.3	4608	ACIS	100
J2021+3651	G75.2+0.1	3901	ACIS	19
J0205+6449	3C 58	3832, 4382, 4383	ACIS	350
J0537−6910	N157B	2783	ACIS	50
B0540−69	SNR 0540−69.3	132, 1735, 1736, 1727, 1738, 1741, 1745	HRC	75
J1124−5916	G292.0+1.8	1953	HRC	50
B1800−21	···	5590	ACIS	30
J1833−1034	G21.5−0.9	1230,1554,159,2873,3700	ACIS	56

examined to filter out periods that suffered from strong background flares. Then we remove the pixel randomization for the ACIS observations and apply an algorithm by Mori et al. (2001), which corrects the positions of the split pixel events, to improve the spatial resolution. Finally we select the appropriate energy range and binning to optimize the S/N of the PWNe, separating out the soft background from the SNR and field stars.

Following the fitting procedures as described in Chapter 3, the best-fit parameters are obtained by maximizing the likelihood function, and Monte Carlo realizations are employed to estimate the statistical errors (see Chapter 3 for the details). To determine the contributions of the unmodeled features to the uncertainties, we blank out different regions in the data (i.e. not consider those bins in the fit) and re-fit the model by varying only one parameter at a time and keeping all the others fixed at their best-fit values. The difference in the best-fit parameter values thus provide estimates of the systematic errors.

In the actual implementation, we begin by blanking out the jet regions in the observations, since they are the most obvious features and are present in many systems. As an example, the image of PSR B0540−69 with jet regions removed is shown in Figure 4.1. This gives the systematic error estimates for the Crab, Vela, PSRs J2229+6113, B1706−44, J2021+3651 and B0540−69. However for PSRs J1930+1852 and J0205+6449, the jets are relatively faint and well-separated from

the PWNe. As a result, removing the jets alone does not change the parameter values significantly. We believe this underestimates the systematic errors and contributions from other unmodeled features should also be considered. Therefore, we obtained another estimate by removing the point source in the data. The results reported are the combination of the two estimates, added in quadrature. Another special case to note is PSR J0537−6910: instead of polar jets, a cometary trail is observed in the data. This is modeled by a rectangular background region with constant brightness in the fit. Comparison with the best-fit parameters without the background provides an estimate for the systematic errors.

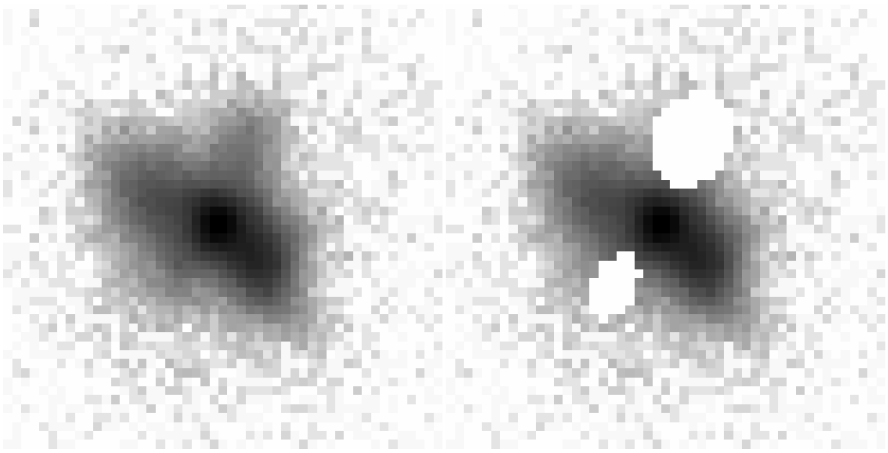

Figure 4.1 *Left: Chandra* ACIS image of PSR B0540−69; *right*: same image with jets removed.

Table 4.2 lists the best-fit results with corresponding statistical and systematic errors. We report the systematic errors for Ψ, ζ, r and the separation only, since they are the most interesting parameters. Systematic errors in other parameters have similar fractional values when compared to the best-fit parameters. Note that for the faint objects including PSRs J1124−5916, B1800−21 and J1833−1034, their detailed structures are not resolved and the statistics does not allow us to determine the systematic errors. Therefore we report only the statistical errors here, which are in any case, dominant. The best-fit models for the new objects in this study are shown in Figure 4.2, the rest may be found in Figure 3.2 and the references listed in Table 4.2.

Table 4.2. Best-fit 'torus' parameters with statistical and systematic errors.

object	$\Psi(^\circ)$	$\zeta(^\circ)$	$r(''')$	$\delta('')$	β	sep $('')$	PS/torus (Cts)	Ref.
Crab (inner)	$124 \pm 0.1 \pm 0.1$	$61.3 \pm 0.1 \pm 1.1$	$15.6 \pm 0.03 \pm 0.1$	1.5*	$0.49^{+0.005}_{-0.006}$	$\cdots$	$\cdots$ /1.0×10^5	1
Crab (outer)	$126.31 \pm 0.03 \pm 0.11$	$63.03^{+0.02}_{-0.03} \pm 1.3$	$41.33^{+0.02}_{-0.03} \pm 0.2$	5.9*	0.55 ± 0.001	$\cdots$	$\cdots$ /1.1×10^7	1
Vela	$130.63^{+0.05}_{-0.07} \pm 0.05$	$63.6^{+0.07}_{-0.05} \pm 0.6$	$21.25^{+0.03}_{-0.02} \pm 0.5$	3.0*	$0.44^{+0.004}_{-0.003}$	$11.61 \pm 0.03 \pm 0.4$	$\cdots$ /1.3×10^6	1
J1930+1852	$91^{+4}_{-5} \pm 1.1$	$147 \pm 3 \pm 3$	$4.6 \pm 0.1 \pm 0.14$	1.1 ± 0.1	$0.62^{+0.04}_{-0.03}$	$\cdots$	1701/602	1
J2229+6114	$103 \pm 2 \pm 1.6$	$46 \pm 2 \pm 6$	$9.3 \pm 0.2 \pm 0.3$	2.5*	0.49 ± 0.02	$\cdots$	2221/1113	1
B1706−44	$163.6 \pm 0.7 \pm 1.6$	$53.3^{+1.6}_{-1.4} \pm 2.9$	$3.3^{+0.08}_{-0.06} \pm 0.1$	1.0*	0.70 ± 0.01	$\cdots$	2897/1221	2
J2021+3651	$45 \pm 1.3 \pm 0.6$	$79 \pm 1 \pm 2$	$8.0 \pm 0.2 \pm 0.4$	1.2*	0.64 ± 0.02	$3.7^{+0.2}_{-0.1} \pm 0.07$	235/751	3
J0205+6449 (inner)	$90.3^\dagger \pm 0.2 \pm 0.4$	$91.6 \pm 0.2 \pm 2.5$	$2.08^{+0.04}_{-0.02} \pm 0.01$	0.74*	$0.66^{+0.01}_{-0.01}$	$\cdots$	5080/39730	4
J0205+6449 (outer)	$90.3^\dagger \pm 0.2 \pm 0.4$	$90.56^{+0.07}_{-0.05} \pm 0.01$	$16.3^{+0.3}_{-0.1} \pm 0.1$	2.0*	$0.88^{+0.004}_{-0.001}$	$\cdots$	5080/29503	4
J0537−6910	$131 \pm 2 \pm 0.9$	$92.8^{+0.7}_{-0.8} \pm 0.5$	$4.0^{+0.5}_{-0.2} \pm 0.3$	0.47 ± 0.04	0.86 ± 0.02	$\cdots$	102/179	4
B0540−69	$144.1 \pm 0.2 \pm 0.8$	$92.9 \pm 0.1 \pm 0.6$	$2.35 \pm 0.02 \pm 0.06$	0.66*	0.64 ± 0.01	$\cdots$	13442/50215	4
J1124−5916	16 ± 3	105 ± 7	0.9 ± 0.1	$0.5^{+0.02}_{-0.05}$	$0.15^{+0.06}_{-0.04}$	$\cdots$	390/552	4
B1800−21	44 ± 4	90 ± 2	$3.1^{+0.4}_{-0.5}$	0.74*	$0.69^{+0.05}_{-0.12}$	$\cdots$	18/88	4
J1833−1034	45 ± 1	$85.4^{+0.2}_{-0.3}$	5.7 ± 0.2	~ 1.2	0.86 ± 0.01	$\cdots$	304/6541	4

* – held fixed in the fit.

† – fitted simultaneously.

References. — Best-fit parameters and statistical errors are from: (1) Ng & Romani (2004), (2) Romani et al. (2005), (3) Hessels et al. (2004), (4) – this work. All systematic errors are new in this work.

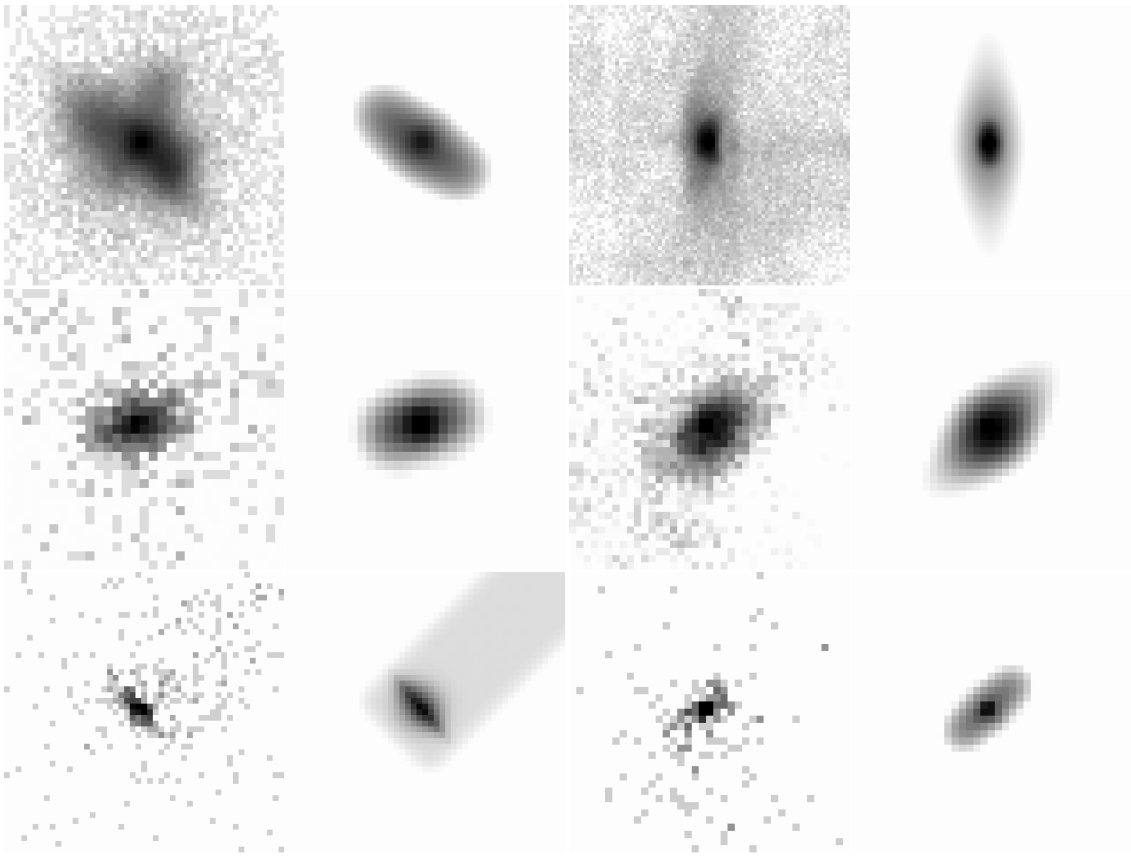

Figure 4.2 New fitting results in this study. *Chandra* data (*left*) compared with the best-fit models (*right*) for PSRs J0205+6449, B0540−69, J1124−5916, J1833−1034, J0537−6910 and B1800−21(*left to right, top to bottom*).

As shown in the table, uncertainties in the parameters for the Crab and Vela pulsars are dominated by the systematic errors and the statistical errors are negligible. For the other objects, the two errors are comparable in Ψ and r, but the systematic errors for ζ are in general much larger. This suggests the fit is more robust in obtaining Ψ and r, as they are mostly determined by the shape of the torus. On the other hand, ζ depends sensitively on the relative brightness of both sides of the torus, hence removing the jet structure could change the results significantly.

There are a few objects in our list which also have independent estimates for Ψ. Johnston et al. (2005) observed the radio polarization for the Vela pulsar and

obtain a P.A. of $126\overset{\circ}{.}8 \pm 1°$. Kothes, Reich, & Uyaniker (2006) measure the radio polarization of the PWN in PSR J2229+6114 and suggest a symmetry axis at P.A.$\sim$ 93°. For PSR B1706−44, the result is controversial. While Wang et al. (2006a) report a P.A. of $162\overset{\circ}{.}0 \pm 10\overset{\circ}{.}0$, Johnston et al. (2005) deduce from the new observation that the polarization angle is difficult to locate. For the Crab pulsar, the radio polarization is very complex and the precursor pulse may help to solve the problem. More observations are needed for a better comparison between the values of Ψ measured by both methods. With the clear geometry provided by the torus fitting technique, it may help to calibrate the radio polarization observations and improve measurements.

In conclusion, we have applied the torus fitting to more PWNe observations in the *Chandra* data archive and characterize the uncertainties in the fits. This study provides a better understanding of the systematic errors as well as the nature of the fit. Altogether this gives quantitative estimates of the measurement uncertainties and helps to develop a more sophisticated model in the future.

Chapter 5

The Spin-Kick Correlation of Young Pulsars

This chapter is based on "The Spin-Kick Correlation of Young Pulsars", C.-Y. Ng & Roger W. Romani 2007, ApJ, submitted.

5.1 Introduction

The high velocity of pulsars, at least an order of magnitude larger than their parent population (Hobbs et al. 2005), has been a long standing puzzle. Of the many models proposed, all except the classic Blaauw (1961) binary break-up mechanism rely directly or indirectly on the large release of gravitational binding energy associated with the core collapse event. Since the fastest observed pulsars have $v > 10^3$ km s^{-1} (Cordes, Romani, & Lundgren 1993; Chatterjee et al. 2005), i.e. bulk velocities $> 3 \times 10^{-4}$ c, binary break-up is clearly inadequate and a viable mechanism must tap an appreciable fraction of the collapse momentum. However, a wide range of physical processes can still be invoked (e.g. Lai et al. 2001; Janka et al. 2005), so gross energetic constraints alone do not solve the pulsar kick problem.

Recent progress has come from studies that probe the *vector* nature of the kick. For example Fryer & Kusenko (2006) argue that neutrino-driven kicks (which may even be crucial for successful explosion) will produce fast supernova remnant (SNR)

velocities along the pulsar velocity vector, while ejecta-driven (recoil) kicks should have fast ejecta opposite to the pulsar motion. The pulsar itself also contains kinematic evidence of the kick geometry, since both the velocity and spin directions are in principle measurable. These linear and angular momenta are fossils of the core collapse which can remain inviolate for as much as 10^6 yr before acceleration in the Galactic potential perturbs the velocity or torques perturb the spin. Thus mechanisms that are spin-dependent can leave a fossil record in the kick distribution (Lai et al. 2001; Romani 2005). Conversely, kicks can leave a record in the spin distribution (Spruit & Phinney 1998).

The key to making such tests is accurate measurement of pulsar motions and pulsar spins. For the former, the most important progress has been the dramatic improvement in the quality and quantity of VLBI astrometric proper motions (Chatterjee et al. 2005). This work makes it possible to have a vector proper motion (and in a number of cases a parallax, and hence a 2-D space velocity) for most moderately bright, $\geq$ few mJy, pulsars within 2-3 kpc. An even larger sample of approximate proper motions has been obtained from refined analysis of long term timing records (Hobbs et al. 2005). Together these methods provide useful space velocities for several dozen young pulsars within 3 kpc. Association with parent supernova remnants can provide a few additional proper motion estimates for interesting pulsars at larger distances.

More difficult to measure is the spin direction. The classic approach is to adopt the 'rotating vector' (RV) model for pulsar polarization and assign the projected position angle (PA) of the spin axis to the absolute (Faraday 'rotation measure' RM corrected) position angle of the polarization at the phase of maximum PA sweep. This method suffers major systematic uncertainties due to poor matches to the expected RV model sweep as well as an intrinsic $\pi/2$ ambiguity according to whether the emission is in the normal or orthogonal mode; early analyses (Deshpande, Ramachandran, & Radhakrishnan 1999) were not at all conclusive. However, recent improved polarization measurements and RM corrections have provided convincing statistical evidence for a projected 2-D correlation between the directions of polarization PA and the proper motion (Johnston et al. 2005; Wang, Lai, & Han 2006a).

Even better, in several cases excellent *CXO* images have made it possible to measure accurately the pulsar spin position angle and its inclination from the plane of the sky, using the symmetry axis of the surrounding pulsar wind nebula (PWN) (Ng & Romani 2004). Finally, in a few cases, one can also independently estimate the original post-supernova spin of the pulsar. With the 3-D spin orientation and amplitude, comparison with the projected 2-D motion allows even more powerful tests of the nature of the birth kick.

In this paper we explore the possibility of comparing the new vector data on pulsar spins and velocities with the dynamics of core collapse. The structure of the paper is as follows. In section §5.2.1, we describe three simple models of the luminosity and size evolution of a proto-neutron star, which we will follow in estimating the effects of a birth kick. In section §5.2.2, we summarize the effect of momentum deposition on kick and spin (following Spruit & Phinney 1998) and show how the integrated kick controls the birth properties of the pulsar. We also comment on the results of Wang, Lai, & Han (2006b), whose related but somewhat simpler study of kick evolution appeared while we were writing up this paper. In Section §5.3, we discuss the sample of nearby and/or young pulsars that we will use for comparison with the models, emphasizing the important objects for which we have more complete knowledge of the post-kick state of the star. Section §5.4 describes a population simulation that allows us to compare the *distribution* of birth properties with the observed neutron stars for the several models. Section §5.5 summarizes the fit results that constrain the basic parameters in the kick models. We conclude by discussing the status of the spin-kick comparison and the insight that the present data give us into the physics of the pulsar kick.

5.2 Core-Collapse Luminosity-Driven Kicks

In this study, we consider some simple models for a kick associated with the large luminosity of the post-bounce proto-neutron star. Our assumptions are: *i*) the asymmetric momentum (kick) scales roughly as the emergent neutrino luminosity, possibly with a delayed onset; *ii*) the *net* thrust originates from a region fixed with

respect to the star; and *iii*) the thrust may be at a finite angle to the local normal. Of course, this net thrust may simply be the surface average of a complex distribution of local forces. However, we assume that the sum of these has a stable component with respect to the star on the timescale of the initial rotation and cooling. If the thrusts are impulsive and random then, as argued by Spruit & Phinney (1998) and illustrated numerically by Wang et al. (2006b), the final velocity and spin tend to become randomly oriented.

The simplest realization of this picture would be asymmetric neutrino emission mediated by strong $B-$fields. Arras & Lai (1999a,b) suggest that due to weak interaction parity non-conservation, the neutrino emission depends on the magnetic field, both through simple field-dependent opacities and through helicity-sensitive scattering in the presence of a strong field. They suggest that the total asymmetry in the neutrino flux is $\sim 0.1 B_{15} \bar{E}_\nu^{-2} + 0.002 B_{15}/T$ where $B = 10^{15} B_{15}$ G is the magnetic field strength, $\bar{E}_\nu$ is the mean neutrino energy in MeV and T is the temperature in MeV. Clearly, very large fields are needed to produce a significant net kick. However, this model does provide a natural 'anchor point' on the star and, through the field angle at the surface, a plausible mechanism for non-normal kicks.

Other possibilities also exist. For example, the net momentum might be generated by asymmetric neutrino coupling to matter in the envelope (Socrates et al. 2005), or by 'neutrino star-spots' induced by the magnetic field (Thompson & Duncan 1993), or even by hydrodynamic motions associated with accretion onto the neutron star (e.g. Blondin & Mezzacappa 2006). In the last case, fall-back instabilities may apparently build to large amplitude. Scheck et al. (2006) have presented a detailed set of 2-D hydrodynamic simulations suggesting that large recoil velocities of neutron stars occur naturally when $m = 1$ instabilities with strong narrow downflows develop. Here the kick velocity is dominated by the gravitational attraction of the dense downflow. (A neutrino hotspot associated with this flow does in fact generate anisotropic emission, but its kick, a $\sim 10\%$ correction, is opposite that of the gravitational term). In such scenarios, the details of the neutrino emission curve are not important, but this luminosity profile does provide a characteristic duration for energetic processes associated with the core collapse. The physical interpretation

is thus not as clear as for the direct neutrino kick scenario, but the characteristic energetics and time scale modeled in our fits can still probe the underlying physics.

5.2.1 Proto-Neutron Star Luminosity Models

We first start from a simple cooling model, where the neutron star is optically thick to neutrinos and the hot envelope is a dominant contribution to the moment of inertia. If the star's gravitational binding energy is promptly released and lost as neutrino radiation from the surface of the proto-neutron star, then the proto-neutron star is in thermal equilibrium and the evolution of its radius $R_{\rm NS}$ is *'quasi-stationary'* and determined by the conservation of energy:

$$L_\nu(t) \sim \frac{d}{dt}\frac{GM^2}{R_{\rm NS}} \ .$$

We show here results using the neutrino luminosity L_ν from Figure 3 in Burrows, Klein, & Gandhi (1992) but have tried different $L_\nu(t)$ from the literature. The results are quite insensitive to the details of any standard cooling curve. In the simulation, the initial proto-neutron star radius is set to a generic value of 100 km. As shown in Figure 5.1, a final radius of 14.7 km is obtained, which is determined by the total neutrino fluence.

At the opposite extreme, we can assume that both the envelope and core are highly degenerate at bounce (for reviews: Janka et al. 2004; Kotake, Sato, & Takahashi 2006). In this case, $R_{\rm NS}$ is independent of $L_\nu(t)$ and the kick essentially acts at a constant radius throughout the cooling. We call this extreme the *'static'* model. In our simulations we take this as $R_{\rm NS}$=10 km, constant throughout the kick.

Results from more physical numerical simulations suggest real neutron star behavior is between the two limiting cases above. To illustrate this, we examined the results of 2-D hydrodynamic simulations from Rampp & Janka (2002) and Janka et al. (2004). These authors employ a Multi-Dimensional Boltzmann Transport and Hydrodynamics (MDBTH) code to follow the neutrino advection and diffusion. In Figure 5.2, we reproduce the mass shell trajectories from Janka et al. (2003) and

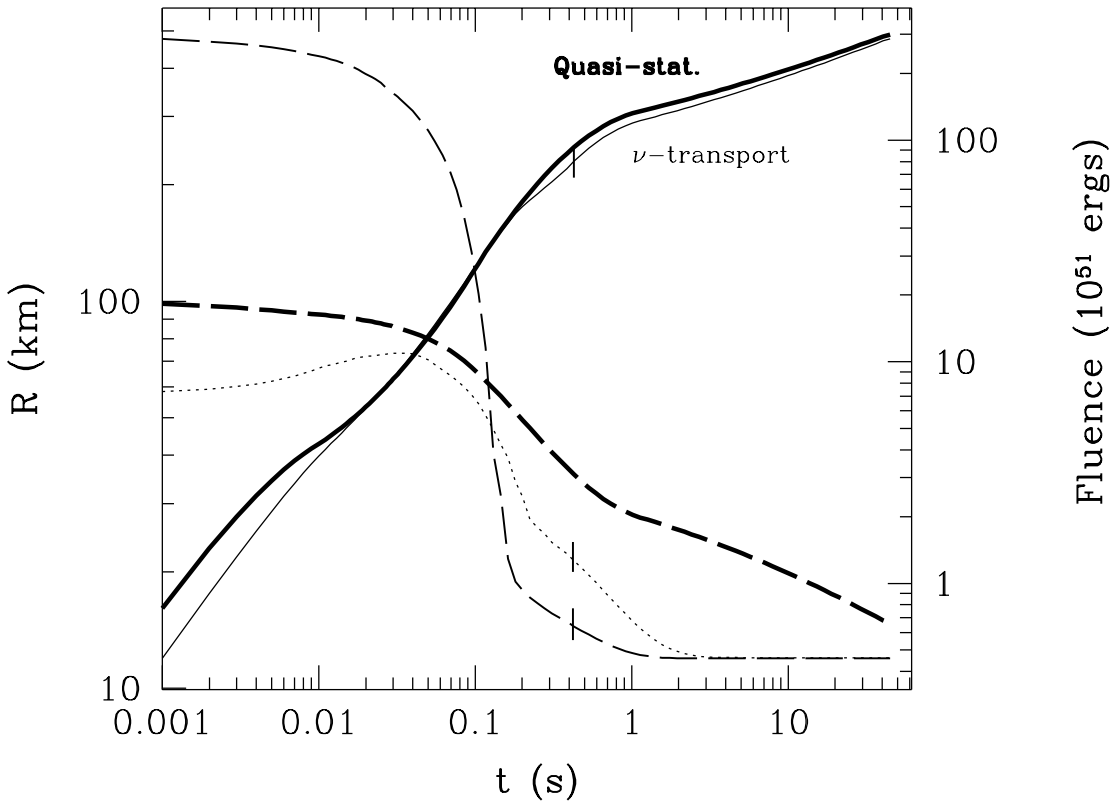

Figure 5.1 Proto-neutron star cooling. Evolution of the stellar radius and the neutrino fluence for the quasi-stationary model are shown in the thick solid and dashed lines respectively. The thin solid and dashed lines show equivalent values for the 'ν-transport' model (Janka et al. 2003), with the effective R of a uniform density sphere with the same instantaneous moment of inertia. The thin dotted line shows the radius of the neutrino-sphere in the 'ν-transport' model. The end points of the numerical simulation are marked; the curves are extrapolated to $t = 50$ s.

show the ν_e photosphere as it evolves during the initial cooling. As one sees, the neutron star initially has a large but optically thin envelope. We will assume the thrust is imparted near the neutrinosphere, but the whole star is forced to co-rotate. The time varying moment of inertia can be followed by integrating across these shells.

The simulations using this evolution are referred to as *'ν-transport'* models. Figure 5.1 compares the basic behavior for the models showing $L_\nu(t)$ and the effective $R_{\rm NS}(t)$. The *'static'* model has, by assumption the same neutrino light curve as the *'quasi-stationary'* picture, albeit at fixed $R_{\rm NS}$. In the case of the *'ν-transport'* model, the simulations available stopped at $t = 0.46$ s (marked). We extrapolate with simple matched exponentials to take the curves to 50 s.

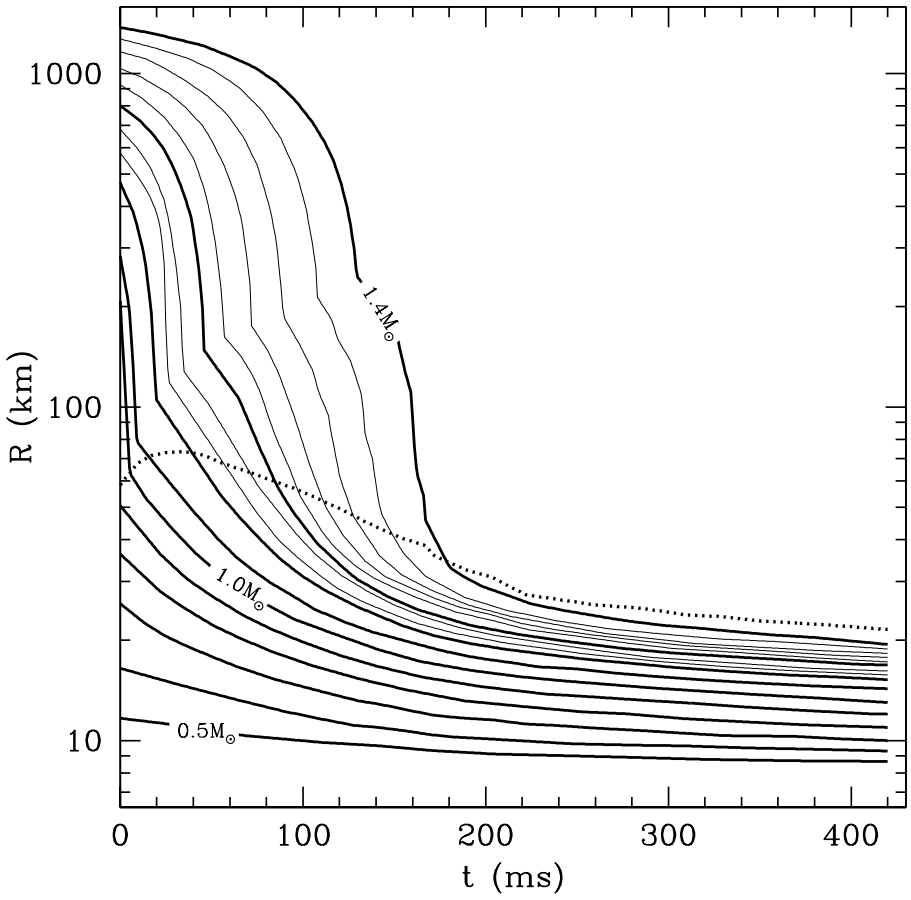

Figure 5.2 Mass shell trajectories of a proto-neutron star in the 'ν-transport' model, reproduced from Janka et al. (2003). Radius of the neutrinosphere is plotted by the dotted line.

5.2.2 Kick Dynamics

We wish to model a (possibly non-normal) net thrust at a fixed point $\vec{r}$ on the proto-neutron star surface which scales with the $L_\nu(t)$ multiplied by a constant asymmetry η. The thrust is given by

$$F_\nu(t) \sim \eta \frac{L_\nu}{c} \ .$$

The angular momentum $\vec{J} = I\vec{\Omega}$ evolves according to

$$\vec{J} = \int \vec{r} \times \vec{F}_\nu \, dt + I_i \vec{\Omega}_i \ ,$$

where I_i and $\vec{\Omega}_i$ are the initial moment of inertia and angular velocity before the kick respectively. Similarly, the linear momentum is determined by

$$\vec{p} = \int \vec{F}_\nu \, dt \ .$$

As we are modeling isolated young neutron stars, three angles determine the kick geometry as illustrated in Figure 5.3: α is the polar angle of the kick position, θ is the off-axis angle of the kick from the surface normal, and ϕ is the azimuth angle of the kick about the normal, with $\phi = 0$ closest to the initial spin axis. Note that we are ignoring any initial space velocity of the progenitor, since with typical values of only a few km s^{-1}, it is negligible compared to the kick velocity of several hundred km s^{-1}. However, some modest fraction of presently isolated young neutron stars are released from the break-up of pre-existing binaries (Dewey & Cordes 1987; Tauris & Takens 1998; Fryer, Burrows, & Benz 1998). In this case, these may have an initial velocity of as much as 100 km s^{-1} (the Blaauw mechanism). If there is no relation between this initial velocity and the initial spin, then this pre-natal velocity may be added to the post-kick speed in quadrature. The main effect is to blur the correlations described below. If, however, there is a fixed relation between the orbital speed and the pre-kick spin or the kick itself, then this fourth angle must be introduced to the geometry. As these cases represent a small fraction of the single neutron star population, we ignore them here; however such considerations may be

important to descriptions of kicks for neutron stars presently found in binaries. We defer discussion of such models to a future communication.

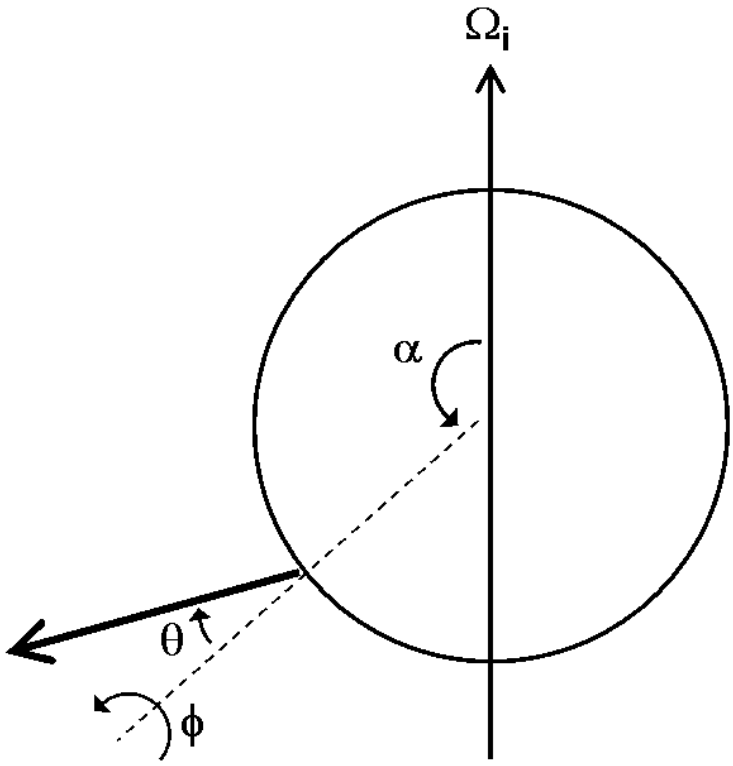

Figure 5.3 Geometry of the kick: α is the polar angle of the kick position, θ is the off-axis angle of the kick from the surface normal, ϕ is the azimuth angle of the kick about the normal, Ω_i is the pre-kick angular velocity.

During the kick, directions of $\vec{r}$ and $\vec{F}_\nu$ evolve according to the rotation

$$\hat{r}\,' = \mathcal{R}\hat{r}$$

$$\hat{F}'_\nu = \mathcal{R}\hat{F}_\nu$$

where the rotation matrix $\mathcal{R}$ is given by

$$\mathcal{R} = \begin{pmatrix} \Omega_x^2 + (1-\Omega_x^2)\cos\delta & \Omega_x\Omega_y(1-\cos\delta) - \Omega_z\sin\delta & \Omega_x\Omega_z(1-\cos\delta) - \Omega_y\sin\delta \\ \Omega_x\Omega_y(1-\cos\delta) - \Omega_z\sin\delta & \Omega_y^2 + (1-\Omega_y^2)\cos\delta & \Omega_y\Omega_z(1-\cos\delta) + \Omega_x\sin\delta \\ \Omega_x\Omega_z(1-\cos\delta) - \Omega_y\sin\delta & \Omega_y\Omega_z(1-\cos\delta) + \Omega_x\sin\delta & \Omega_z^2 + (1-\Omega_z^2)\cos\delta \end{pmatrix},$$

$\vec{\Omega} = \Omega\hat{\Omega} = \Omega(\Omega_x, \Omega_y, \Omega_z)$ is the angular velocity and $\delta = \Omega\Delta t$ is the angle that the star rotates in time Δt.

Given a set of initial conditions, the above equations can be integrated numerically to obtain the kick velocity, initial spin period and alignment angle. Note that in this paper, we call the initial pulsar spin period P_0 which is the value right after the kick. The pre-kick spin is denoted by P_i (Ω_i), which is a specified parameter of the model.

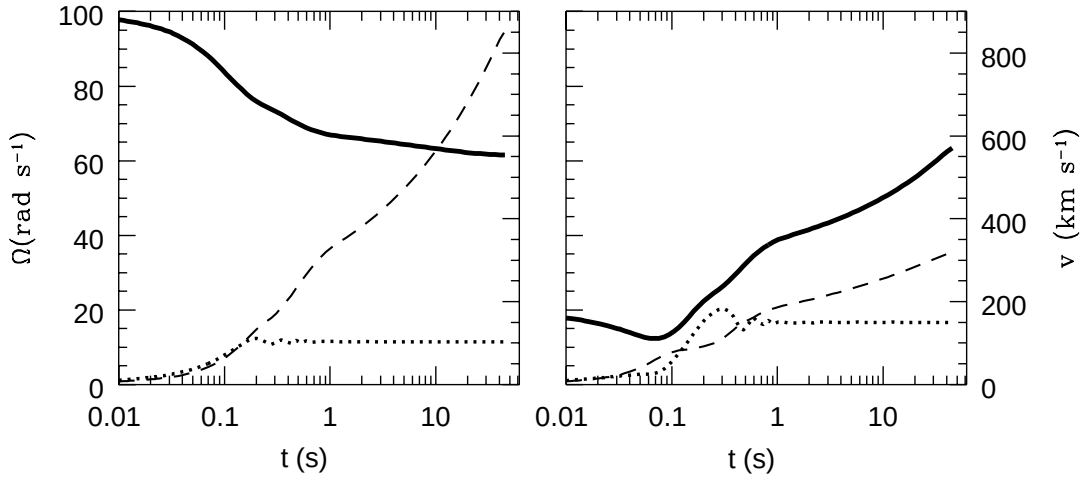

Figure 5.4 kick integrations with identical parameters except $\Omega_i = 100$ rad s^{-1} (*left*) and $\Omega_i = 30$ rad s^{-1} (*right*). The solid lines follow the instantaneous angular momentum, plotting the equivalent angular velocities with the moment of inertia at its final value. The dashed and dotted lines are the parallel and perpendicular components of the space velocity with respect to the instantaneous spin direction.

Figure 5.4 shows two example integrations with identical initial parameters except for the pre-kick angular velocity Ω_i. The kick is against the initial spin with a component along the surface, thus the angular velocity decreases. However, with $\Omega_i = 30$ rad s^{-1}, the right panel shows that the torque from the kick is large enough to perturb the spin axis to a new direction, where the kick is more effective in spinning up the proto-neutron star. Note that the initially fast spinner ends up nearly aligned, while the slow spinner is closer to orthogonal. Thus, even though

the post-kick spin periods P_0 are quite similar in the two models, information about the pre-kick spin is encoded in the vector direction of $\vec{\Omega}_0$.

5.3 Pulsar Sample

Linear and angular momenta are relics of neutron star birth and, if well preserved, can provide important probes of the core collapse physics. Given their vector nature, the alignment angle between them is an important observable. As discussed above, this is particularly sensitive to the kick timescale and geometry and can thus give unique information on the kick dynamics. While objects with measurements of all three observables (velocity v, initial spin period P_0 and alignment angle $\vartheta_{\Omega \cdot v}$) are rare, the correlations between these are particularly powerful at testing the models.

Only recently have improved pulsar observations made such comparison possible. For example, VLBI astrometry provides unprecedentedly high precision proper motion measurement (e.g. Brisken et al. 2002; Chatterjee et al. 2005). Also, pulsar timing observations (Hobbs et al. 2004; Zou et al. 2005) have recently provided additional (albeit often more uncertain) proper motion values. Altogether these provide several dozens of useful proper motion measurements. On the other hand, the pulsar spin direction projected on the sky plane has been inferred from the radio polarization profile by adopting the rotating vector model, although uncertainty in the emission mode leads to an inherent $\pi/2$ ambiguity. Recently, Johnston et al. (2005) obtain the spin orientations of 25 pulsars from radio polarization observations and noted significant alignment with the pulsar velocities. Wang et al. (2006a) reanalyze archival polarization data and arrive at similar conclusions. Next, the discovery of X-ray jets and torus structure in PWNe provides an even more powerful (and largely model-independent) way to obtain the pulsar spin orientation for a modest number of objects. Ng & Romani (2004) developed a method of pulsar wind torus fitting to measure the 3-D (not projected!) orientation of the spin axis. So for the vector (2-D) speeds and spin orientation, progress has been good. In contrast, pulsar initial spin periods remain very difficult to estimate. Currently, only a handful of pulsars have initial spin period estimates (e.g. Table 7 in Faucher-Giguère & Kaspi 2006).

As it happens, most of these have PWN structure indicating their spin orientations, but many do not have a precise proper motion measurement. In some cases, we can make an estimate of the space velocity from the structure of the associated SNR, but we must be cautious in applying such model-dependent values.

To select a sample of pulsars with 2-D velocities, we start from the list of pulsar proper motions from Hobbs et al. (2005), selecting young isolated pulsars with $> 2\sigma$ proper motion measurements. A few objects are added or updated with new measurements (e.g. Chatterjee et al. 2005; Zou et al. 2005; Ng & Romani 2006). Galactic acceleration can affect the trajectories of old pulsars, so we restrict our sample to $\tau < 5$ Myr (we also have included the interesting pulsar PSR B1133+16, which at $\tau = 5.04$ Myr is just above this limit). Also, differential Galactic rotation can add appreciably to the observed space velocity of distant pulsars. When the precise distance is unknown, this can cause large errors in reducing the speed and position angle to the local standard of rest. Accordingly, we restrict our sample to $d < 3$ kpc for pulsars with velocities from astrometric or timing analysis. Table 5.1 lists the pulsar samples used in this study. The first group of 20 objects have only transverse velocity measurements, hence they are called '1-D pulsars'. The next group, referred to as '2-D pulsars', have both a velocity and a projected spin alignment angle. For IC 443 and PSR B1800−21 the spin orientations are obtained from X-ray PWNe, all other 14 spin measurements are from radio polarization observations (Johnston et al. 2005; Wang et al. 2006a). As noted, the proper motions, must be corrected to the birth local rest frame for comparison with the spin directions, as this may affect the position angle by several degrees. Finally, the last group consists of 9 '3-D pulsars' which have estimates in all 3 observables, namely the velocities, initial spin periods and alignment angles, thus allowing for a full vector comparison. These pulsars place the strongest constraints on the model parameters.

Table 5.1: Pulsar sample used in the analysis.

Pulsar	v (km s^{-1})	Δv[a](km s^{-1})	$\vartheta_{\Omega\cdot v}$ (°)	P_0 (ms)	ζ(°)	Ref.
1-D Pulsars						
B0114+58	190	±63	···	···	···	···
B0136+57	300	±68	···	···	···	···
B0355+54	61	+12/-9	···	···	···	···
B0402+61	653	±121	···	···	···	···
B0450+55	175	+20/−19	···	···	···	···
B0458+46	72	±33	···	···	···	···
B0540+23	215	±78	···	···	···	···
J0633+1746	128	±3	···	···	···	···
B0656+14	60	+7/−6	···	···	···	···
B0736−40	238	+200/-23	···	···	···	···
B0834+06	157	+20/−19	···	···	···	···
B1702−19	330	±152	···	···	···	1
B1749−28	630	±280	···	···	···	1
B1818−04	129	+21/-21	···	···	···	···
B1848+13	204	+25/−25	···	···	···	···
B2020+28	256	+114/−61	···	···	···	···
B2021+51	115	+18/−15	···	···	···	···
B2022+50	244	±33	···	···	···	···
B2217+47	337	±74	···	···	···	···
B2224+65	1605	+193/-188	···	···	···	···
2-D Pulsars						
B0628−28	318	+61/-64	5 ± 4	···	···	2
B0740−28	259	+190/-149	7 ± 5	···	···	2
B0823+26	189	+55/-34	21 ± 7	···	···	3
B0835−41	170	±30	13 ± 11	···	···	3
B0919+06	506	±80	32 ± 17	···	···	3
B1133+16	639	+38/-35	22 ± 2	···	···	2
B1325−43	597	±254	31 ± 22	···	···	3
B1426−66	150	+40/-24	5 ± 9	···	···	2
B1449−64	219	+55/-18	1 ± 3	···	···	2
B1508+55	1082	+103/-90	23 ± 7	···	···	3,4
B1642−03	160	+34/-32	26 ± 5	···	···	2

Continued on Next Page...

Table 5.1 – Continued

Pulsar	v (km s^{-1})	Δv[a](km s^{-1})	$\vartheta_{\Omega\cdot v}$ (°)	P_0 (ms)	ζ(°)	Ref.
B1800−21	347	+48/-57	7 ± 8	···	90 ± 2	6
B1842+14	512	+51/-50	5 ± 15	···	···	2
B1929+10	173	+4/-5	16 ± 2	···	···	2
B2045−16	304	+39/-38	3 ± 6	···	···	3
IC 443	250	±50	45 ± 10	···	···	5
			3-D Pulsars			
J0205+6449	838	±251	21 ± 10	60 ± 10	91.0 ± 0.2	6
B0531+21	140	±8	26 ± 3	19 ± 2	61.3 ± 0.1	6
J0537−6910	634	±50	3 ± 5	12 ± 4	92.8 ± 0.8	6
J0538+2817	407	+116/-74	12 ± 4	139 ± 2[b]	···	6
B0540−69	1300	±612	34 ± 33	38 ± 2	93.7 ± 5	6
B0833−45	61	±2	10 ± 2	30 ± 20	63.6 ± 0.1	6
B1706−44	645	±194	35 ± 10	70 ± 10	52 ± 2	6
J1833−1034	125	±30	16 ± 15	58 ± 3	85.4 ± 0.3	6
B1951+32	273	±11	18 ± 5	27 ± 6	$\sim 90 \pm 30$	6

a – The errors in velocity are compiled from either the uncertainties in proper motion measurement, or distance estimates, whatever larger.

b – An uncertainty of 20 ms is used in the calculation, as to represent a group of slow spin objects.

References: Unless specified otherwise, all pulsar velocities are from Hobbs et al. (2005) and references therein. (1) Zou et al. (2005); (2) Johnston et al. (2005); (3) Wang et al. (2006a); (4) Chatterjee et al. (2005); (5) Gaensler et al. (2006); (6) – see text.

We have checked the consistency of the three subsets of pulsars, comparing their velocity and alignment angle distributions with the Kolmogorov-Smirnov (K-S) test. The K-S statistics indicates a probability of 0.34 that the velocities of the '1-D' and '2-D pulsars' are drawn from the same distribution. Comparison of the '3-D' samples with the summed '1-D' and '2-D' ones gives a similar value of 0.33. For the alignment angle, the probability of having the same distribution for the '2-D' and '3-D' pulsars is 0.48. Since the samples are relatively small, these tests are not very stringent but at least there is no evidence that the different measurement methods introduce significant biases in to the sample properties.

We next summarize the status of the several of the particularly interesting '3-D pulsars'.

Crab Pulsar (PSR B0531+21) Ng & Romani (2006) have measured the pulsar's proper motion with *HST* astrometry and compared with the spin vector, which was obtained from pulsar wind torus fitting (Ng & Romani 2004). The initial spin period is derived from the historical age, measured braking index and spin parameters (Manchester & Taylor 1977).

Vela Pulsar (PSR B0833−45) Tracing back the motions of dense supernova ejecta knots, Aschenbach, Egger, & Trümper (1995) inferred a supernova explosion site $14\farcm9 \pm 7\farcm2$ away from the pulsar's current position. With the updated pulsar proper motion from Dodson et al. (2003a), the kinematic age of the system is then $\tau = 20 \pm 10$ kyr. Using the measured braking index of $n = 1.4 \pm 0.2$ (Lyne et al. 1996), an initial spin period of 30 ± 20 ms is estimated. PA of the pulsar spin axis is obtained by torus fitting (Ng & Romani 2004).

PSR B0540−69 Based on the estimated pulsar age from the SNR expansion velocity (Reynolds 1985), Manchester et al. (1993) suggest an initial spin period of 38.7 ms. The velocity of the pulsar has an initial estimate by Serafimovich et al. (2004) using *HST*/WFPC2 images. For the pulsar spin, Ng & Romani (2007, in preparation; see Chapter 4) fit the X-ray pulsar wind torus to obtain its orientation.

PSR J0538+2817 Ng et al. (2007) report a VLBA astrometric measurement of the pulsar proper motion. They also discovered symmetric structure around the source in the X-ray observation, which, if interpreted as polar jets or pulsar wind torus, indicates the spin axis. From the offset of the pulsar position with respect to the SNR geometrical center, Romani & Ng (2003) argued for a long initial spin period, which was confirmed by Kramer et al. (2003) with the timing proper motion results and strengthened by the precise VLBA proper motion measurement (Ng et al. 2007).

PSR B1951+32 The pulsar proper motion is determined by VLBA astrometry (Migliazzo et al. 2002). Assuming the pulsar was born at the center of the shell CTB 80, the authors deduced the pulsar age and its initial spin period. Hester (2000) argue that the Hα lobes observed in the *HST* image correspond to pulsar

polar jets, which indicates its spin orientation. Radio polarization measurements could provide a valuable test of this hypothesis.

PSR J0537−6910 The X-ray PWN observation shows bar-like extended structure around the pulsar. The symmetric structure, if interpreted as pulsar equatorial outflow, indicates the pulsar spin vector. Ng & Romani (2007, in preparation; see Chapter 4) apply pulsar wind torus fitting to measure the PA of the symmetry axis. The pulsar birth site may be inferred from the radio image (Fig. 3 in Wang et al. 2001), where the peak of the PWN radio emission is at $\alpha = 05^{\rm h}37^{\rm m}44\overset{\rm s}{.}5(5)$, $\delta = -69°10'11''(2)$ (J2000). Then, adopting the kinematic age of 5 kyr (Wang & Gotthelf 1998), the pulsar velocity is 630 km s^{-1}. While the initial spin period is unknown, with its current $P = 16$ ms we can safely assume the pulsar had a P_0 range of $8 - 16$ ms.

PSR J1833−1034 Camilo et al. (2006) suggest a young kinematic age $\lesssim 1000$ yr for the pulsar, which implies an initial spin period of $P_0 \gtrsim 55$ ms. They also estimate the PA of the pulsar spin axis from the ellipticity of the PWN. Ng & Romani (2007, in preparation; see Chapter 4) fitted a model torus to the X-ray data and obtained similar results. Following Camilo et al. (2006), we found the geometrical center of G21.5−0.9 at $\alpha = 18^{\rm h}33^{\rm m}33\overset{\rm s}{.}4(3)$, $\delta = -10°34'12''(3)$ (J2000). If this is the explosion site, the offset from the pulsar position gives an estimated velocity of 125 km s^{-1}.

PSR J0205+6449 The *CXO* images of this pulsar in 3C58 have been noted as having a prominent central torus and polar jets, and fitting of these provides a robust spin position angle (Ng & Romani 2007, in preparation; see Chapter 4). The position of the pulsar birth may be inferred from the SNR radio expansion center to be at $\alpha = 02^{\rm h}05^{\rm m}31\overset{\rm s}{.}32(3)$, $\delta = +64°49'58\overset{''}{.}7(5)$ (J2000) (M. F. Bietenholz, private communication). Recently Gotthelf, Helfand, & Newburgh (2006) have identified a thermal X-ray shell in 3C58 with a similar center. If one assumes that 3C58 is the remnant of SN 1181, one gets an initial pulsar spin of 60 ms (Murray et al. 2002) and a rather large velocity of ~ 840 km s^{-1}. The X-ray and radio evidence, however, suggest an older age of $3000 - 5000$ yr. This would imply a shorter initial P_0 and a transverse velocity of $\sim 140 - 230$ km s^{-1}. While we plot values for

the commonly assumed 825 yr age, these values and the pulsar's status as a '3-D object' are certainly open to question. A pulsar proper motion would resolve these difficulties.

PSR B1706−44 A clear equatorial torus and polar jets were found in *CXO* data by Romani et al. (2005), where a robust spin position angle and inclination were fit. This pulsar is often associated with the SNR shell G343.1−2.3; comparing the total energy of the SNR and PWN, Romani et al. (2005) suggested $P_0 = 60-80$ ms. Also, if born at the geometric center of the SNR shell, the pulsar velocity is ~ 650 km s^{-1}. However, the PWN morphology and interstellar scintillation velocity limits make such a high speed questionable. Uneven SNR expansion could, for example, make the birth site much closer. Again, an interferometric pulsar proper motion would be particularly valuable.

PSR B1800−21 Radio images spanning ~ 10 years give an astrometric proper motion measurement of the pulsar with an accuracy of 2.5 mas yr^{-1} (Brisken et al. 2006). The Chandra X-ray observation shows symmetric PWN structure around the pulsar, which is fitted by Ng & Romani (2007, in preparation; see Chapter 4) to measure the spin orientation. However, no initial spin estimate is available for this pulsar.

PSR J1124-5916 While the PWN image in the initial *CXO* HRC observation showed noticeable ellipticity (Hughes et al. 2003), this axis was not clear in a subsequent ACIS exposure. A scheduled deep ACIS observation could help to resolve this structure. A PWN axis would be quite useful here as a robust proper motion axis and a reasonable age and P_0 estimate are available from the highly symmetric parent SNR.

5.4 Simulations

With our pulsar samples defined, we are now ready to constrain the kick models. We proceed by making Monte Carlo realizations of a given kick model, drawing pulsar spin and kick parameters and kick angles from the model distribution, simulating many pulsar realizations (by integrating according to the equations in §5.2.2) and

projecting onto the sky plane to produce the observables for comparison with the pulsar sample. The comparison for a given set of true pulsars is made using a maximum likelihood estimate of the probability of getting that observed set from the Monte Carlo model.

Of course, any physical model will have a distribution of values for the kick parameters rather than single values. What we attempt to extract from our comparison with the observed pulsars are the characteristic values in these distributions. For the kick geometry, we assume no preferential directions in the kick position α and the azimuth angle ϕ, hence $\cos\alpha$ and ϕ are distributed uniformly between -1 to 1 and 0 to 2π respectively. The off-axis angle θ is, however, a more interesting parameter as it is potentially related to the kick mechanism. Assuming the kick follows a Gaussian distribution around the surface normal, θ is characterized by the dispersion σ in the Gaussian. Many authors (e.g. Hobbs et al. 2005) fit the pulsar velocity distribution with a Maxwellian. We adopt this form for the momentum asymmetry η, with characteristic value η_0. We also attempted to use a simple Gaussian but this did not give a good distribution for the observed velocities; apparently, the larger Maxwellian tail is important for matching the observed sample. For the pre-kick angular velocity Ω_i, we assume a Gaussian distribution with mean $\bar{\Omega}$. To minimize the fit parameters, we take the dispersion as $\bar{\Omega}/3$. The value used Ω_i represents the angular frequency that the star with the same momentum will have after the proto-neutron star shrinks to its final radius. Our toy model approximates the time profile of the momentum kick as being proportional to the rapidly falling neutrino cooling light curve. A convenient way of introducing a characteristic kick time scale into the problem is by a delay to the 'turn-on' of the asymmetry, here parameterized as an exponential with a time constant τ. This has the added advantage of approximating some reasonable physical scenarios for asymmetry growth. However, as the asymmetry occupies a smaller fraction of the momentum flux in the light curve tail, the effective η must grow. To avoid focus on this strong correlation, we thus report the equivalent asymmetry $\bar{\eta}$ here, which corresponds to the same total thrust for

the case of $\tau = 0$, i.e.

$$\bar{\eta} \int L_\nu(t)\, dt = \eta_0 \int [1 - \exp(-t/\tau)]\ L_\nu(t)\, dt\ .$$

In brief, the kick model is characterized by the 4 'fitting parameters': η_0, $\bar{\Omega}$, τ and σ. The thrust is given by

$$F_\nu(t) = [1 - \exp(-t/\tau)]\ \eta\ L_\nu(t)/c$$

and the kick parameters are distributed as

$$\begin{aligned}
\alpha, \phi &\sim \text{isotropic} \\
\tfrac{dN}{d\eta} &\propto \eta^2 \exp(-\eta^2/2\eta_0^2) \\
\tfrac{dN}{d\Omega_i} &\propto \exp\left[-\tfrac{(\Omega_i - \bar{\Omega})^2}{2(\bar{\Omega}/3)^2}\right] \\
\tfrac{dN}{d\theta} &\propto \sin\theta \exp(-\theta^2/2\sigma^2)\ .
\end{aligned}$$

The factor $\sin\theta$ above accounts for the area in polar coordinates. In the simulation, the approximation $\sin\theta \approx \theta$ is taken to simplify the calculations. Also we tabulate the asymmetry results as $\bar{\eta}$, as noted above.

Given a set of fitting parameters, the kick velocity and spin vectors of $N_{\rm sim} = 2 \times 10^5$ pulsars are simulated. As the pulsar radial velocity is not an observable, the data samples are essentially only projected 2-D values on the sky plane. Therefore, the simulation results have to be projected before comparing to the observations. This is done by specifying 2 angles: the inclination angle ζ of the spin axis to the sky plane, and the azimuth angle ϕ_v of the velocity about the spin vector. While the latter is totally random, ζ is sometimes actually known from pulsar wind torus fitting. In the simulation, each of the simulated vectors are projected $N_{\rm proj} = 50$ times, according to the measured ζ (and its error) of an individual pulsar in the sample if this is known, or isotropically otherwise.

In order to compare the model prediction to measurements, we define a likelihood

function similar to the typical χ^2 statistic

$$\mathcal{L}_\xi^{ij} \sim \exp\left[-(\xi_{\rm obs}^i - \xi_{\rm sim}^j)^2/2(\sigma_\xi^i)^2\right] \ .$$

For an observable $\xi \in \{v, P_0, \vartheta_{\Omega\cdot v}\}$, $\xi_{\rm obs}^i$ is the i-th sample pulsar's measurement with uncertainty σ_ξ^i and $\xi_{\rm sim}^j$ is the j-th simulation result. For the initial spin periods P_0 and velocities based on the DM-estimated distance, uncertainties in the measurements are dominated by systematic errors which do not follow Gaussian properties. In this case, a boxcar function is used

$$\mathcal{L}_\xi^{ij} = \begin{cases} 1 & \text{if} \quad \left|\xi_{\rm obs}^i - \xi_{\rm sim}^j\right| \leq \sigma_\xi^i \\ 0 & \text{otherwise} \end{cases} \ .$$

For each pulsar in the data sample, the likelihood function is then the product of all its observables, averaged over the simulations and projections

$$\mathcal{L}^i = \frac{1}{N}\sum_j^N \left(\prod_\xi \mathcal{L}_\xi^{ij}\right) \ ,$$

where $N = N_{\rm sim} \times N_{\rm proj}$. Finally, the total likelihood function is the product of all the pulsars in the data sample

$$\mathcal{L} = \prod_i^{N_{\rm obs}} \mathcal{L}^i \ .$$

It is convenient to define a Figure-of-Merit (FoM) function for comparison between different models. As usual, it is defined as the negative log of the likelihood function FoM$= -\log\mathcal{L}$.

5.5 Results

Figures 5.5–5.7 show the projections of the likelihood function of our three kick scenarios for the model parameters. Each panel shows four curves, with the minimum

indicating the best-fit parameter values. The solid curve shows results obtained using all the objects in our pulsar sample; this generally has the tightest, best-defined minimum. However, as discussed in §5.3, some of the spin and velocity estimates for certain '3-D objects' are quite model-dependent and can be questioned. We therefore also ran the FoM calculations with a 'minimal' set of '3-D pulsars': the widely accepted Crab and Vela pulsars and PSR B0650−69, which is simple, but has large statistical error bars. The results are very similar to those for the full set, albeit with larger uncertainties. Finally, we ran fits with the '1-D' and '2-D' objects together and just the '1-D objects' alone. Again, the fits are broadly consistent with the full set's results, but as expected the minima are poorly constrained. Thus, we confirm that our handful of well measured '3-D objects' dramatically improve our knowledge of the birth kick properties, but apparently do not introduce major biases into the fits.

Our likelihood function is unnormalized. Since it is a product over individual objects, it is convenient to rescale the values for the curves computed for different sets of pulsars. This removes the gross scaling of FoM with number of objects and facilitates cross-comparison. In practice the results with different object sets are normalized by dividing all by the corresponding best-fit FoM values for the 'ν-transport' model for the same data set. Note that, with the exception of the '1D+2D' (dashed line) fit to the static model, all minima occur at FoM > 1. Also the 'ν-transport' model has narrower minima. This means that this model, in addition to being the most physical, provides the best description of the full data set of the three scenarios tested.

It is useful to understand how the '1-D objects' can provide some model constraints, i.e. how the pulsar velocity distribution is sensitive not only to the asymmetry η, but to the other kick parameters, as well. To illustrate, consider the case of large σ or small $\bar{\Omega}$, i.e. when kick-induced spin is important. When the pulsar is spun up, the induced linear and angular momenta are always orthogonal. In this case, the rotational averaging is efficient, generating many low velocity pulsars. In contrast, for large $\bar{\Omega}$ or nearly normal kicks (i.e. small σ), the initial spin sets the averaging axis, and the final velocity is principally determined by the kick location.

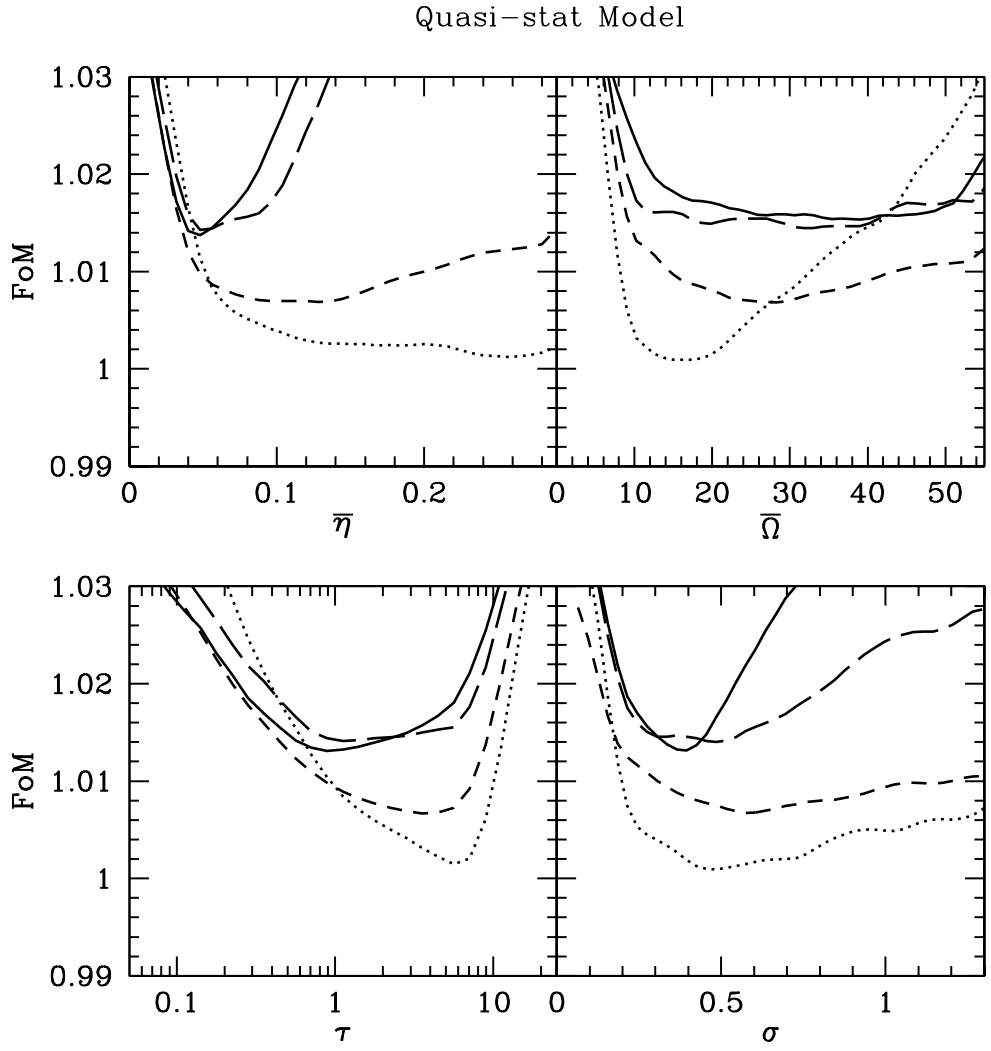

Figure 5.5 Projected FoM for individual parameters of the 'quasi-stationary' model. The solid lines show the full sample fit; the long dashed lines show the fit with '1-D' + '2-D' + 'minimal set' of '3-D' pulsars (i.e. Crab, Vela and B0540−69); the short dashed lines show the fit with only '1-D' + '2-D' pulsars; the dotted lines show the fit with only '1-D pulsars'. Smoothing filters have been applied to the curves and the FoM scale has been normalized by the minimum 'ν-transport' value for each data set.

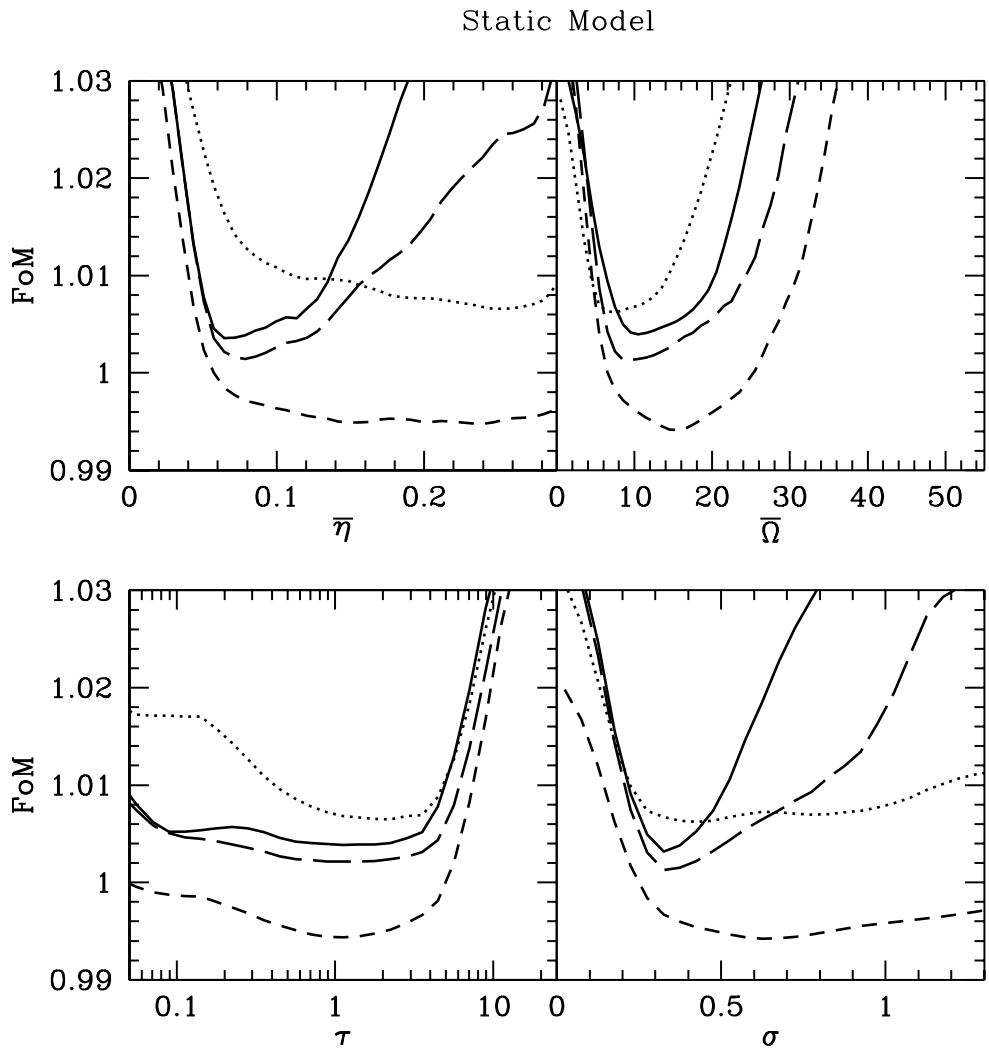

Figure 5.6 Same as Fig. 5.5, for the 'static' model.

For example, a polar kick results in a fast moving pulsar, while an equatorial kick is quickly averaged to give a low final speed. Thus, for fast initial spinners, the kick velocity distribution becomes relatively uniform, as our model assumes no preferential kick direction. This is unlike the observed velocity distribution.

Table 5.2 reports the best-fit parameters for the models, obtained from the lightly smoothed curves in Figure 5.5 – 5.7, with 1σ confidence intervals estimated from

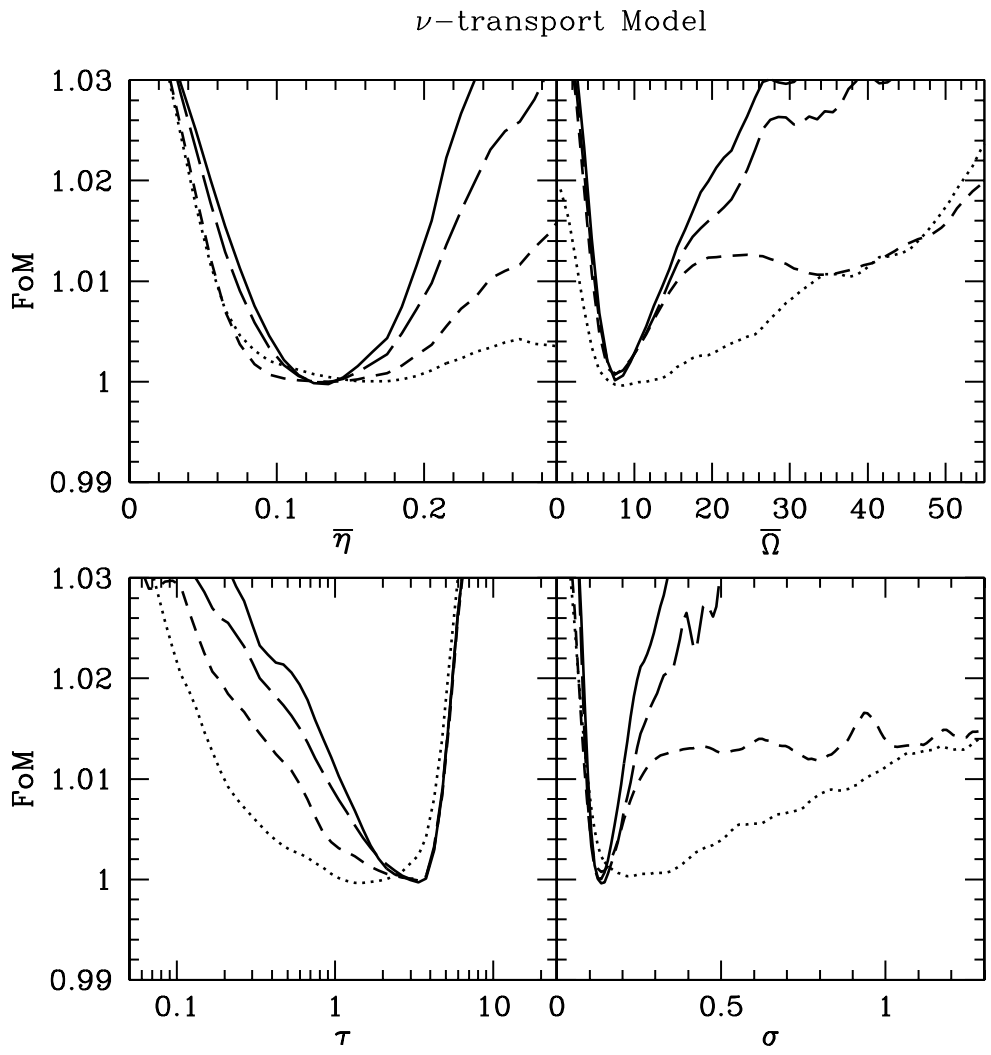

Figure 5.7 Same as Fig. 5.5, for the 'ν-transport' model.

the bootstrap percentiles (Efron & Tibshirani 1993). We generated 10^5 bootstrap samples and quote 1σ errors from the standard normal 68% interval of the bootstrap replica distribution. To be conservative, we quote here the 'projected' multi-dimensional errors on all the model parameters. The single-parameter errors are, in general, significantly smaller.

Table 5.2. Best-fit parameters of the models.

	$\bar{\eta}$	$\bar{\Omega}$	τ	σ
Quasi-stationary				
Full Sample	$0.05^{+0.01}_{-0.03}$	26^{+50}_{-11}	$0.9^{+1.8}_{-0.7}$	$0.39^{+0.17}_{-0.17}$
Minimal Set	$0.05^{+0.03}_{-0.03}$	36^{+33}_{-21}	$1.4^{+2.7}_{-1.1}$	$0.5^{+0.4}_{-0.2}$
1D+2D	$0.13^{+0.04}_{-0.10}$	30^{+16}_{-10}	4^{+2}_{-3}	$0.6^{+0.6}_{-0.17}$
1D	$0.24^{+0.03}_{-0.21}$	13^{+10}_{-3}	5^{+3}_{-5}	$0.5^{+0.6}_{-0.13}$
Static Model				
Full Sample	$0.07^{+0.02}_{-0.02}$	9^{+10}_{-3}	$1.0^{+1.2}_{-0.9}$	$0.32^{+0.09}_{-0.18}$
Minimal Set	$0.07^{+0.04}_{-0.03}$	9^{+11}_{-3}	$0.8^{+1.5}_{-0.7}$	$0.32^{+0.28}_{-0.13}$
1D+2D	$0.13^{+0.14}_{-0.04}$	14^{+7}_{-4}	$1.4^{+0.7}_{-1.3}$	$0.6^{+0.5}_{-0.17}$
1D	$0.18^{+0.37}_{-0.09}$	7^{+3}_{-5}	$2.3^{+1.4}_{-2.1}$	$0.4^{+0.5}_{-0.24}$
ν-transport				
Full Sample	$0.13^{+0.02}_{-0.06}$	7^{+1}_{-3}	$3.3^{+0.4}_{-1.5}$	$0.12^{+0.03}_{-0.03}$
Minimal Set	$0.13^{+0.03}_{-0.07}$	8^{+16}_{-3}	$3.3^{+0.3}_{-2.4}$	$0.14^{+0.19}_{-0.03}$
1D+2D	$0.13^{+0.07}_{-0.06}$	7^{+27}_{-3}	$3.5^{+0.1}_{-2.5}$	$0.13^{+1.2}_{-0.03}$
1D	$0.17^{+0.15}_{-0.07}$	8^{+7}_{-5}	$1.4^{+1.8}_{-0.6}$	$0.19^{+0.6}_{-0.06}$

Of course, when only velocity values are available, there is a large co-variance between the model parameters, leading to a broad minimum in the multi-dimensional (projected) FoM curve. In fact, it is the handful of '3-D objects' that break these degeneracies and best localize the minima, as the FoM curves illustrate. Even then, there are significant correlations in the fit parameters, as illustrated by Figure 5.8. The points show the loci of the minimum in two dimensional cuts through parameter space for the ν-transport model. Similar results are obtained for the other models. To be conservative, we quote here the 'projected' multi-dimensional errors on all the model parameters. The single-parameter errors are, in general, significantly smaller. Table 5.2 reports the best-fit parameters for the models, with 1σ confidence intervals estimated from the bootstrap percentiles (Efron & Tibshirani 1993). We generated 10^5 bootstrap samples and quote 1σ errors from the standard normal 68% interval of the bootstrap replica distribution. The two dot sizes in Figure 5.8 show the loci of the '1σ' and '2σ' minima.

There are some robust trends in the fitting results. All four of our basic model parameters are significantly constrained and, with the exception of τ in the 'static' model, they have significantly non-zero values. Thus, we conclude that in all of our scenarios a finite pre-kick spin and a finite tangential component to the kick are required. In some sense, we consider the 'ν-transport' model to be the most physical. The best parameters for this model are closer to those of the static model than to the shrinking 'quasi-stationary' model. Thus, the kick is somewhat insensitive to the initial envelope shrinkage of the 'ν-transport' model. However, it should be noted that the 'ν-transport' model strongly prefers a finite $\tau \sim 3$ s. This *ensures* that the kick is insensitive to the initial large envelope phase. Interestingly, if τ is forced to be small for this model the best fit $\bar{\eta}$, $\bar{\Omega}$ and σ move much closer to the preferred 'quasi-stationary' values (Fig. 5.8). In this limit, the kick is dominated by the large-radius initial phase of the cooling curve.

The final angular velocity (after the proto-neutron star cooling and kick) has a very broad distribution, which peaks at ~ 120 rad s^{-1} for the 'ν-transport' model. Similar results are obtained for the other models. With the pre-kick spin Ω_i of only $10 - 30$ rad s^{-1}, this indicates that most of the spin is induced by the kick, as

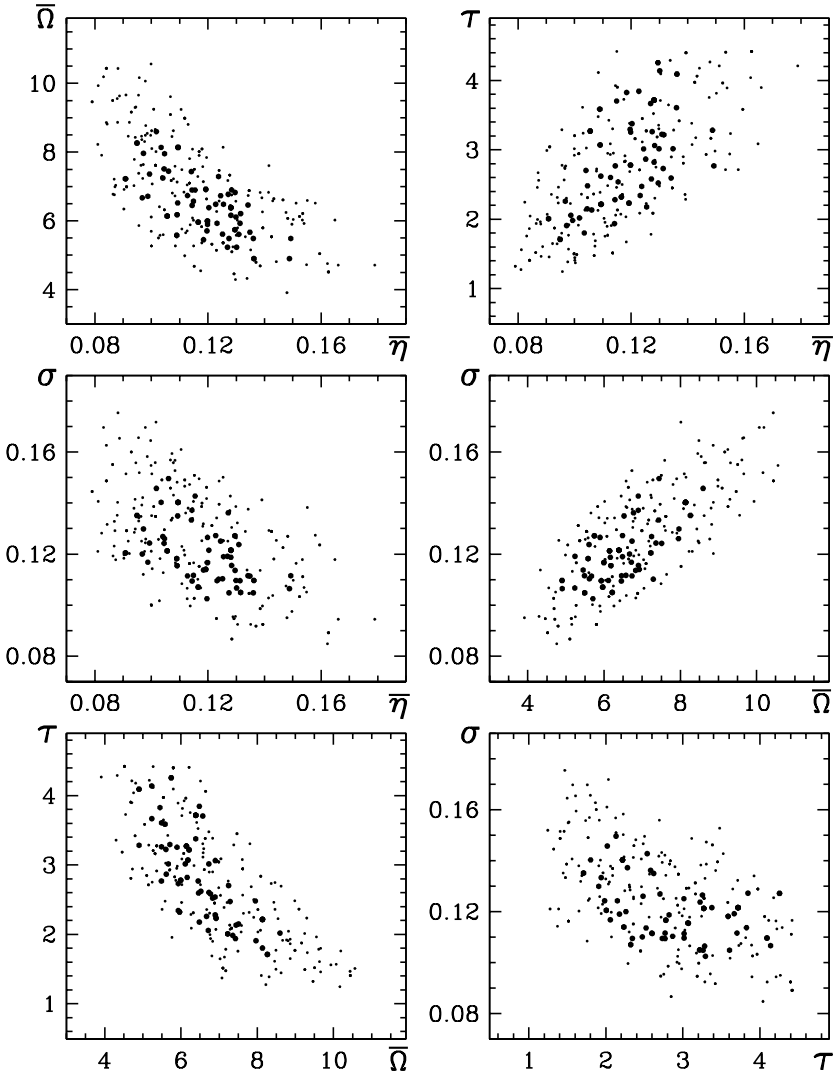

Figure 5.8 Correlations between fitting parameters for the best-fit ν-transport model with full data sample. Large and small dots are simulations within 1 and 2σ of the best fit FoM. Note that significant correlations remain between the parameters and that our full projected errors are (conservatively) larger than the single parameters uncertainties.

suggested by Spruit & Phinney (1998). Unfortunately, so few initial spin estimates are available at present that the post-kick spin distribution cannot yet be compared with the data.

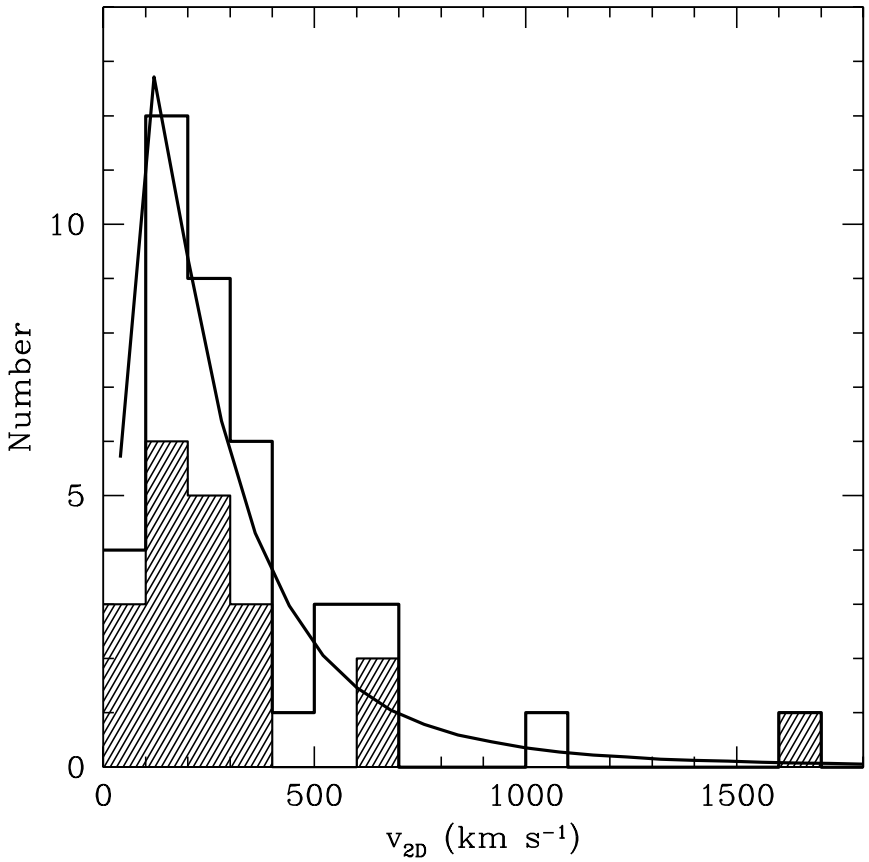

Figure 5.9 Velocity distributions of the best-fit ν-transport model with the full data set, compared to the observed pulsars with proper motion measurements of $> 2\sigma$ significance. The '1-D pulsars' are shaded.

The distribution of final velocities for the best-fit ν-transport model with full sample is plotted in Figure 5.9. The observed velocities represent reasonable draws from that model, with a K-S probability of 0.3, although the model predicts some additional low velocity pulsars. Similarly, Figure 5.10 shows the model and data distributions of the alignment angles. The left panel compares the model angle distribution and the data. This is the alignment angle range that is actually used

in the fits. The K-S statistic gives a moderately poor fit with a probability of only 0.08 that the data and model have the same distributions. Note, however that the '2-D pulsars' with angles determined by polarization have, by fiat, $\vartheta < 45°$, so in the right panel we fold the model curve back to $\vartheta < 45°$. The data match this distribution very well, with the K-S probability increased to 0.98. If our model is correct, about 20% of the '2-D' ϑ values should be $> 45°$. Note also that a few of the '3-D' measurements have large errors and values $> 45°$ are allowed. We have tested this by randomly drawing $\sim$3 of the '2-D pulsars', flipping the table values to $\vartheta = 90° - \vartheta$, and re-fitting. The majority of the draws produce, as expected, best-fit parameters close to our adopted values, but deeper and tighter minima.

5.6 Discussion

We have explored the effect of a single kick applied at a random but fixed point on the surface of a rotating, cooling proto-neutron star. This is a reasonable direct description of a class of models where neutrino anisotropy is imposed by a structure (e.g. magnetic) locked in the underlying neutron star. It is also a reasonable stand-in for other physical models where e.g. convection is controlled by a hot spot on the stellar surface. We note that our modeled momentum thrust can be considered as the net anisotropy of any number of kicks, as long as the anisotropy maintains a fixed pattern and follows the evolving core luminosity. Our models do not directly address the effects of multiple, completely random thrusts, but as first described by Spruit & Phinney (1998) and as confirmed in recent model integrations of Wang et al. (2006b), multiple kicks tend to wash out any anisotropy; the net effect of a large number of kicks is to produce little or no correlation between motion and spin, contrary to recent observations. Our simulations also do not directly test the gravity-driven kicks described by Scheck et al. (2006) since for a rotating star these are almost certainly directed at the pole. Their scenario also does not include the kick-induced spin and rotational averaging described here.

While our model is certainly a simplified parameterization of real physics, it does produce some surprisingly complex behavior that can be discerned in the real

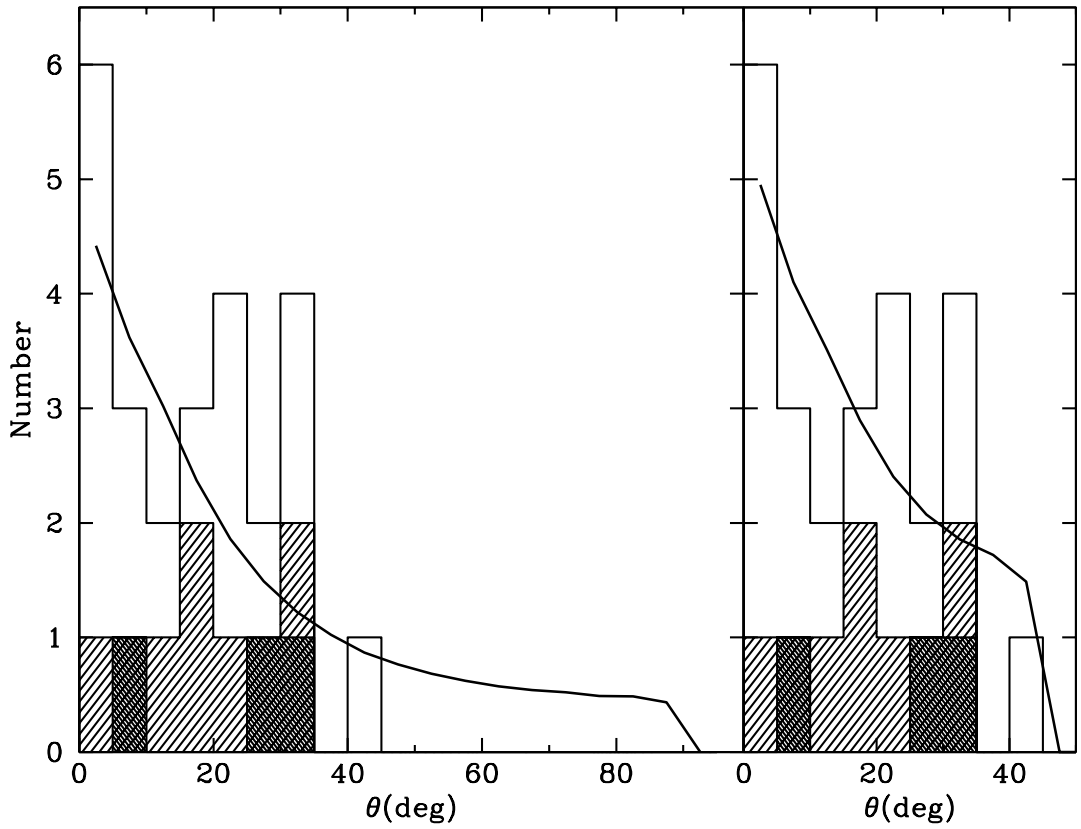

Figure 5.10 Alignment angles of the pulsar samples compared to the best-fit ν-transport model with the full data set. The '3-D objects' and the 'minimal set' are shaded in light and dark gray respectively. *Right:* Simulations are folded around 45° to illustrate the effects of the 90° ambiguity in alignment angles measured by radio polarization.

pulsar data. The most interesting effects are only visible in the '3-D pulsars', objects for which we have multiple observables and can measure their correlation within the population. Consider, for example, the projected angle $\vartheta_{\Omega \cdot v}$ vs. the post-kick initial pulsar spin frequency Ω_0 (Fig. 5.11). The model distribution shows that at intermediate initial spin periods $40 - 60$ ms we expect a substantial fraction of pulsars to be misaligned, with $\vartheta_{\Omega \cdot v} > 45°$. This is because during the kick, the spin was slow enough that the initial impulse induced the bulk of the spin, at orthogonal angles. In contrast, short spin period pulsars ($P_0 < 20$ ms, $\Omega_0 > 200$ rad s^{-1}) tend

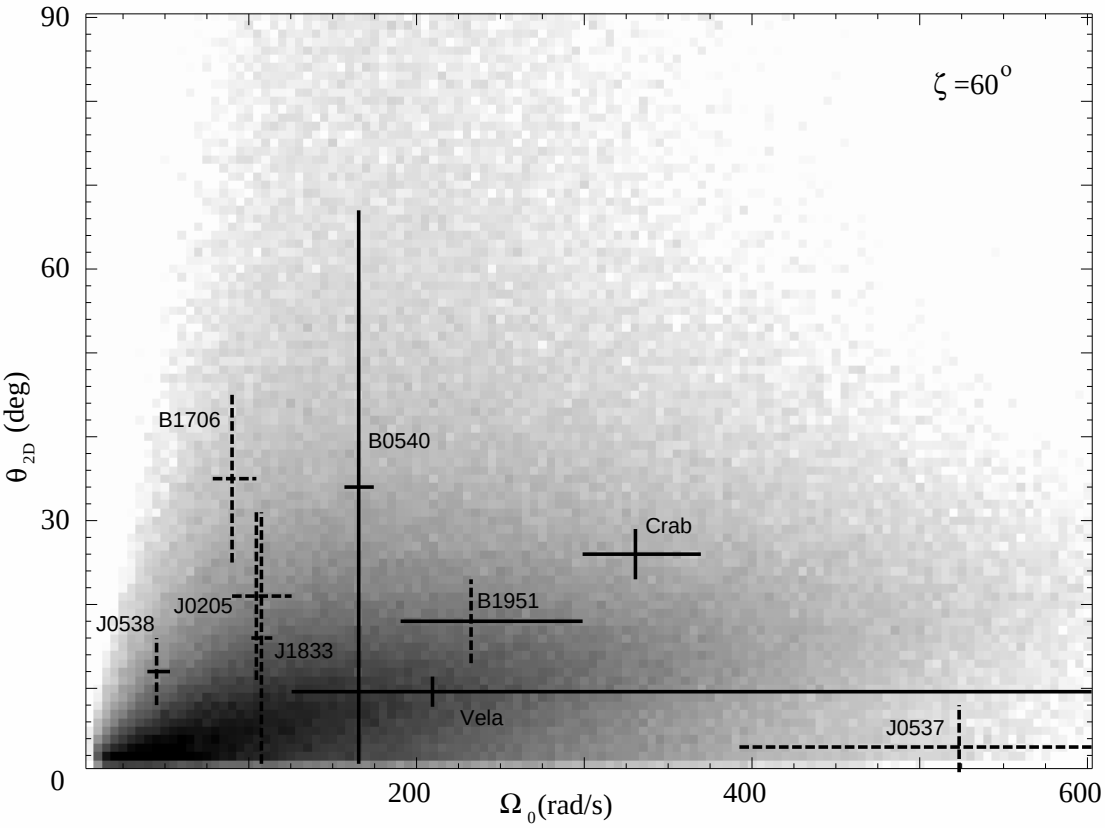

Figure 5.11 Distribution of alignment angle $\vartheta_{\Omega \cdot v}$ vs. post-kick initial spin Ω_0 for the best-fit ν-transport model with the full data set. The simulations are projected for $\zeta = 60°$, a typical value for the '3-D pulsars'. For these pulsars, measurements with model-dependent assumptions dominating the errors are shown by plotting the corresponding error flags in dotted lines.

toward alignment due to spin averaging, and very long period pulsars ($P_0 > 100$ ms, $\Omega_0 < 60$ rad s^{-1}) are also aligned. The latter effect is 'survivorship'; to retain a slow spin even with a decent kick the pulsar must have started as a slow spinner *and* have been kicked nearly radially. Similar correlations exist with the pulsar velocity, e.g. the fastest moving pulsars are expected to be slow spinners (Fig. 5.12): if the initial kick produces a large spin then continued thrust 'averages away' and the pulsar never reaches high speeds.

While considering the 2-D correlations, it is interesting to look at the alignment-velocity correlation (Fig. 5.13). Here we may include many of the RV-model pulsars.

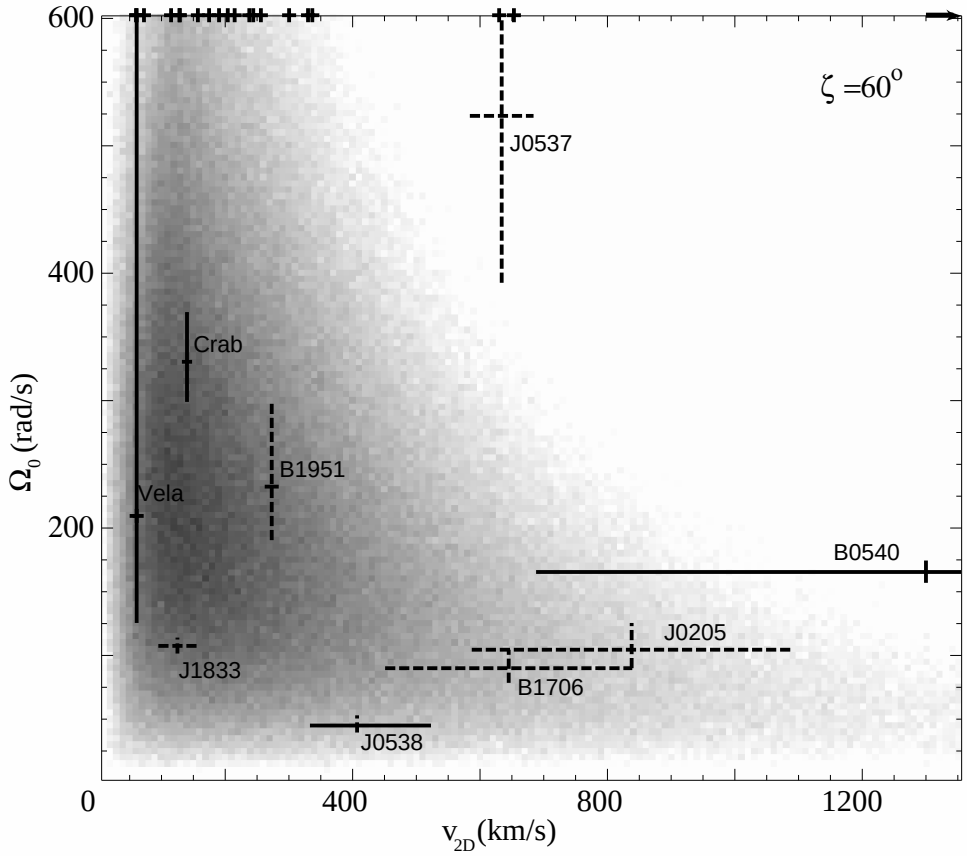

Figure 5.12 Distribution of pulsar post-kick initial spin vs. velocity for the best-fit ν-transport model with the full data set. The simulations are projected for $\zeta = 60°$. The velocities of the '1-D pulsars' are marked at top. Again, systematic-dominated parameters of '3-D objects' have dotted-line error bars.

It is not clear that these objects follow the expected correlations. First, there appears a dearth of misaligned pulsars at slow speeds. However, two effects may explain this. First, truly slow movers are selected against in the data sample as they are unlikely to have either a significant astrometric or timing proper motion. Second, we should remember that all RV pulsars have been *forced* to have $\vartheta_{\Omega \cdot v} < 45°$. It is possible that at least a few of the slower pulsars are in fact orthogonal. What about the pulsars at large space velocity in this plot? Well, the model suggests that these should show good alignment. Two of the '3-D' pulsars PSRs B1706−44 and J0205+6449 in 3C58

show surprisingly large $\vartheta_{\Omega \cdot v}$ for their speed. However, note that the speed plotted for PSR J0205+6449 assumes a birth date of CE 1181. If, as appears increasingly likely, the pulsar is actually $\geq 3,000$ years old (Gotthelf, Helfand, & Newburgh 2006), then the object falls near the peak of the expected distribution. Similarly, the large velocity inferred for PSR B1706−44 depends on travel from the present remnant center. Scintillation measurements suggest a much slower speed, requiring an asymmetric SNR or even non-association; these again put the pulsar near the peak of the model distribution. Further note the large error bar on the alignment angle of PSR J1833−1034 in G21.5−0.9. This is set by the uncertainty in setting the SNR expansion center position. It would not be very surprising if this object, as well as the neutron star CXOU J061705.3+222127 in IC 443, would appear at $\vartheta_{\Omega \cdot v} > 45°$.

Recall that for the 2-D polarization objects, set to $\vartheta_{\Omega \cdot v} < 45°$ by fiat, we might expect that 3−4 are actually at large ϑ, emitting in the opposite polarization mode. This would not, of course, significantly dilute the general trend noted by e.g. Johnston et al. (2005). that RV model fits correlate with proper motion vectors. It is not clear if we will be able to understand the radio emission well enough to remove this $\pi/2$ ambiguity. Happily the direct X-ray PWN fits do not suffer this problem, so more such measurements should expose a few poorly aligned objects. Globally, we expect fast pulsars to be well aligned. Slow pulsars will have a significant fraction of poorly aligned objects. Note that additional velocity components, e.g. orbital velocity for pulsars released from binaries, will enhance this trend.

Are there any serious challenges to our proposed model? Well, yes. PSR B1508+55 is fast and has a relatively large $\vartheta_{\Omega \cdot v} = 23° \pm 7°$. This is very difficult to produce with the sort of kick scenarios that we describe. We would predict that improved spin measurements would prefer smaller $\vartheta < 15°$. If a large misalignment perseveres, some amendment is needed to the kick scenario.

What about the substantial velocities which may arise naturally due to convection, when $m = 1$ modes dominate (Scheck et al. 2006)? These kicks make *vector* predictions differing from those modeled here. For example, these authors suggest that fast spinners produce strong $m = 1$ modes and thus only these attain high

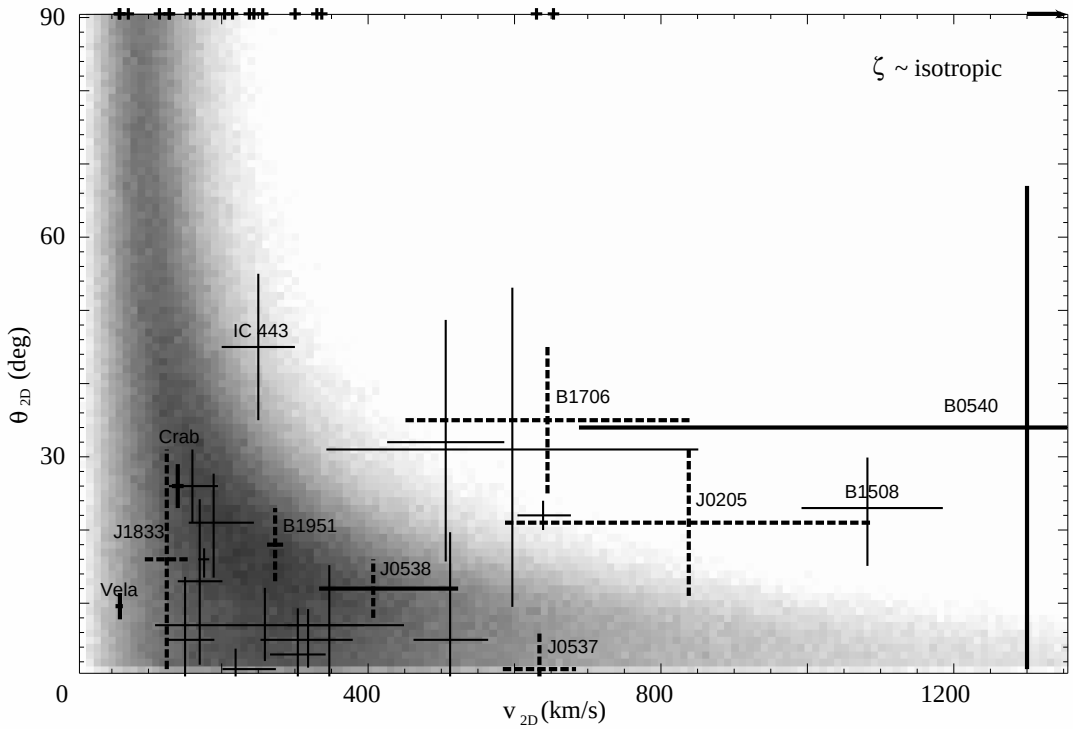

Figure 5.13 Distribution of alignment angle vs. kick velocity for the best-fit ν-transport model with the full data set. Here we can plot many '2-D pulsars', so the simulations are projected isotropically. The velocities of the '1-D pulsars' are plotted on the top. '2-D objects' are plotted by the thin lines. Measurements of '3-D objects' have thick-lined error bars, with dotted lines for those parameters dominated by model-dependent systematics.

space velocities (opposite to the pattern of Fig. 5.12). Also, they suggest that slow spinners ($\lesssim 60$ rad s^{-1}) should be poorly aligned (cf. Fig. 5.11). This picture may also produce a bi-modal distribution of pulsar speeds; it is presently unclear if such bimodality exists, but this would be a important test of the model. Perhaps the most interesting *vector* test of this downflow kick scenario should come from binary pulsars, where a rotation-controlled $m = 1$ mode predicts a kick along the binary orbit normal. We have not discussed binary kicks in this paper, deferring to a future publication.

Also, we should at least comment on the physical plausibility of our fit values. The effective asymmetry $\bar{\eta}$ is quite large. If this were strictly induced at the neutrino

photosphere, this would represent a large asymmetry. In the simple magnetic field picture this requires very large (although possibly transient) fields of $\sim 10^{15.5-16}$ G. Thus, a momentum asymmetry mediated by coupling to matter would be quite appealing, as the field requirements are lower. The pre-kick spin periods are, as noted above, generally quite low. This argues for effective core-envelope coupling, possibly magnetic, in the pre-collapse progenitor (Spruit & Phinney 1998). What about the modest $\sigma \approx 0.2 - 0.4 \approx 10^\circ - 20^\circ$ angle of the kick to the normal? This does seem quite natural in a magnetically-induced asymmetry model, where a dipole centered at $\sim R_{\rm NS}\sigma/2$ would cause such an angle. Pictures where the kick is due to matter fall-back, would tend to accrete matter with a large specific angular momentum. While effective at re-spinning the star, this would tend to have a large $\sigma > 1$ and would, of course, suggest a strong trend to $\vartheta_{\Omega \cdot v} \sim 90^\circ$, which are not observed.

Finally, we come to the time delay in the kick asymmetry. Since the initial neutrino flux falls off exponentially, the delay τ can be thought of as selecting a characteristic timescale for the momentum thrust. As already noted, this has a strong covariance with the kick amplitude and with the pre-kick spin Ω_i, with small delays requiring smaller kicks and faster spins. For example the best-fit 'static' model is consistent with no delay and has $\Omega_i \approx 10-15$ rad s^{-1}. The quasi-stationary model prefers a ~ 1 s delay and has $\Omega_i \approx 20 - 40$ rad s^{-1}. Interestingly all the fits to proper motion data alone prefer some substantial delay, implying that long kicks and significant rotational averaging are useful in producing the observed velocity distribution. Finally, the 'ν-transport' model very strongly excludes the no-delay solution. As noted above, this is required to avoid having the bulk of the momentum thrust while the star still has a large radius. What about the physical origin for this delay? In a picture where a large B field introduces the asymmetry, it is attractive to associate this field with early dynamo action in the proto-neutron star. Such dynamo theory is not well developed, but it is interesting that qualitative discussions (e.g. Thompson & Duncan 1993) suggest a characteristic time of $\sim 1-3$ s for a convectively-driven dynamo to drive the field to saturation. If η grows as $\sim 0.1 B_{15}(MeV/\bar{E}_\nu)^2$, then the kick gains in efficiency as the B field grows to its limit

and as the neutrinosphere temperature drops. Thus, the fit parameters, a delayed kick with modest tangential component and a slow-spinning pre-kick star, are quite consistent with our qualitative picture of a magnetic field induced asymmetry of a neutrino-driven kick. Only the large asymmetry fraction, implying a very large B field, stretches this scenario.

Chapter 6

Conclusions and Outlook

In this study we have investigated the pulsar kick problem from a kinematic point of view, with particular focus on the connection between pulsar linear and angular momentum vectors. The magnitudes, as well as the relative orientation of these two vectors provide important probes of the core collapse dynamics.

Proper Motion of the Crab Pulsar

Since the Crab pulsar is the index case for velocity-spin correlation, we checked the published value for its proper motion, finding substantial new results. Using over 6 years of archival *HST* WFPC2 observations and improved distortion corrections, we obtained a pulsar proper motion of $\mu_* = 14.9 \pm 0.8$ mas yr^{-1} at P.A. $278^\circ \pm 3^\circ$ in its LSR. At the nominal distance of 2 kpc, this corresponds to a space velocity of 140 ± 8 km s^{-1}. Our accurate results have uncertainties 3 times less than claimed in previous studies, and more importantly, rejects the previous value at the 5.7σ level. The pulsar velocity direction is at $26^\circ \pm 3^\circ$ to the nebular axis, which substantially relaxes constraints on the birth kick of this pulsar.

Pulsar Wind Tori Fitting

Previously, equatorial tori have been qualitatively described in several PWNe, but the geometry have not been measured. We have developed a pulsar wind torus fitting technique to extract the 3-D orientation of termination shocks from X-ray data. This method provides robust and nearly model independent estimates of the geometric parameters, and gives reliable measurements even for the case of sparse and Poisson-limited observations. In addition, we have also estimated the systematic and statistical errors in the fit quantitatively, allowing for the first time a comprehensive comparison with the model. Application to a dozen of PWN tori gives their orientations, shock scales and postshock wind speeds, along with confidence intervals in the parameters. This has taken the study of PWN geometry from the qualitative to quantitative level and shown the way to more fundamental studies of the pulsar wind physics.

Pulsar Kick Modeling

The improved data samples suggest a general alignment between pulsar velocity and angular momentum. This also allows us to investigate the pulsar kick physics, in particular to constrain the kick amplitude and timescale quantitatively. We studied a toy model where the pulsar kick is driven by accretion and cooling of the proto-neutron star, with the momentum thrust proportional to the neutrino cooling luminosity. For this simple model, simulations results suggest that an anisotropy of up to $\sim 10\%$ in the neutrino flux is required to match the observed data, along with a finite pre-kick spin of $10 - 20$ rad s^{-1}, a kick timescale of $1 - 3$ s and kick-induced spin. While the detailed fit values may depend on the model assumptions, we tried a range of models showing that the kick parameters hold in general. This gives important clues to the basic kick physics.

Outlook

Currently, there are only a handful of pulsars with precise measurements of spin vectors, a few more examples of spin-kick connection could substantially improve

the statistical significance and further constrain the kick physics. Therefore, continuing efforts to identify pulsar toroidal termination shock and jet structures in X-ray observations are essential. Although pulsar wind torus fitting is a powerful technique in measuring pulsar spins, it requires a fairly energetic young neutron with large spin down luminosity. In most cases, the PWNe are very faint and deep X-ray observations are needed. Therefore we do not expect the number of examples to increase dramatically in near future. In principle, radio polarization observations present a more promising technique, since it could be applied to many radio pulsars. Then careful calibrations could reveal their spin orientations. However, this technique is still phenomenological and the underlying physics is not yet fully understood. In particular, the $\pi/2$ ambiguity significantly impairs its power to constrain the kick models. It is hoped that the pulsar wind torus fitting could provide some insights into the problem. The few pulsars having spin measurements from both X-ray PWNe and radio polarization provide important calibrations to the rotating vector model. Obtaining more examples in the future allows a better comparison. Also, the 3-D spin orientation from the torus fitting helps to study the polarization profiles and provides a better understanding of the fundamental pulsar physics.

Another application of the torus fitting technique is to obtain the viewing geometry for Gamma-ray pulsar studies. High energy Gamma-ray emissions have been detected from young neutron stars. In the model of Romani & Yadigaroglu (1995), the radiation originates from the outer magnetosphere and the pulse profile depends sensitively on the viewing geometry. Therefore, having a reliable measurement of the pulsar orientation is essential to verify the theories. The torus fitting technique is particularly valuable in this case, as it provides quantitative measurements of the pulsar spin axis inclination to the sky plane. This is a powerful tool to obtain the viewing geometry which strongly constrains the models. With the Gamma-ray Large Area Satellite Telescope (GLAST) mission anticipated in 2007, we expect to detect several hundreds of Gamma-ray pulsars with detail pulse profiles. Some of them are expected to have associated PWNe which could indicate the pulsar orientation, allowing a comparison of the pulse profiles to the models.

For the study of pulsar kick models, we investigated a simple neutrino kick scenario to illustrate the basic kick physics. In future studies, our analysis could be improved by considering more physical assumptions, such as taking into account the effects of multiple kicks or the proto-neutron star's initial velocity. As discussed in the previous chapter, our study only focused on single kick, however it is also possible that the neutrino anisotropy changes rapidly with time, resulting in multiple kicks which occur randomly. In this case, it is generally believed that the correlation between linear and angular momentum vectors would be washed out (Spruit & Phinney 1998; Wang et al. 2006b). Including the possibility of multiple kicks in our simulation could help confirm that. Another simplification we made in the simulation is neglecting the pre-kick neutron star velocity. Although it has been shown that the Blaauw mechanism could not solely account for the observed pulsar velocity, there is a modest fraction of pulsars released from binary systems during supernova explosion, the momentum imposed could contribute to the kick velocity significantly and affect the precise alignment. Tauris & Takens (1998) derived analytical formulae for the dynamical effects of binary disruption and showed the correlation between the orbital velocity of the progenitor and the neutron star's final velocity. As indicated in Figure 5.9, there is an excess of slow pulsars in our model. We believe that considering the effects of binary break-up would increase the mean velocity, and results in a better match to the observed velocity. In general, our simulation technique could be applied to further investigations of pulsar kicks where the anisotropy patterns are fixed, for example, the electromagnetic rocket effect, asymmetric emission of sterile neutrinos or even kicks due to matter fall-back.

As usual, more observations will provide improved tests of this picture. In particular we would like to obtain more robust X-ray image measurement of pulsars with low space velocities. Improved polarization sweep position angles for a larger data set will help, as well. However, the real key to progress is accurate measurements of proper motion vectors for more young pulsars, especially slow objects. This means that we need improved sensitivity to reach to higher distances and long baselines. High band-width VLBI studies extending over a decade are the key. To push to

larger distances, we will also want improved distance estimates to allow the ϑ measurements to be corrected for differential Galactic rotation. The real challenge in collecting more '3-D pulsar' measurements is the difficulty in estimating initial spin periods. While some estimates may be obtained from SNR and PWN modeling (e.g. van der Swaluw & Wu 2001), most will require either historical remnants or very regular objects with high precision expansion ages. There are not many such objects and measuring braking indices and precise proper motion for these will not be easy. However, with improved X-ray measurements for robust orientations, improved radio measurements for polarization and motions and improved population modeling, we can hope for a more refined exploitation of this new probe of neutron star birth dynamics.

Appendix A

The Pulsar Wind Torus and Jets of PSR B1706–44

This chapter is based on "The Complex Pulsar Wind Torus and Jets of PSR B1706−44", Roger W. Romani, C.-Y. Ng, Richard Dodson & Walter Brisken 2005, ApJ, 631, 480.

A.1 Introduction

PSR B1706−44, discovered by Johnston et al. (1992) is among the most interesting pulsars for study at high energies. It is one of a handful of pulsars detected by EGRET in GeV γ-rays. It is quite similar to the Vela pulsar with a characteristic age $\tau_c = P/(2\dot{P}) = 1.7 \times 10^4$ yr and a spindown luminosity of $\dot{E} \approx 4 \times 10^{36}$ ergs s^{-1}, but is $\sim 10\times$ more distant at $d = 3d_3$ kpc. Early *Chandra* HRC/ACIS data provided a first detection of X-ray pulsations and showed a compact $\sim 10''$ surrounding pulsar wind nebula (PWN) (Gotthelf, Halpern, & Dodson 2002; Dodson & Golap 2002). More recent *XMM-Newton* spectroscopy (McGowan et al. 2004) has provided improved measurements of the X-ray spectrum and pulsations. Early claims that the PWN is detected in TeV γ-rays (Kifune et al. 1995; Chadwick et al. 1997) have not been supported by recent High Energy Stereoscopic System (H.E.S.S) observations (Aharonian et al. 2005).

PSR B1706−44 is superposed on a radio-bright spur of the supernova remnant G343.1−2.3, which has a similar, albeit unreliable, $\Sigma - D$ distance of $\sim$ 3 kpc (McAdam, Osborne, & Parkinson 1993). The pulsar DM gives a distance of 2.3 ± 0.3 kpc in the Cordes & Lazio (2002) model. Dodson & Golap (2002) have argued for an association. In particular, they found a faint southern extension of the SNR, which would place the pulsar within the full SNR boundary. They also noted an approximately N-S elongation of the X-ray PWN, pointing roughly back to the SNR center and argued that this would represent a trailed nebula. The required velocity for travel from the approximate geometric center of the SNR, about $12'$ away, was $\sim 1000 d_3/\tau_4$ km s^{-1} where τ_4 is the pulsar age in units of 10^4 yr. There are, however, some challenges to this SNR association. Koribalski et al. (1995) in an HI absorption study of the pulsar found velocity components setting lower and upper bounds for the distance of $d_{min} = 2.4 \pm 0.6$ kpc and $d_{max} = 3.2 \pm 0.4$ kpc. However a prominent HI emission feature seen in the bright limb of G343.1−2.3 at −32 km s^{-1} is not seen by Koribalski et al. in the absorption spectrum of the pulsar, suggesting that it lies in front of the SNR. Also scintillation studies (Nicastro, Johnston, & Koribalski 1996; Johnston, Nicastro, & Koribalski 1998) suggest a low transverse velocity for the pulsar, $v \leq 89$ km s^{-1}. This estimate has been supported by more recent scintillation measurements (S. Johnston, private communication). Thus the distances of the pulsar and SNR are still fairly uncertain. We adopt here a generic distance of 3 kpc in the discussion that follows, but carry through the scaling to show the distance dependence.

Ng & Romani (2004) re-examined the AO1 50 ks HRC and $\sim$ 15 ks ACIS-S exposures, and found that the compact PWN could be well modeled as an equatorial torus + polar jets, rather similar to the structures seen around the young Crab and Vela pulsars. They found that the brightest arc of PWN emission lay *behind* the pulsar's inferred motion from the SNR center, while a polar jet extended well in front of the pulsar position. This is difficult to reconcile with a bow shock/trail interpretation. On the other hand, the PWN symmetry axis did indeed point back to the SNR center, suggesting that a more careful evaluation of the connection was in order. This is particularly interesting, since comparison of the PWN symmetry

(= pulsar spin) and proper motion axes can constrain the origin of pulsar birth kicks (Spruit & Phinney 1998; Lai et al. 2001; Romani 2005).

We have obtained a deeper 100 ks ACIS-I exposure of PSR B1706−44 and its surroundings. The X-ray exposure coverage is compared to the overall geometry of G343.1−2.3 in Figure A.1. Together with new ATCA radio continuum imaging, we are able to study the rich structure in this PWN and further constrain its connections with the SNR.

A.2 Observations and Data Analysis

PSR B1706−44 was observed with the *Chandra* ACIS-I array (4 ACIS-I chips along with the S3 and S4 chips) on Feb 1-2, 2004 with standard imaging (3.2 s TE) exposures. The CCD array was operated in 'very faint' (VF) mode, allowing improved rejection of particle backgrounds. The total live-time was 98.8 ks and no episodes of strong background flaring were observed. Hence all data are included in our analysis. The pulsar was positioned near the standard aimpoint of the I3 chip and all observing conditions were normal. We have also compared our new exposure with the archival (Feb 3, 2001) 14.3 ks ACIS-S3 exposure (ObsID 0757). As usual the backside illuminated S3 chip suffered more from particle background and after cutting out periods of background flares, 11 ks of clean exposure remained. All analysis was performed using CIAO 3.2 and CALDB 3.0.0, including automatic correction for the ACIS QE degradation. These data were nearly free of pile-up; the maximum pixel counts at the pulsar position indicate only 2.5% pile-up while the best-fit model for the point source has an expected pile up fraction of $\sim 3.5\%$. For sources with low pile-up we can maximize the spatial resolution of the ACIS image by removing the standard pixel randomization and applying an algorithm correcting the position of split pixel events (Mori et al. 2001). This decreases the on-axis point-spread function (PSF) width in our data set by $\gtrsim 10\%$. These data are compared with radio observations of the PWN.

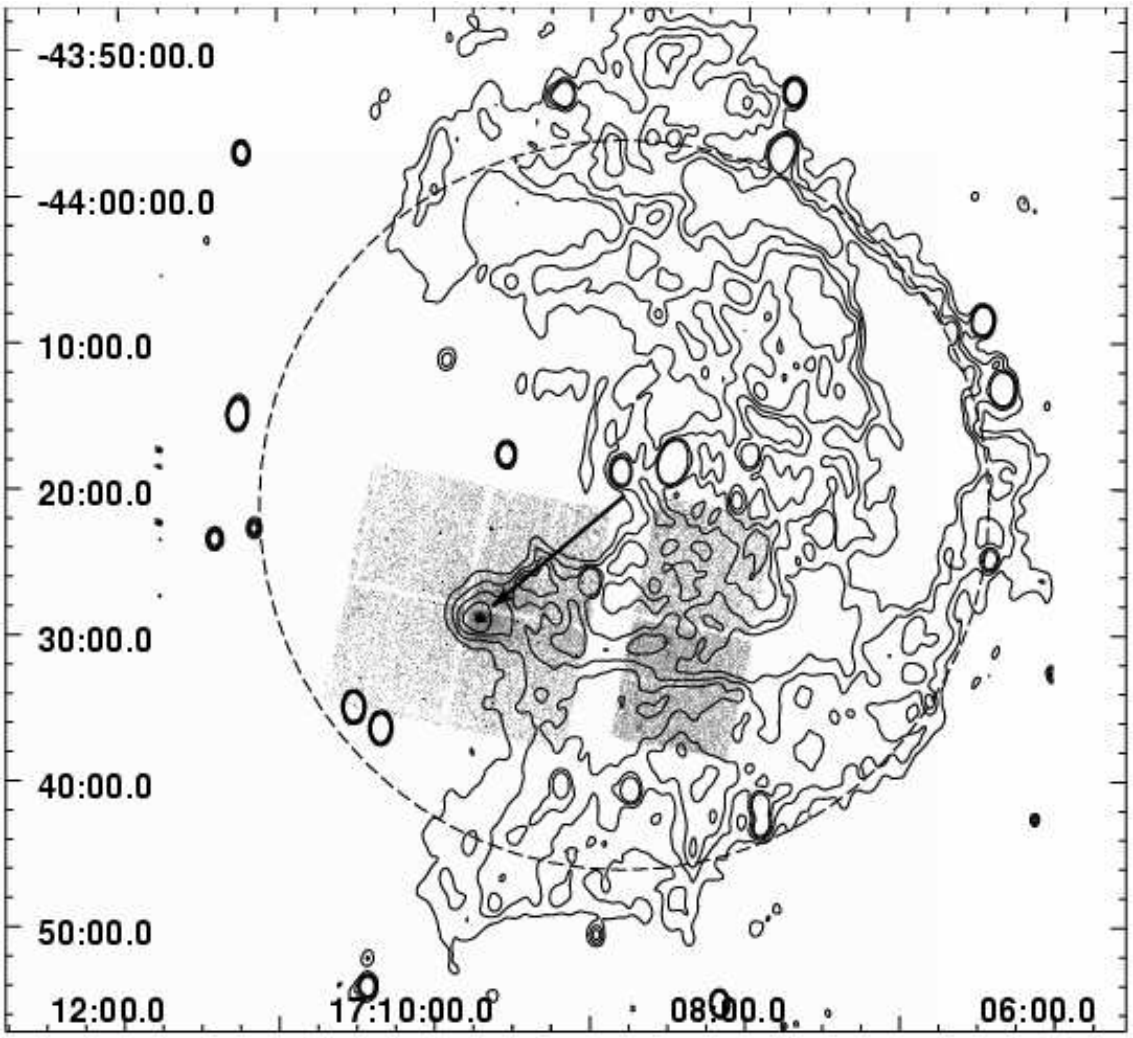

Figure A.1 Gray-scale image of our new ACIS-I pointing of PSR B1706−44. The contours (at 8, 10, 12 and 14 mJy beam^{-1}) show the shell of G343.1−2.3 from a 19 pointing 1384 MHz ATCA mosaic (Dodson & Golap 2002). The radio map has a resolution of $70'' \times 47''$ and an rms final map noise of 0.6 mJy. The X-ray PWN lies on a spur of radio emission. An approximate boundary of the full SNR ($25'$ radius) and an arrow for the inferred PSR motion, assuming birth at the SNR center, are shown.

A.2.1 Radio Imaging and Astrometry

Data for the radio maps shown here were collected at the Australia Telescope Compact Array (ATCA) in Narrabri (latitude $-30.^{\circ}3$) (Frater, Brooks, & Whiteoak 1992).

For the 1.4 GHz map in Figures A.1 and A.2, the data acquisition and analysis are described in Dodson & Golap (2002). For the image contours in Figure A.3, the data first presented in Dodson & Golap (2002) were re-imaged including the 6 km baselines and uniform weighting to highlight the high resolution features. The restoring beam size is $9\farcs0 \times 7\farcs8$. To show the nebular structure, an 11 mJy point source PSF has been subtracted at the position of the pulsar. Two maxima appear flanking the pulsar position. These are unlikely to be artifacts due to pulsar variability, as diffractive scintillation for this pulsar is particularly weak (Johnston, Nicastro, & Koribalski 1998). Since the data were collected in five sessions, spread over more than a year, it is in principal possible for slow refractive scintillation to change the pulsar flux between epochs and distort its PSF. However, each epoch used ∼12 hr of integration, so any residual epoch PSF should be close to circularly symmetric, in contrast to the structure near the pulsar which is clearly bipolar. Further observations, with pulsar binning, have been requested to confirm this result.

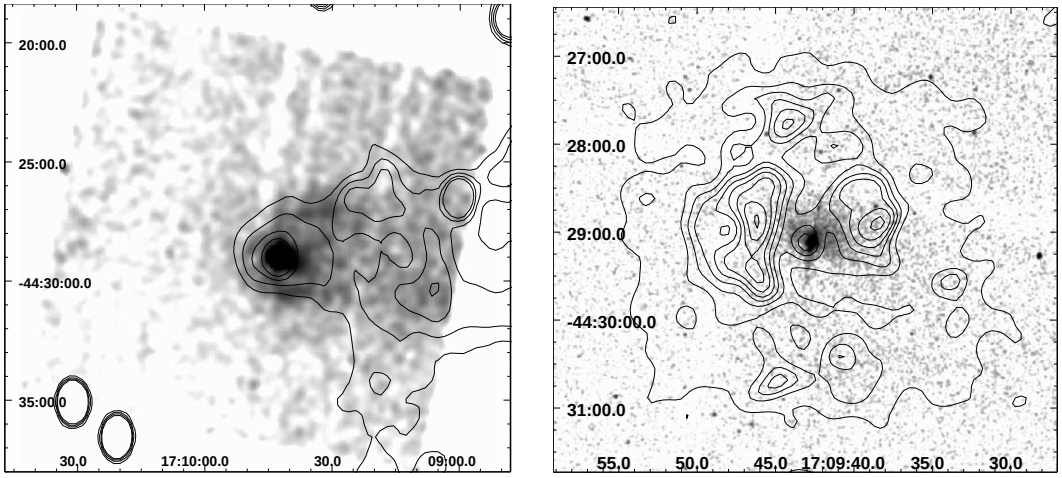

Figure A.2 *Left:* ACIS-I $1-7$ keV image with point sources (other than the pulsar) removed, exposure correction and $20''$ Gaussian kernel smoothing. Contours are from the 1.38 GHz radio map of Fig. A.1. *Right:* $1\farcs5$ Gaussian smoothed image of the PWN with an overlay of the core of the radio nebula from a 4.8 GHz ATCA image (contours at 0.4, 0.8, 1.0, 1.1, ..., 1.6 mJy beam^{-1}); the resolution is $20''$ and the image rms is 0.2 mJy beam^{-1}.

For the 4.8 GHz map in Figure A.2 (*right*), observations were made at 4.8 and

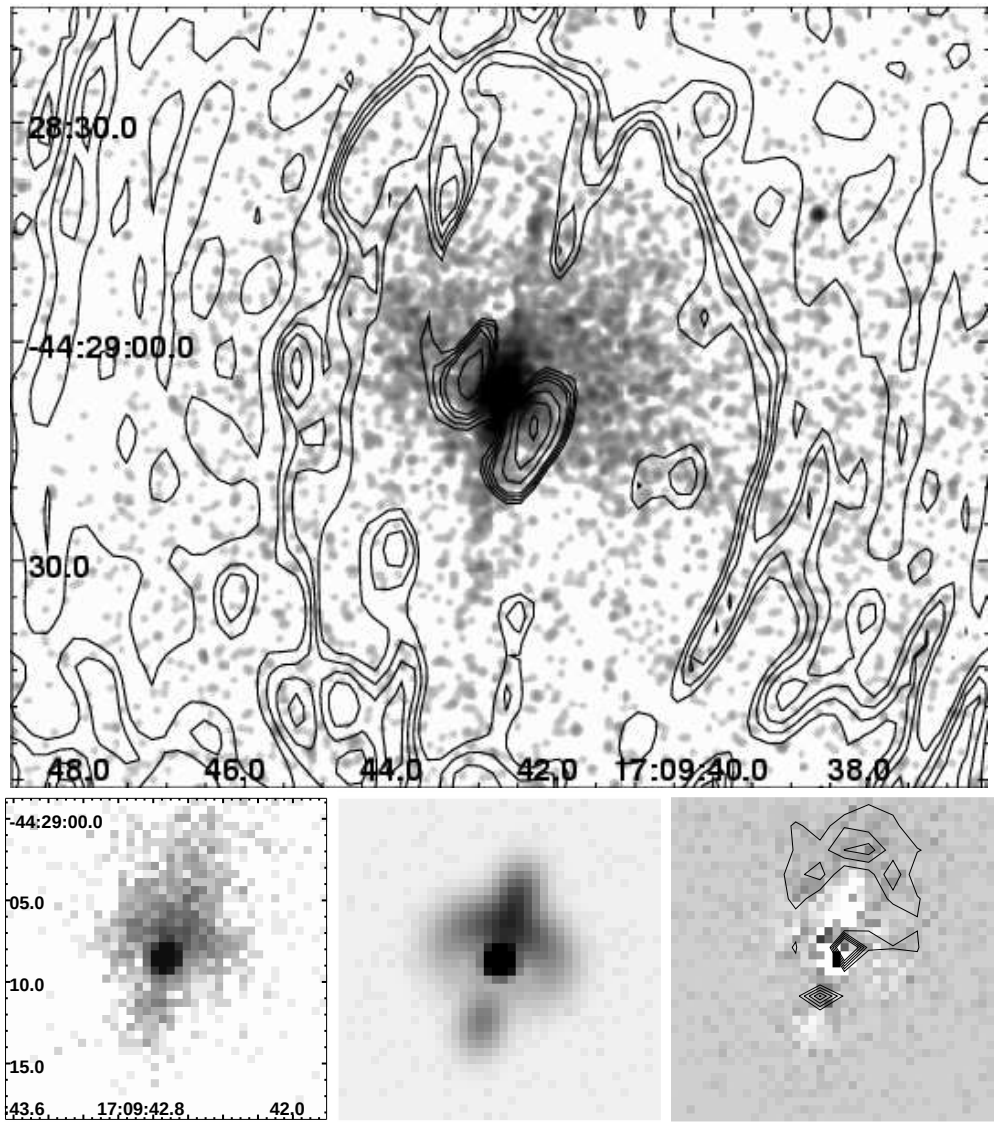

Figure A.3 *Top*: Grey scale image (1.″5 Gaussian smoothing) of the PWN, stretched to show the outer jets and the equatorial PWN. The contours (0.3, 0.4, 0.5, 0.6, 0.9, 1.2, 1.5 mJy beam^{-1}) are from the 1.38 GHz ATCA image, which has a map rms of 0.2 mJy beam^{-1} and a resolution of 9.″0 × 7.″8. The pulsar point source has been subtracted. Two peaks of radio emission bracket the torus. These lie in a cavity which surrounds the equatorial PWN and jets. *Bottom*: Grey scale image of the inner PWN (*left*) and of the best-fit point source+torus+(inner) jets model (Table A.1) to the same scale (*middle*). The residual image is shown (*right*), with contours indicating the excess counts above (North of) the torus.

8.6 GHz with the array in the standard configurations 0.75A, 1.5A and 6A on 06 Jan, 16 Feb and 11 Apr 2002. The maximum and minimum baselines for the 4.8-GHz data were 1 and 100 kλ (angular resolutions of $3\farcm4$ to $2\farcs1$) for a total of 26 hours observation. In all cases we observed the two frequencies with bandwidths of 128 MHz. We used the ATNF correlator mode that divides each integration's data into separate phase bins spanning the pulsar period. This firstly allowed the strongly pulsed point source flux to be excluded from the image and secondly allowed us to self-calibrate using the relatively strong point source flux from the pulsar. After data editing and calibrating we inverted the image with a *uv*-taper of $20''$ and deconvolved it with the full polarization maximum entropy task PMOSMEM in MIRIAD.

The most important test of the SNR association would, of course, be a direct astrometric proper motion. With a 1.4 GHz flux of $\sim$11 mJy, PSR B1706−44 is relatively bright. As such it is suitable for phase referenced VLBI astrometry, if an in-beam reference could be found. Unfortunately searches for phase references adequate for Australian Long Baseline Array (LBA) and US VLBA experiments have not detected comparison sources with compact fluxes greater than $\sim$ 1 mJy. Attempts were made at external phase reference VLBA astrometry. However at 1.4 GHz, the nearest known reference source ($2\farcs5$ away) was scatter broadened to $\sim$ 50 mas. With the strong ionosphere at such low elevation, the next nearest known source (10° away) is too distant for effective calibration. Since the pulsar spectrum is steep, an attempt at VLBA astrometry at 5 GHz was also unsuccessful; at this low elevation the system temperature was $4-5\times$ nominal and only six VLBA antennae could be used, reducing the sensitivity to $\sim$ 15% of nominal. So unfortunately we have only tied-array astrometry at present. Even if the pulsar does travel from the geometric center of G343.1−2.3, the expected proper motion is only $\sim$ 40 mas yr^{-1}; the existing time base of VLA/ATCA imaging does not yet allow a serious constraint on this motion. We must conclude that a direct proper motion measurement awaits substantially increased (SKA or EVLA) capabilities and a long-duration, large base-line experiment.

A.2.2 X-ray Spatial Analysis

To show the diffuse emission surrounding PSR B1706−44, we plot (Fig. A.2, *left*) a $1-7$ keV image with point sources removed (except the pulsar). These data are exposure corrected to minimize the chip gaps and heavily smoothed on a $20''$ scale. The diffuse emission is an edge-brightened, radius $\sim 110''$ cavity surrounding the pulsar with a faint extension to the west. Contours of the 1.38 GHz radio map show good correlation with the radio emission in the bar crossing G343.1−2.3 (Fig. A.1). We will refer to this structure as the 'nebula'.

Moving in toward smaller scale, in Figure A.2 (*right*) we show a $1-7$ keV image, smoothed with a $1\farcs5$ Gaussian. Point sources have not been removed. This shows that the cross structure fit by Ng & Romani (2004) extends across $\sim 1'$. Narrow X-ray jets, which we refer to here as the 'outer jet' (extending south) and 'outer counter jet' (extending north) start $\sim 10''$ from the pulsar and continue to $\sim 30''$. Bracketing these is faint diffuse X-ray emission which we will call the 'equatorial PWN'. For comparison we draw contours of a 4.8 GHz ATCA image with $21'' \times 18''$ restoring beam. These observations have the pulsar 'gated out' and show that the radio PWN has a hollow center bracketing the equatorial PWN. Diffuse radio peaks are, in fact, seen just east and west of this X-ray structure.

Finally, we show in Figure A.3 a lightly smoothed image of the central region of the PWN, stretched to bring out the faint outer jets. The contours are drawn from a 1.38 GHz ATCA image, where the 6 km baselines have been weighted to produce a $9\farcs0 \times 7\farcs8$ restoring beam. A point source PSF has been subtracted at the pulsar position. Two local radio maxima with peak fluxes ~ 2 mJy and ~ 2.5 mJy bracket the 'torus' structure. The radio then shows a sub-luminous zone surrounding the 'equatorial PWN'; beyond $\sim 30''$ the radio brightens again, as in figure 2b. No emission appears along the 'outer jets'. Indeed there appear to be evacuated channels in the radio emission, but improved S/N and resolution are needed to probe this sub-mJy structure. The frames on the right show the innermost region of the PWN with the best-fit torus + inner jet model (§A.2.3).

The overall geometry of the PWN is strongly reminiscent of that surrounding the Vela pulsar. In particular Pavlov et al. (2003) have described a series of ACIS images

of the Vela nebula which show a torus-like structure, an inner jet and counter jet and a faint narrow outer jet system. This imaging sequence showed that the Vela outer jet, which is patchy and strongly bent, varies dramatically on timescales of days to weeks. Apparent motion of blobs within the jets suggests mildly relativistic bulk velocities and strong instabilities. For PSR B1706−44 our single sensitive image does not let us comment on variability. However we argue that the relatively straight and narrow jets, $\sim 3\times$ longer than those of Vela, and symmetric PWN structure are a consequence of a static uniform external environment and a low pulsar velocity. At 1.4−8.5 GHz Dodson et al. (2003b) have found that the Vela PWN has two bright patches bracketing the X-ray torus and jets, in a structure quite similar to that in Figure A.2b. Polarization imaging of the Vela radio structure suggests that these two patches represent the limbs of a toroidal B field structure. This implies that the rotation axis controls the PWN symmetry to large radii.

A.2.3 Nebula Structure Fits

Following Ng & Romani (2004) we have fitted our new ACIS image to a point source PSF, Doppler boosted equatorial torus, polar jets and uniform background. The fitting minimizes residuals using a Poisson-based likelihood function. Monte Carlo simulations of Poisson realizations of the best-fit model are in turn re-fitted to generate statistical errors and their co-variance matrices. Table A.1 contains the best-fit values. The torus radius and axis inclination and position angles are r, ζ and Ψ, respectively. See Ng & Romani (2004) for the definition of the other parameters and the details of the fitting technique. In Table 1 the inner jet/counter-jet are constrained to lie along the torus axis in the fits.

In addition to the statistical errors, there are certainly systematic errors, in particular induced by unmodeled PWN components. For example, it is clear that there are counts in excess of the torus+jet model in a cap surrounding the inner counter-jet. Interestingly similar structure is seen in the Crab PWN. We have made an attempt to constrain the systematic biases by modifying the fitting model. For example, allowing the (inner) jet and counter-jet to have a free position and

Table A.1. Torus Fit Parameters with 1σ Statistical Errors

Parameter	Value
Ψ (°)	163.6 ± 0.7
ζ (°)	$53.3^{+1.6}_{-1.4}$
r ($''$)	$3.3^{+0.08}_{-0.06}$
δ ($''$)	1.0 (fixed)
β	0.70 ± 0.01
Point Source (Counts)	2897^{+65}_{-52}
Torus (Counts)	1221^{+55}_{-41}
Jet (Counts)	185^{+8}_{-21}
Counter-jet (Counts)	325^{+43}_{-54}

amplitude shifts the best-fit position angle to $\Psi = 165° \pm 0.^{\circ}5$ and the inclination to $\zeta = 56.^{\circ}7 \pm 1.^{\circ}0$. We therefore infer systematic errors about $3\times$ larger than our rather small statistical errors.

We have also measured the outer jet/counter-jet system. Minimizing the residual to a 1-D line passing through the pulsar, the two jets together lie at $\Psi_{\rm outer} = 169.^{\circ}4 \pm 0.^{\circ}15$. If the jets are fitted separately, we obtain $\Psi_{\rm outer} = 168.^{\circ}4 \pm 0.^{\circ}2$ and $170.^{\circ}9 \pm 0.^{\circ}2$ for the outer jet and counter-jet, respectively. Thus the two jets are mis-aligned at the $\sim 8\sigma$ level. A fit to the count distribution about the best-fit axis shows that the narrow outer counter-jet has a Gaussian FWHM across the jet of $2.''3 \pm 0.''2$. The outer jet appears broader at the base with an initial width of $4.''9 \pm 0.''5$, continuing at FWHM=$2.''7 \pm 0.''3$ for its outer half. These estimates have been corrected for the telescope PSF, which is quite uniform this close to the aimpoint.

It is important to note that at the observation roll angle, the read-out direction lies at $\Psi = 168.^{\circ}7$. Due consideration, however, shows that the jet structure cannot be produced by the read-out trail. First the jets cover only $\sim 1'$; the read-out excess should cover the full I3 chip. Second the pulsar provides only ~ 2900 $1-7$ keV counts. The read-out trail (out-of-time) image of this source should contribute only 36 counts over the full $8.'3$ strip across I3 and ~ 2.5 counts in the 'jet regions'; the

outer jet and counter-jet have 92 and 93 $1-7$ keV counts, respectively. Finally the outer jets are much harder than the soft X-ray emission from the pulsar; indeed with a mean detected photon energy ~ 2 keV these are the hardest extended features in the image.

The over-all system, showing an asymmetric torus, broad inner jets and narrow outer jets is, of course, very similar to the Vela PWN as studied with *Chandra* by Pavlov et al. (2003). We will discuss the comparison with the Vela system in §A.3, highlighting the differences. We interpret these as suggesting that the PSR B1706−44 PWN has developed from a low velocity pulsar.

A.2.4 Spectral Analysis

For the best possible constraints on the source spectrum, we have reprocessed both the ~ 11 ks cleaned ACIS-S data set and our new ~ 100 ks ACIS-I data set with the new time-dependent gain adjustment and CTI correction available in CIAO 3.2. The updated RMFs should in particular improve the low energy calibration, important for obtaining the best estimates of $N_{\rm H}$. As noted above, in these data sets the pile-up was negligible at $\sim 3\%$. To model the aperture corrections, 10 PSFs with monochromatic energies from 0.5 to 9.5 keV were simulated using the Chandra Ray-Tracer program, ChaRT. The enclosed energy fraction as a function of radius was fitted to a linear function of energy and this was used to correct the ARFs used in the spectral fit. In extracting the pulsar spectrum, an aperture of radius $1''$ was used to minimize nebular contamination. Results from the combined fits of the ACIS-I and ACIS-S pulsar data sets are listed in Table 1; the spectral fits are substantially better for composite models with both thermal and power-law components. Spectral parameter errors are projected multi-dimensional 1σ values. We quote both absorbed and unabsorbed fluxes. As is often the case with low statistics X-ray spectra, projected (multi-dimensional) errors on the fluxes are very large due to spectral parameter uncertainties. Thus, we follow other authors in quoting flux errors as 1σ single parameter values.

To get the best constraints on the point source spectrum, Table A.2 gives fits

Table A.2. Spectral Fits to PSR B1706−44

		BLACKBODY/ATMOSPHERE				POWER LAW			
MODEL	$N_{\rm H}$ (10^{21} cm^{-2})	T_∞ (10^6 K)	R_∞ (km)	Abs. Flux $f_{0.5-8}$ (10^{-13} ergs cm^{-2} s^{-1})	Unabs. Flux $f_{0.5-8}$ (10^{-13} ergs cm^{-2} s^{-1})	Γ	Abs. Flux $f_{0.5-8}$ (10^{-13} ergs cm^{-2} s^{-1})	Unabs. Flux $f_{0.5-8}$ (10^{-13} ergs cm^{-2} s^{-1})	χ^2/dof
PL	3.8 ± 0.3	...	...	...	...	$3.06^{+0.15}_{-0.14}$	2.01 ± 0.04	4.74 ± 0.1	145.9/99
BB	1.0 ± 0.3	3.7 ± 0.2	$0.4^{+0.13}_{-0.11}$	1.42 ± 0.03	1.76 ± 0.04	...	...	...	288.4/99
PL+BB	$4.7^{+0.8}_{-0.7}$	$2.00^{+0.17}_{-0.16}$	$2.4^{+1.6}_{-1.0}$	0.83 ± 0.03	3.85 ± 0.12	1.62 ± 0.2	1.70 ± 0.07	2.25 ± 0.1	40.6/97
	5.0 (fixed)	1.93 ± 0.06	$2.8^{+0.76}_{-0.70}$	0.82 ± 0.03	4.40 ± 0.14	1.68 ± 0.17	1.70 ± 0.07	2.33 ± 0.1	40.8/98
PL+Atm	$5.9^{+0.9}_{-0.8}$	$0.79^{+0.13}_{-0.11}$	13.1 (fixed)	0.85 ± 0.03	6.8 ± 0.2	1.67 ± 0.2	1.67 ± 0.07	2.34 ± 0.1	40.7/97
	5.0 (fixed)	0.91 ± 0.05	13.1 (fixed)	0.88 ± 0.03	4.92 ± 0.15	1.56 ± 0.17	1.67 ± 0.07	2.2 ± 0.1	40.8/98

with $N_{\rm H}$ held to the value from the power law fits to the extended emission. We have also compared our results with the *XMM-Newton* fitting of McGowan et al. (2004), by fitting counts in the $20''$ aperture used in that observation. Our parameters and fluxes for the thermal component are generally in very good agreement. However, since this aperture contains much of the torus and central PWN, *XMM-Newton* substantially overestimates the non-thermal flux for the point source. Their fitted power-law flux corresponds to 7.5×10^{-13} ergs cm^{-2} s^{-1} ($0.5 - 8$ keV, unabsorbed). In the $20''$ aperture we find 9.6×10^{-13} ergs cm^{-2} s^{-1} ($0.5 - 8$ keV); while the small *Chandra* point source aperture gives 2.3×10^{-13} ergs cm^{-2} s^{-1} ($0.5 - 8$ keV) for the power law component. We find a similar $\sim 3\times$ excess in the power-law + atmosphere flux for the fit to the large *XMM-Newton* aperture. Conversion of the power law flux observed in our small point source aperture to the *XMM-Newton* band shows that the expected PN+MOS ($0.2 - 10$ keV) count rate is 18% of the total (power law + thermal) counts in the $20''$ aperture. In soft ($0.2 - 1.35$ keV) and hard ($1.35 - 10$ keV) bands the predicted fraction of the counts from the power law are 12% and 21%, respectively. However the light curves of McGowan et al. (2004) show that the pulse fractions are 21% (soft), 12% (hard) and 11% (total). Since the small aperture power law produces only 12% of the soft counts but 21% are pulsed, there must a thermal pulse component. Conversely, since the power law produces 21% of the hard band flux, but this only has a pulse fraction of 12%, some of the power law counts must be unpulsed. Extrapolation of the PWN count excess above the point source PSF in the sub-luminous zone at $2'' - 3''$ produces $\lesssim 1\%$ of the point source aperture counts. Thus the larger scale torus emission does not contribute significantly to the point source power law and cannot account for its unpulsed component. This suggests that part of the magnetospheric emission is nearly isotropic or that there is a very compact ($\lesssim 1''$) PWN component at the pulsar position.

For the thermal component, the fit flux gives an emitting area (effective radius) as a function of distance. Our fit to a pure blackbody gives $R_{eff} = 2.8 d_3$ km. Thus for reasonable distances, this flux represents hot $T \sim 2 \times 10^6$ K emission from a small fraction of the stellar surface ($\sim 4.5\%$ for an $R^\infty = 13.1$ km star). The light

Table A.3. Spectral fits to extended sources

Object	$N_{\rm H}$ (10^{21} cm^{-2})	Γ	Abs. Flux $f_{0.5-8}$ (10^{13} ergs cm^{-2} s^{-1})	Unabs. Flux $f_{0.5-8}$ (10^{13} ergs cm^{-2} s^{-1})	χ^2/dof
Nebula	$5.0 \pm 0.4^{\dagger}$	$1.77^{+0.09}_{-0.08}$	5.6 ± 0.23	7.9 ± 0.32	67.4/77
Equatorial PWN	$5.0 \pm 0.4^{\dagger}$	1.57 ± 0.08	2.4 ± 0.07	3.2 ± 0.09	70.3/81
Torus	$5.0 \pm 0.4^{\dagger}$	1.48 ± 0.08	1.5 ± 0.05	1.9 ± 0.07	39.8/53
Jet	5.0 (fixed)	$1.26^{+0.14}_{-0.13}$	0.42 ± 0.03	0.52 ± 0.04	12.0/18
Counter Jet	5.0 (fixed)	1.39 ± 0.10	0.81 ± 0.04	1.0 ± 0.05	10.8/18
Outer Jets	5.0 (fixed)	1.26 ± 0.18	0.27 ± 0.03	0.33 ± 0.03	11.9/18

† – Simultaneous $N_{\rm H}$ fit.

element neutron star atmosphere models, such as the pure H 10^{12} G model grid used here (Zavlin et al. 1996), have large Wien excesses. When fit they give lower T_{eff}. Also, the blackbody departures allow one, in principle, to fit both the surface redshift and radius. In practice, these are typically highly degenerate in CCD-quality data. We assume here a generic surface radius of $R_s = 10$ km, corresponding to $R_\infty = R_s(1-2GM/R_sc^2)^{-1/2} = 13.1$ km. With $N_{\rm H}$ free (giving $5.9\pm0.9\times10^{21}$cm^{-2}) our thermal flux normalization gives a radiating radius of $R_\infty = 27.4d_3$ km, which is difficult to reconcile with expected neutron star radii for any $d > 1.8$ kpc. However, when $N_{\rm H}$ is fixed at the nebular value of 5×10^{21} cm^{-2}, we get an effective radius of $R_\infty = 16.1d_3$ km, which is tolerable even at our nominal 3 kpc distance.

Analysis of the low signal-to-noise, extended flux depends critically on the background subtraction. Given the limited statistics, only simple absorbed power-law fits were attempted for all non-thermal sources. The results are listed in Table A.2. For consistency, all fits are to the $0.5 - 8$ keV range and we quote both absorbed and unabsorbed fluxes.

Note that there is significant softening of the extended emission as one progresses to larger scales and that the jet components appear to be the hardest of all. This is certainly consistent with the idea that the central pulsar supplies fresh energetic electrons and that synchrotron burn-off increasingly softens the spectrum as older

populations are viewed in the outer PWN. Again this trend is common in the well-measured young PWNe. Allowing the photon index to vary for the different nebula components, the best-fit to a global absorption value for the extended emission gives us our fiducial $N_{\rm H} = 5 \times 10^{21}$ cm^{-2}. This is consistent with free-fit values for the point source, but given complexities of the composite thermal+power law model, we consider the nebular fit value more robust. Note that with DM= 75.7 cm^{-3} pc, the $n_{\rm H}/n_e \approx 21$ for this sight-line is large, but not unprecedented for low $|b|$ pulsars. This is also consistent with the H$_{\rm I}$ absorption measurements and a fiducial SNR distance ~ 3 kpc, given the appreciable uncertainties.

A.3 Interpretation and Conclusions

A number of authors have discussed the evolution of a PWN within an expanding supernova remnant. For example, van der Swaluw et al. (2001) and Chevalier (2005) describe the early evolution when the supernova ejecta are in free expansion. Later, after the remnant interior is heated by the passage of the reverse shock, the PWN evolves within the Sedov phase supernova remnant whose radius is $R_{\rm SNR} = 1.17(E_0/\rho)^{1/5}t^{2/5}$ for an explosion energy E_0 in a $\gamma = 5/3$ medium of density ρ. PSR B1706−44 has a characteristic age $10^4\tau_4$ yr with $\tau_4 \approx 1.7$, so G343.1−2.3 should be safely in the Sedov phase with an expected angular size

$$\theta_{\rm SNR} \approx 16'(E_{51}/n_0)^{1/5}t_4^{2/5}/d_3 \tag{A.1}$$

for a supernova releasing energy $E_0 = 10^{51}E_{51}$ ergs in an external medium density n_0 cm^{-3}, at a true age 10^4t_4 yr at a distance $3d_3$ kpc. The observed size then implies $E_{51} \approx 11n_0t_4^{-2}d_3^5$, requiring a fairly energetic explosion for $d > 2$ kpc. During the Sedov phase the interior pressure is

$$P_{SNR} \approx 10^{-9}E_{51}^{2/5}n_0^{3/5}t_4^{-6/5}\ {\rm g\ cm^{-1}\ s^{-2}} \tag{A.2}$$

and is relatively constant away from the SNR limb.

The pulsar blows a wind bubble within this SNR interior, whose radius is

$R_{\rm PWN} \approx (E_*/E_0)^{1/3} R_{\rm SNR}$ for a PWN bubble energy $E_* = f\dot{E}\tau_c$ (van der Swaluw & Wu 2001). Although the accuracy of this dependence of PWN radius on pulsar injection energy has been questioned (Blondin, Chevalier, & Frierson 2001), we adopt it for the following estimates. With the observed ratio of radii, $R_{\rm PWN}/R_{\rm SNR} = 1.8'/25'$, we obtain $E_* = 3.7 \times 10^{-4} E_0$, i.e. this PWN has quite low internal energy. This is also reflected in the low radio and X-ray fluxes. Together we use these estimates, the observed size of the SNR, Equation (A.1) and the measured $\dot{E}_{36} = 3.4$ and $\tau_c = 1.75 \times 10^4$ yr to write $f \approx (R_{\rm PWN}/R_{\rm SNR})^3 E_0/(\dot{E}\tau_c) = 2.1\, n_0 t_4^{-2} d_3^5$. Now, if the PWN is adiabatic and we assume spindown with constant B and braking index $n = 3$ from an initial period P_0, we find that the total energy in the plerion is $[(P/P_0)^2 - 1]\dot{E}\tau_c$. Then, setting $f = (P/P_0)^2 - 1$ and eliminating the true age t using $t = \tau_c[1 - (P_0/P)^2]$ for magnetic dipole spindown, we obtain a constraint on the initial spin period

$$[1 - (P_0/P)^2]^3/(P_0/P)^2 = 0.68\, n_0 d_3^5 \tag{A.3}$$

which has a solution of $P_0 = 0.61P = 62$ ms for $d = 3$ kpc, and $P_0 = 0.79P = 80$ ms for $d = 2$ kpc. The corresponding true ages are $0.61\tau_c$ (1.1×10^4 yr) and $0.38\tau_c$ (0.67×10^4 yr), respectively. These numerical values are for $n_0 = 1$ and the density dependence from Equation (A.3) is quite weak. van der Swaluw & Wu (2001) present a similar sum for P_0, assuming a known E_0; the above formulation emphasizes the sensitivity to the poorly known d. Note that with the large implied initial period, the integrated PWN energy is quite comparable to the present spin energy, with $f \approx 1.7$ at $d = 3$ kpc and $f \approx 0.62$ at $d = 3$ kpc. So the spindown luminosity is roughly constant in the adiabatic phase and the PWN growth is closer to $t^{11/15}$ than to the $t^{3/10}$ law appropriate for impulsive energy injection (van der Swaluw et al. 2001).

Inside this wind bubble, the Sedov interior pressure confines the PWN, giving rise to a termination shock at

$$\theta_{\rm WS} \approx (\dot{E}/4\pi c P_{\rm SNR})^{1/2}/d. \tag{A.4}$$

which results in $\theta_{\rm WS} \approx 1\farcs2 \dot{E}_{36}^{1/2} E_{51}^{-1/5} n_0^{-3/10} t_4^{3/5} d_3^{-1}$. If we apply the SNR estimate for E_0 above, this becomes $\theta_{\rm WS} \approx 0\farcs72 \dot{E}_{36}^{1/2} n_0^{-1/2} t_4 d_3^{-2}$. Then, using $\dot{E}_{36} \approx 4$ and applying the age estimate following Equation (A.3) we get $\theta_{\rm WS} \approx 1\farcs5 n_0^{-1/2}$ ($d = 3$ kpc) or $\theta_{\rm WS} \approx 2\farcs1 n_0^{-1/2}$ ($d = 2$ kpc). These estimates are reasonably consistent with the observed 3″ torus radius, especially since an equatorially concentrated flow should have a stand-off distance 1.5-2× this spherical scale. The polar jets can have an initial shock at somewhat larger angle, with the resulting pitch angle scattering illuminating the jets somewhat further from the pulsar.

Of course, this bubble is offset from the center of G343.1−2.3 at $R = 0.5\, R_{\rm SNR}$ (Fig. A.1). This is inside the $\sim 0.68\, R_{\rm SNR}$ where van der Swaluw, Downes & Keegan (2004) note that the increasing density causes the pulsar to be supersonic, so a bow shock should not have yet formed. These authors however compute numerical models of a fast moving pulsar in a SNR interior. As the pulsar moves, the PWN should become highly asymmetric with a 'relic PWN' at the SNR center and the pulsar placed near the leading edge of the PWN; see van der Swaluw, Downes & Keegan (2004) Figures 7 and 8. We see no PWN structure near the geometric center of G343.1−2.3 and, if the 'bubble nebula' is identified with the shocked pulsar wind, the pulsar is certainly not offset from its center along the proper motion axis (away from the SNR center). So these models are an inadequate description of G343.1−2.3. From Figure A.2, the pulsar is well centered in the bubble nebula, with any offset from its center along the axis to the SNR substantially less than $30\Delta_{30}$″. Thus

$$v < 40\Delta_{30} d_3 / t_4 \text{ km s}^{-1} \ , \tag{A.5}$$

and the pulsar cannot have moved far from the explosion center. This is, of course, consistent with the scintillation results.

We can reconcile the symmetric PWN with the offset SNR shell if we assume that the pulsar progenitor exploded toward the edge of a quasi-spherical cavity. One scenario (also posited by Bock & Gvaramadze 2002; Gvaramadze 2002) that can associate the low velocity pulsar with G343.1−2.3 is to assume that the progenitor star had a stellar wind of mass loss rate $\dot{M}_{-8} 10^{-8} M_\odot$ yr^{-1} and wind speed $10^8 v_{\rm w8}$ cm s^{-1}

over $t \sim t_7 10^7$ yr, typical of the $\sim 10 M_\odot$ stars that dominate the pulsar progenitors (Maeder 1981). This evacuates a stellar wind bubble of size

$$\theta_{\rm SW} = 46' \left(\dot{M}_{-8} v_{\rm w8}^2 / n_0 \right)^{1/5} t_7^{3/5} / d_3. \tag{A.6}$$

During the main sequence lifetime, the star moving at $10 v_6$ km s^{-1} travels $\sim 2^\circ v_6 t_7 / d_3$ and so it can easily traverse its wind bubble. Thus, one can imagine an off-center supernova in a nearly symmetric stellar wind bubble of radius $\sim 25'$: the supernova blast wave expands to fill the bubble, passing to the Sedov phase near its present radius. The supernova produces a neutron star with little or no kick, placing the pulsar near its present position. This has the added advantage of accommodating the rather large SNR size with a more modest energy of a few$\times 10^{51}$ ergs. The PWN energy and size estimates above would then be somewhat amended; this would require a careful numerical simulation.

For the reasons detailed in the introduction, it is not yet clear that PSR B1706−44 and G343.1−2.3 are associated. So for completeness we can consider the case when the shocked pulsar wind blows an adiabatic bubble in a static, low $P_{\rm ext}$ external medium (Castor, McCray, & Weaver 1975). If we assume that the pulsar was born (sans SNR) or entered a confining region of the ISM $\sim 10^4$ yr ago and that since then it has been spinning down at the present energy loss rate, we find that it will blow a bubble of angular size

$$\theta_{\rm BN} \approx 0.76 (\dot{E} t^3 / \rho)^{1/5} / d \approx 120'' (\dot{E}_{36} / n_0)^{1/5} \tau_4^{3/5} / d_3. \tag{A.7}$$

These estimates change somewhat for a pulsar born at $P_0 \ll P$; since we are not making the association with the SNR G343.1−2.3, we can make no estimate of the initial spin period. As first noted by Dodson & Golap (2002), the $\sim 4'$ wide radio spur across the face of G343.1−2.3 has the approximate scale of such a 'bubble nebula'. If the PWN stays unmixed (relativistic) then the interior of the bubble will have a pressure $P_{\rm BN} \approx \dot{E} t / (4\pi R^3) \approx 1.6 \times 10^{-10} \left(n_0^3 \dot{E}_{36}^2 / \tau_4^4 \right)^{1/5}$ ergs cm^{-2} s^{-1}. In

turn, the torus termination shock in this medium is at

$$\theta_{\rm WS} \approx 2\farcs9 (\dot{E}_{36}/n_0)^{3/10} \tau_4^{2/5}/d_3. \tag{A.8}$$

If (e.g. through Rayleigh-Taylor instabilities) the pulsar wind is well mixed with the swept up gas, the adiabatic thermal pressure would be $\sim 2\times$ larger. Interestingly, the angular scales for this scenario are also reasonably compatible with the observed torus and bubble nebula size. Of course this scenario leaves open the question of the pulsar origin. Again the pulsar would need to have a quite low velocity to produced the observed symmetry.

Turning to the spectral results, we note that Possenti et al. (2002) fit a correlation between spindown energy and the PSR+PWN luminosity: $L(2-10\ {\rm keV}) = 1.8 \times 10^{38} \dot{E}_{40}^{1.34}$ ergs s^{-1}. For the PSR B1706−44 parameters this predicts a flux $f(2-10\ {\rm keV}) = 4.7 \times 10^{-12} d_3^{-2}$ ergs cm^{-2} s^{-1}. The observed $2-10$ keV flux is in fact $\sim 1.7 \times 10^{-12}$ ergs cm^{-2} s^{-1}, even including the outer 'bubble nebula'; without this component it is half as large. These correlations are not very accurate, but this does imply that the PSR B1706−44 PWN is substantially under-luminous for any distance less than 3 kpc. Gotthelf (2003) has derived correlations between the pulsar spindown power and the pulsar/PWN spectral indices. His relation predicts $\Gamma_{\rm PSR} = 0.63 \pm 0.17$ (substantially smaller than our power law index $\sim 1.6 \pm 0.2$) and $\Gamma_{\rm PWN} = 1.3 \pm 0.3$ (not inconsistent with the values measured for the torus and equatorial PWN).

As described in §A.2.4, the spectrum softens appreciably from the central torus to the outer bubble nebula. This suggests increased aging of the synchrotron population. Figures A.2 and A.3 show that the bulk of the radio emission lies in the 'bubble nebula' region. So we can take the radio flux and spectral index from Giacani et al. (2001) and compare with our nebula X-ray flux (Fig. A.4). Comparing the radio spectral index $\alpha_R = 0.3$ with the best-fit X-ray index $\alpha_X = 0.77$, shows a break quite close to the $\Delta\alpha = 0.5$ expected from synchrotron cooling. The extrapolated intersection of these power laws gives a break frequency of ${\rm Log}[\nu_B\ ({\rm Hz})] = 12.2^{+0.9}_{-1.1}$. For the fiducial pulsar age of $\sim 1.7 \times 10^4$ yr, this corresponds to a nebula field of

$1.4^{+2.1}_{-0.6} \times 10^{-4}$ G. Note that the magnetic pressure from this (photon flux-weighted) average field is $\sim 8 \times 10^{-10}$ g cm^{-1} s^{-2}, somewhat larger than the nebula pressure estimated from its radius. This may indicate field compression in the nebula limb. In general, if the mean nebula field is $10^{-4}B_{-4}$ G for a nebula of angular radius $\sim 100''\theta_{100}$, the total nebula field energy is $E_B \approx 1.5 \times 10^{47} B^2_{-4}(\theta_{100} d_3)^3$ ergs. This is comfortably less than the present spin energy $E_{\rm PSR} \approx 2 \times 10^{48}$ ergs, so the nebula can be easily powered even if the pulsar was born close to its present spin period. We find that this cooling break field is substantially larger than the equipartition field of $10 - 15$ μG inferred for the radio and X-ray emitting populations (also the minimum equipartition nebula energy $\sim 9 \times 10^{45}$ ergs is substantially smaller). The cooling break field can also be compared to that expected from simple radial evolution of the pulsar surface field: if this field $B_* = 3 \times 10^{12}$ G falls off as r^{-3} to the light cylinder, then as $1/r$ to the wind shock where it is compressed we get $B_{\rm WS} \sim 3B_* r_*^3/(r_{\rm LC}^2 r_{\rm WS}) \sim 1$ mG. If it continues to fall off as $1/r$ beyond this we get a field at the limb of the bubble nebula of $\sim 30\mu$ G. So the best we can do is to infer a mean nebular field $\sim 10 - 30\times$ the equipartition value, with some generation of new field beyond the torus wind shock. The energetic requirements for this field, required to match the ν_B cooling break, are comfortably less than the energy available from PSR B1706−44. These field estimates are consistent with the non-detection of TeV ICS flux from this source (Aharonian et al. 2005).

The narrow outer jets also have a power-law spectrum and are almost certainly synchrotron-emitting. For a reasonable $0.1\,B_{-4}$ mG field, the observed X-rays of $E_\gamma = 1.5 B_{-4} \Gamma^2_{7.5}$ keV require substantial $e^- e^+$ energies, with $\Gamma_e = 3 \times 10^7 \Gamma_{7.5}$ near the radiation-reaction limited primary Lorentz factor inferred for many polar cap (Muslimov & Harding 2003) and outer magnetosphere (Romani 1996) pulsar models. Since the jet is narrow, confinement of these pairs imposes a (not very restrictive) lower bound on the jet field $B_{-4} > 0.075 E_5^{1/3}/(d_3 \theta_w)$ where the maximum observed jet photon has $E \sim 5E_5$ keV and the observed outer jet half-width is $\theta_w{}''$. A more restrictive upper limit on the mean jet field comes from the observation that the jets do not soften noticeably before their end $\sim 30\theta_{30}{}''$ from the pulsar. If we assume a jet bulk speed βc, then arguing that the flow time is shorter than the synchrotron

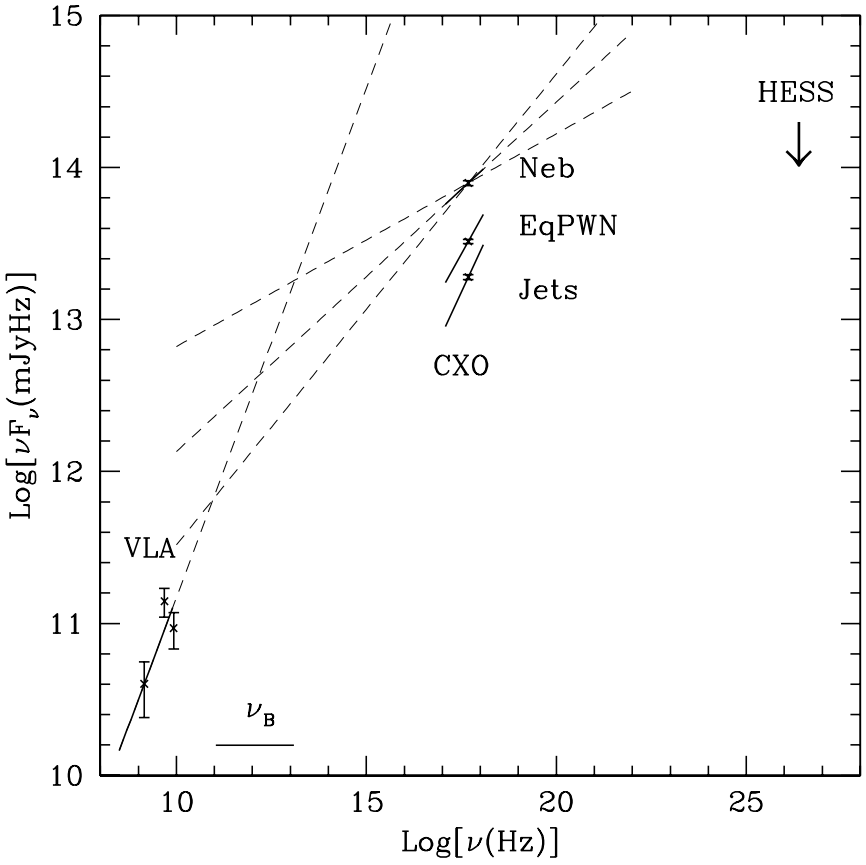

Figure A.4 Outer PWN ('bubble nebula') spectral energy distribution (SED). Radio data are from Giacani et al. (2001), the TeV upper limit is from Aharonian et al. (2005). The spectra of the inner, younger PWN components are plotted for comparison. The extension of the radio PL and the best-fit nebula (outer PWN) PL meet at $\nu_B \sim 1.6 \times 10^{12}$ Hz; the indices are consistent with a $\Delta\alpha = 0.5$ cooling break.

cooling time gives us the limit $B_{-4} < 8.5 \left(\frac{\beta}{d_3\theta_{30}}\right)^{2/3} E_5^{-1/3}$.

When the observed jet spectrum has an energy index of $\alpha = \Gamma - 1 \approx 0.3$, we infer a power-law spectrum of $e^{\pm}$ in the jet $N(\Gamma_e)d\Gamma_e = K\Gamma_e^{-p}d\Gamma_e$, with $p = 2\alpha + 1 \approx 1.6$. We can then make an estimate of the minimum jet luminosity, i.e. at 'equipartition' when $B^2 = 6\pi m_e c^2 \int \Gamma_e N(\Gamma_e)d\Gamma_e$. Given the observed combined outer jet luminosity $(0.5 - 8$ keV$)$ $L = 4\pi d^2 f_{\rm oj} \approx 2.7 \times 10^{31}$ ergs s^{-1} and emitting

volume $V \approx 2 \times \theta_L \times \pi\theta_w d^3 \approx 1.1 \times 10^{52}(\theta_L/20)\theta_w^2 d_3^3$ cm^3 with the angles in arcsec, we can estimate the equipartition field for an isotropic plasma as

$$B_{\rm eq} = \left[\frac{18\pi}{\sigma_T}\left(\frac{2\pi m_e c}{E_{\rm max}}\right)^{1/2}\frac{2(1-\alpha)}{1-2\alpha}\frac{1-(E_{\rm min}/E_{\rm max})^{(1-2\alpha)/2}}{1-(E_{\rm min}/E_{\rm max})^{(1-\alpha)}}\frac{L}{V}\right]^{2/7} \tag{A.9}$$

where the observed photon spectrum runs from $E_{\rm min}$ to $E_{\rm max}$. For the observed flux this gives

$$B_{\rm eq} \approx 0.25 \times 10^{-4} q(\alpha)[\theta_L \theta_w^2 d_3/20]^{-2/7}\ {\rm G}\ , \tag{A.10}$$

where $q(\alpha = 0.3) = 1$ is a weak function of α. The corresponding minimum energy flux for the outer jet is

$$L_{\rm oj} = 8 \times 10^{33}\beta d_3^{12/7}\theta_w^{10/7}(\theta_L/20)^{-2/7}\ {\rm ergs\ s^{-1}}\ , \tag{A.11}$$

where the jet bulk velocity is βc. This is $\sim 10^{-3}\dot{E}$ per jet and will, of course, be larger if the jet flow includes ions. Interestingly, if the pulsar couples roughly isotropically to the PWN, then the corresponding fraction of the outflow should subtend a half angle of $\sim 5^\circ$. This is somewhat smaller than the angle subtended by the inner jets, but $\sim 3\times$ larger than the $\sim 1''$ width of the ends of the jet – there is substantial collimation of the jet energy flux.

We have argued that a low pulsar velocity can explain the symmetry of the PWN. The central location of the pulsar and spherical post-shock flow may also allow the equatorial toroidal structure and polar jets to propagate undisturbed to large radii. We do, however, measure a small misalignment of the outer jets, corresponding to a deflection of $\theta_{\rm de} = 1\overset{\circ}{.}3 \pm 0\overset{\circ}{.}15$ for each. If we imagine a pressure acting along the jet's $\sim 30''$ length, then the required perturbation is $\delta P \approx L_{\rm oj}\tan\theta_{\rm de}/(\beta c A_{\rm oj}) \approx 5 \times 10^{-14} L_{34}/(\beta\theta_{30}\theta_w d_3^2)$ g cm s^{-2}, where $A_{\rm oj}$ is the jet's cross sectional area. This is only $\sim 10^{-3}$ of the total pressure in the nebula. It could be due to ram pressure if the shocked nebular medium flows to the west at $v \sim 1.7 n_{\rm neb}^{-1/2}$ km s^{-1}.

Our X-ray measurements have established the PWN symmetry axis, presumably reflecting the pulsar spin axis, to very high precision. Unfortunately our original

goal of relating this to the proper motion axis remains unfulfilled. It is true that the torus symmetry axis points roughly toward the center of G343.1−2.3, confirming the estimates from earlier *Chandra* data. However, the PWN symmetry about the pulsar and the low scintillation velocity suggest a very low transverse speed ≤ 40 km s^{-1}, which would preclude a birth site as distant as the SNR center. This low speed makes a direct proper motion challenging, but allows latitudinal asymmetries in the PWN flow to propagate undisturbed to fairly large radius, where they can be imaged with *Chandra*. Thus, study of this PWN offers some good opportunities to probe outflow dynamics and jet collimation. Study of this, and similar, PWNe may prove useful electrodynamic analogs of the $10^6\times$ more powerful AGN jets. A viable scenario for maintaining the G343.1−2.3/PSR B1706−44 association posits a supernova event near the present pulsar site, with the remnant inflating a pre-existing off-center cavity. However, the residual (small) proper motion could then have any direction. In fact, the faint extension of the PWN (bubble nebula) to the west and the increased radio surface brightness to the east might suggest a rather slow pulsar motion at PA $\sim 80°$. This would be nearly orthogonal to the torus symmetry axis. With the large P_0 estimated here, this could be construed as suggesting poor rotational averaging of a birth kick (Ng & Romani 2004). So the PWN/SNR geometry offers both aligned and orthogonal axes. Only a sensitive astrometric campaign can detect or limit the pulsar motion and resolve this ambiguity.

Appendix B

The Origin and Motion of PSR J0538+2817 in S147

This chapter is based on "The Origin and Motion of PSR J0538+2817 in S147", C.-Y. Ng, Roger W. Romani, Walter F. Brisken, Shami Chatterjee & Michael Kramer 2007, ApJ, in press.

B.1 Introduction

S147 (G180.0−1.7) is an optically faint shell-type supernova remnant (SNR) located in the direction of the Galactic anti-center. It is highly filamentary and has a radius of 83′ (Sofue, Fürst,& Hirth 1980). Although age estimates vary widely, from 20 kyr (Sofue et al. 1980) to 100 kyr (Kundu et al. 1980), S147 is believed to be one of the oldest SNRs with well-defined shell structure. It has been extensively studied at several wavelengths including radio (Kundu et al. 1980; Sofue et al. 1980), optical (Lozinskaya 1976; Kirshner & Arnold 1979), UV (Phillips, Gondhalekar, & Blades 1981) and X-ray (Souvageot et al. 1990). A recent continuum-subtracted Hα image (Drew et al. 2005) reveals much detailed structure in S147. As shown in Figure B.1[1],

[1]The Hα image of S147 is based on data obtained as part of the INT Photometric Hα Survey of the Northern Galactic Plane: prepared by Albert Zijlstra, University of Manchester and Jonathan Irwin, IoA Cambridge.

the shell is mostly circular with a few obvious blowouts to the East and the North. Gvaramadze (2006) suggested that a faint blowout to the West and the brighter lobe to the East define a bilateral axis passing through the center. Most of the bright filaments concentrate on the southern half, where the SNR boundary is also sharper. In contrast, the northern half is more diffuse and less well-defined.

Within the boundaries of S147, a 143 ms pulsar PSR J0538+2817 was discovered by Anderson et al. (1996) in an undirected pulsar survey using the 305 m Arecibo radio telescope. The pulsar has a large characteristic age $\tau_c = P/2\dot{P} = 620$ kyr and a dispersion measure (DM)-estimated distance of 1.2 kpc. Based on the positions and distances of PSR J0538+2817 and S147, Anderson et al. (1996) suggested an association between the two. From the maximum SNR age of 10^5 yr, Romani & Ng (2003) argued that PSR J0538+2817 had a slow initial spin period. This was supported by Kramer et al. (2003) who obtained a rough timing proper motion which indicated that the pulsar is moving from near the SNR geometrical center with a kinematic age of only 30 kyr, much shorter than the characteristic age. To reconcile the discrepancy, they also suggested a large initial spin period of 139 ms for the pulsar. Alternatively, Gvaramadze (2006) proposed that PSR J0538+2817 arose in the first supernova from a massive binary, while a second supernova produced S147. In X-rays, PSR J0538+2817 has been detected by *ROSAT* All Sky Survey (Sun et al. 1996) and HRI imaging. A 20 ks *Chandra* ACIS-S observation discovered extended emission around the pulsar (Romani & Ng 2003), while an XMM-Newton observation (McGowan et al. 2003) reported the detection of pulsed X-ray emission.

In summary, S147 with an old nearly circular shell and a central pulsar showing extended X-ray emission, provides some unique opportunities to test the details of the pulsar/SNR connection. Kinematic measurements, along with X-ray morphology and cooling measurements can probe the history of the pulsar.

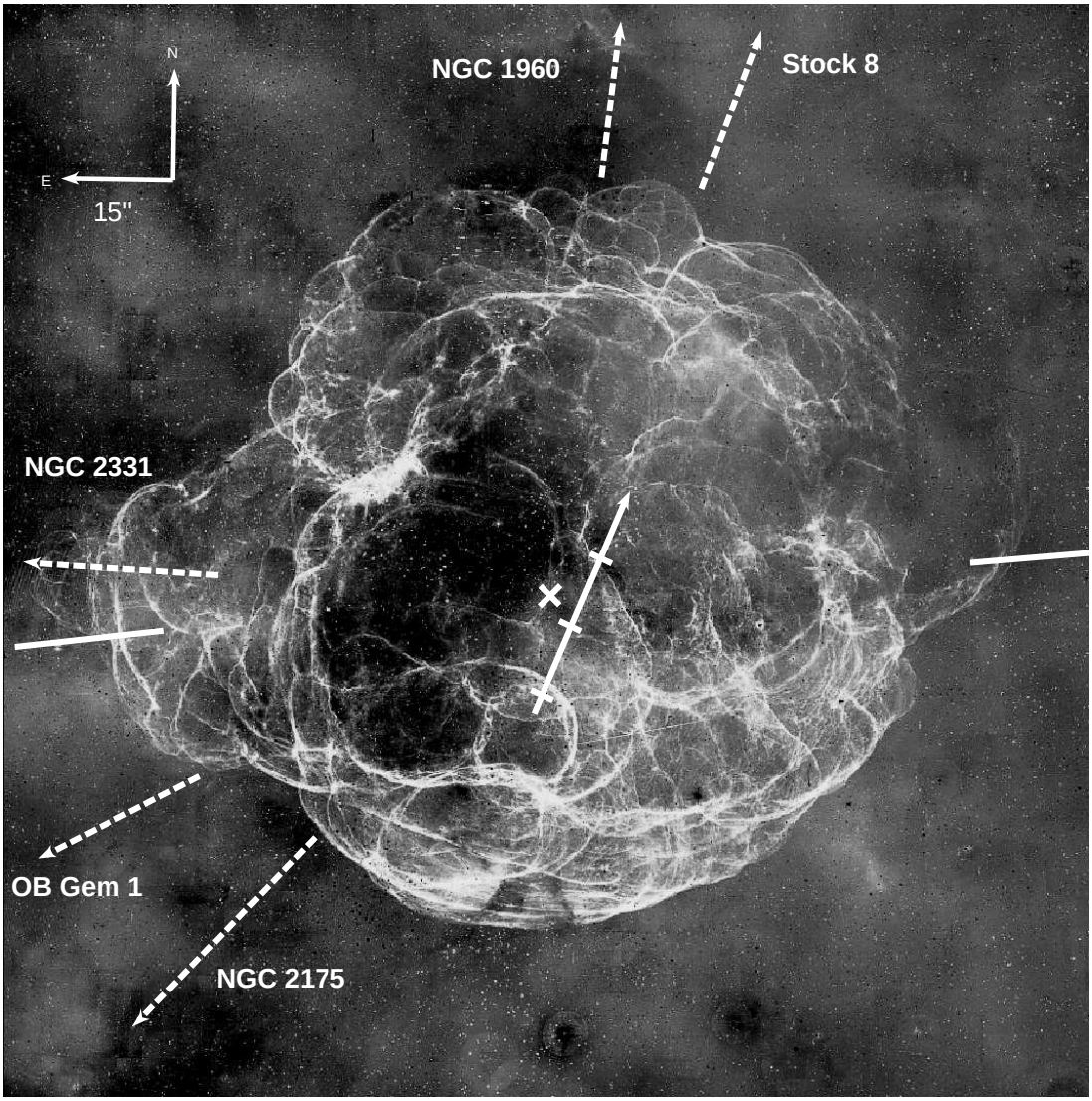

Figure B.1 Continuum-subtracted Hα image of S147 (Drew et al. 2005). The arrow shows the pulsar's proper motion direction and points to its current position (see § B.2), with tick marks indicating the birth-sites of the pulsar if born 20, 40 & 60 kyr ago. The cross marks the SNR geometrical center suggested by Kramer et al. (2003). Solid lines mark a possible bilateral axis (Gvaramadze 2006) and dashed lines show the direction to several candidate birth-sites for the progenitor star.

B.2 Parallax and Proper Motion Measurement

PSR J0538+2817 was observed with the NRAO VLBA over 9 epochs between 2002 and 2006. The observations were conducted between 1.4 and 1.7 GHz, as a trade-off between increasing pulsar flux at lower frequencies and improved resolution as well as reduced ionospheric effects at higher frequencies. At each epoch, 4 spectral windows (IFs) each with 8 MHz bandwidth are observed simultaneously. To retain visibility phase coherence, repeated visits were made to the primary phase calibrator source 133′ distant from the pulsar. A VLA survey of the region around J0538+2817 revealed a compact 8 mJy source only 8′ distance from the pulsar; the two sources are within the same VLBA primary beam and were observed simultaneously. The data were correlated in two passes, first centered on the pulsar field, and then a second pass centered on the in-beam calibrator. The signal-to-noise ratio for the pulsar was boosted by 'gating' (accepting signal from) the correlator on at the expected times of arrival of pulses, using current pulse timing solutions obtained for each epoch from ongoing observations at the Jodrell Bank Observatory. Incremental phase calibration derived from observations of the in-beam source were applied to the pulsar for considerably improved calibration.

Data analysis was performed using the AIPS package with a customized pipeline (Brisken 2007, in preparation), which included amplitude calibration based on the system temperatures and antenna gains, followed by visibility phase calibration based on the primary calibrator and the in-beam source. Large scale ionospheric phase effects were estimated and corrected with the AIPS task TECOR, using global models of the ionospheric electron content based on distributed GPS measurements. Once the calibration was completed, the pulsar position was measured by fitting a Gaussian ellipse to calibrated images made separately for each IF. The pulsar parallax and proper motion were then obtained from a linear least-squares fit to the epoch positions.

Table B.1 shows the best-fit astrometric results from 8 good epochs, for which the pulsar is far away from the sun, with IFs equally weighted. The derived pulsar distance and transverse velocity are $d = 1.47^{+0.42}_{-0.27}$ kpc and $V_\perp = 400^{+114}_{-73}$ km s^{-1}

Table B.1. Parameters for PSR J0538+2817

Parameter	Value
Epoch (MJD)	53258
R.A. (J2000)	$05^{\rm h}38^{\rm m}25\overset{\rm s}{.}05237 \pm 0\overset{\rm s}{.}00001$
Decl. (J2000)	$+28^\circ17'09\overset{''}{.}3030 \pm 0\overset{''}{.}0001$
$\mu_{\alpha\cos\delta}$ (mas yr^{-1})	-23.53 ± 0.16
μ_δ (mas yr^{-1})	52.59 ± 0.13
π (mas)	0.68 ± 0.15
d (kpc)	$1.47^{+0.42}_{-0.27}$
$V_\perp$ (km s^{-1})	400^{+114}_{-73}
l, b	$179\overset{\circ}{.}7186$, $-1\overset{\circ}{.}6859$
μ_l, μ_b (mas yr^{-1})	-57.03, 8.18
n_e (cm^{-3})	0.027 ± 0.006

respectively. The distance is in good agreement with the DM-estimate value $d_{DM} = 1.2 \pm 0.2$ kpc, using the NE2001 model (Cordes & Lazio 2002). The proper motion is also consistent with the timing observation results reported by Kramer et al. (2003), but our errors are much smaller, especially in the ecliptic latitude (μ_β).

To convert the proper motion to its local standard of rest (LSR), we correct for differential Galactic rotation using $\Omega_0 = 220$ km s^{-1}, $R_0 = 8.5$ kpc (Fich, Blitz, & Stark 1989) and the solar constants 10 ± 0.36, 5.25 ± 0.62, 7.17 ± 0.38 km s^{-1} (Dehnen & Binney 1998). The corrected proper motion is $\mu_* = 58.51 \pm 0.18$ mas yr^{-1} at position angle (PA) $336\overset{\circ}{.}8 \pm 0\overset{\circ}{.}13$, which converts to a transverse velocity of $V_\perp = 407^{+116}_{-74}$ km s^{-1}. Backward extrapolation of the pulsar's motion indicates that it passed $\sim 8'$ from the geometrical center of S147 defined by Kramer et al. (2003) at $\alpha = 05^{\rm h}40^{\rm m}01^{\rm s} \pm 2^{\rm s}$, $\delta = 27^\circ48'09'' \pm 20''$ (J2000). Since the pulsar is young and located near the Galactic plane, this trajectory is not significantly altered by acceleration in the Galactic potential. For any reasonable Galactic model (e.g. in Sun & Han 2004, and references therein), the displacement from a linear trajectory over the pulsar characteristic age is much smaller than $1'$. However, the SNR and pulsar are almost certainly associated (see below) and thus we conclude that the

nominal center of the shell does not represent the explosion site and that S147 underwent asymmetric expansion, likely due to inhomogeneities in the surrounding ISM.

B.3 *CXO* Observations

Chandra observations of PSR J0538+2817 were carried out on 2006 Jan 18 & 20 (Observation IDs 6242 & 5538) with the ACIS-I array operating in very faint timed exposure (VF TE) imaging mode. The pulsar was positioned near the aim point on the I3 chip, which was the only chip active during the observation. Subarray mode with 160 rows was used to further reduce the CCD pile-up. The resulting frame time of 0.5 s reduced the pile-up of the pulsar to 2%, ensuring the distortion of the point-spread function (PSF) and the high energy spectrum is minimal. The total live time was 93.2 ks and examination of the background light curve showed no strong flares during the observation. Hence, all data is included in the analysis.

For comparison, we have also reprocessed the archival 20 ks ACIS-S exposure (ObsID 2796) observed on 2002 Feb 7. After filtering out the periods suffering from background flares, 18.5 ks of clean exposure remains. All data analysis was performed using CIAO 3.3 and CALDB 3.2.1 to ensure the latest time-dependent gain calibration and charge transfer inefficiency (CTI) correction are applied. To further improve the spatial resolution, we removed the ACIS pixel randomization and applied the algorithm by Mori et al. (2001) to correct the position of split pixel events.

B.4 Spatial Analysis

The ACIS-I $0.5 - 8$ keV image is shown in Figure B.2. The point source produces 0.12 cts s^{-1}. With the short frame time, a trail of counts can be seen along the read-out direction (at PA 5°), with 0.5 cts $pixel^{-1}$. The extended emission $\sim 5''$ NE of the pulsar reported by Romani & Ng (2003) is clearly detected in the new observation. However, the deeper exposure shows that the structure is not an obvious torus. It

also appears somewhat fainter in the new data, with $(4.3 \pm 0.7) \times 10^{-4}$ cts s^{-1} in 0.5-8 keV after background subtraction, as compared to $(9.7 \pm 2.2) \times 10^{-4}$ cts s^{-1} in the archival ACIS-S data. Diffuse emission is also seen in the SE direction, as noted by Romani & Ng (2003), at $\sim 3''$ from the point source. Given that the direction is behind the pulsar's proper motion, this could be trailed emission from relativistic electrons in the motion-confined pulsar wind, as observed in other PWN systems.

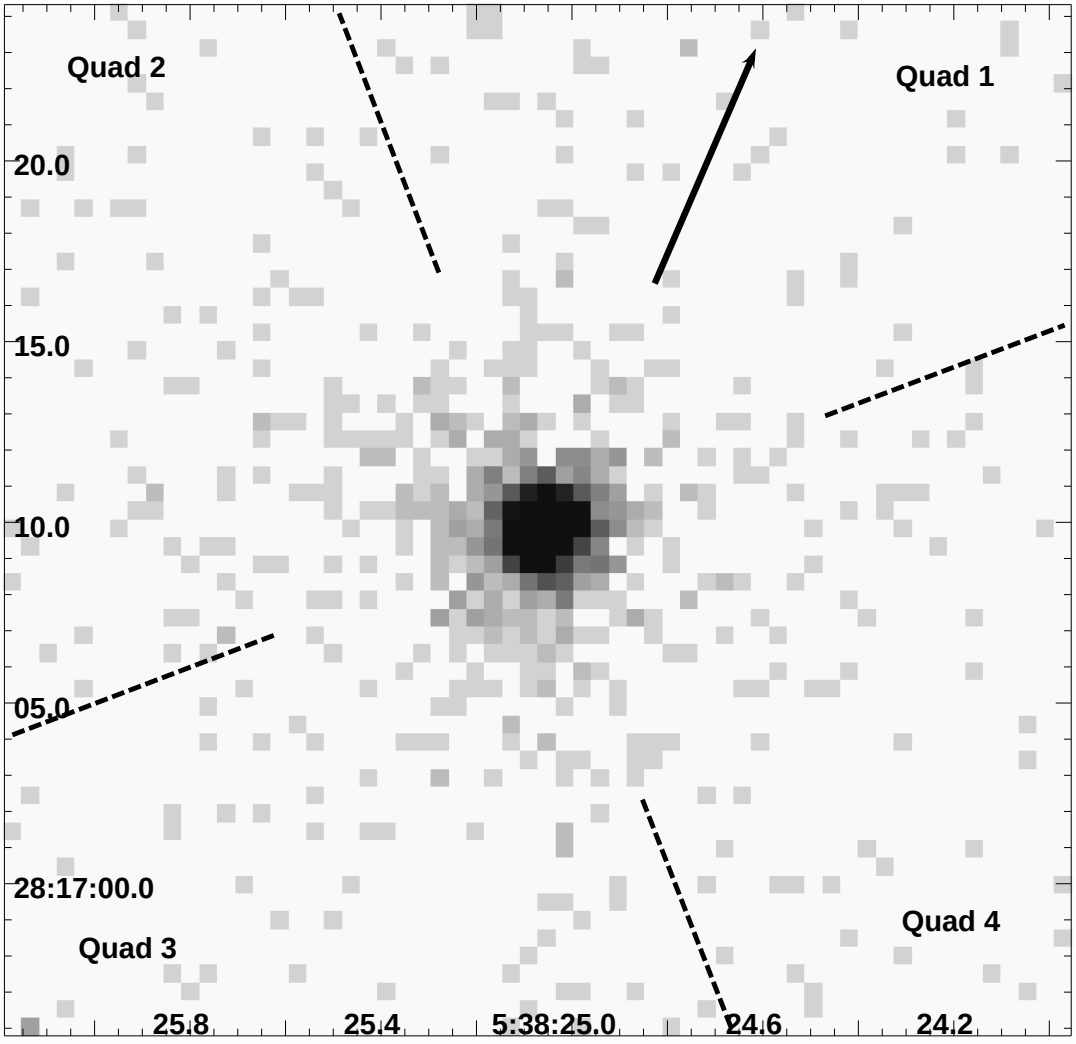

Figure B.2 ACIS-I $0.5 - 8$ keV image. The arrow indicates the pulsar's proper motion direction in its LSR. The dotted lines separate the four quadrants used to measure the azimuthal distribution of the extended emission.

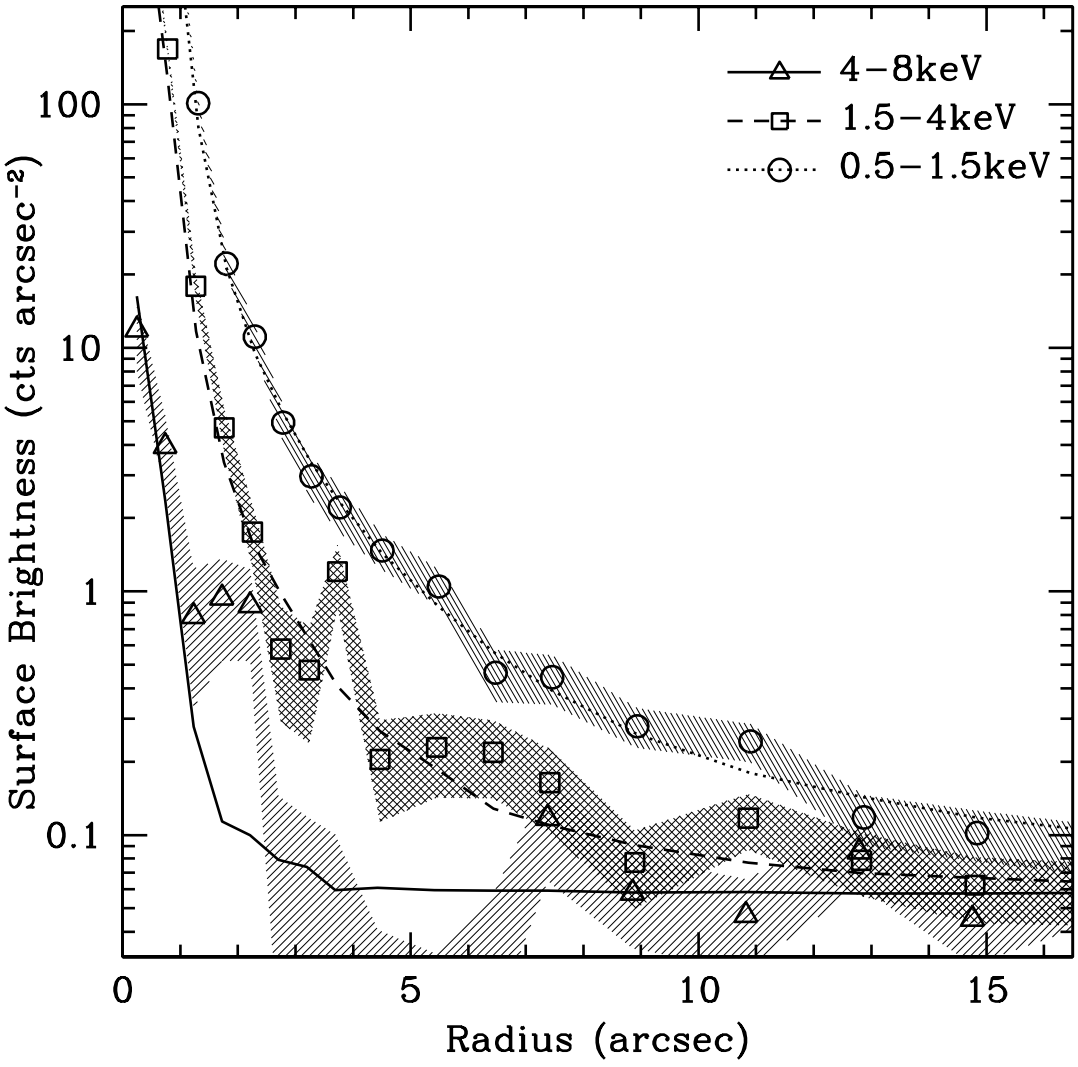

Figure B.3 Observed source (points) and model point source (line) radial count distributions in three energy bands, with the corresponding uncertainties (shaded bands).

Figure B.3 compares the observed surface brightness of the source for the ACIS-I data and the model PSF+background in 3 energy bands. The PSF is simulated using the Chandra Ray-Tracer (ChaRT) and MARX software using the best-fit pulsar

spectrum from a $1''$ radius aperture, in order to minimize any nebular contamination. Although the readout trail is simulated in the model PSF, we excluded two rectangular regions of $1''.5$ wide along the readout trail and beyond $2''.5$ from the point source in our analysis, in order to improve the statistics. The graph suggests that the data and PSF model are well matched for the low energy band, while excess counts appear at several radii for the higher energies.

To investigate the azimuthal distribution of these counts, we show in Figure B.4 the PSFs and observed counts per unit area for the four quadrants (in three energy bands) with Quad 1 along the proper motion direction (see Fig. B.2). The shaded region shows the Poisson uncertainty in the surface brightness measurements. Here we see significant departures from the PSF in all three energy bands. The excesses from $4''-6''$ and $9''-11''$ in Quad 2 in the low energy band represents the candidate 'torus' suggested in Romani & Ng (2003); no corresponding excess is seen in Quad 4. A persistent excess is also seen from $4''-8''$ in Quad 3 of the medium energy band, representing the diffuse emission trailing behind the pulsar.

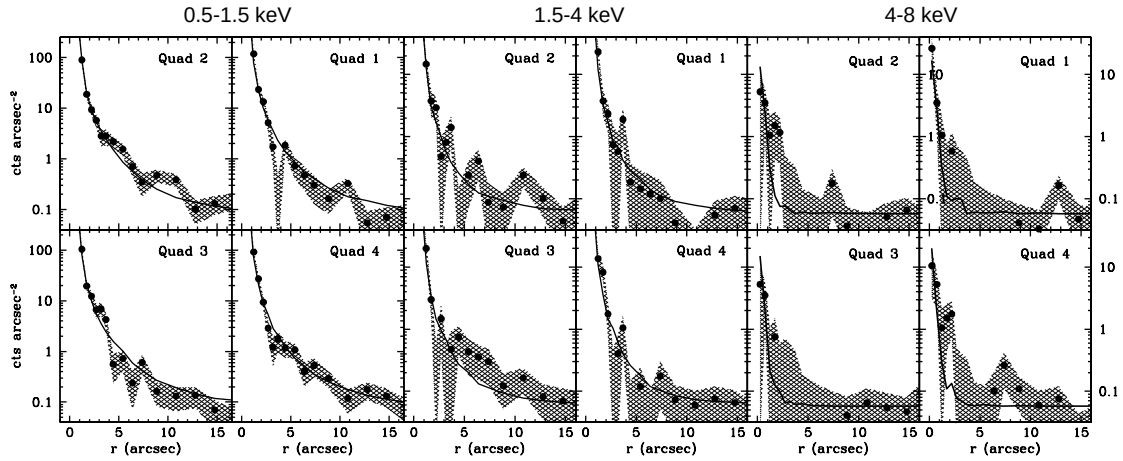

Figure B.4 Surface brightness of the observed source (points) and model point source (lines) for the four quadrants in three energy bands. The y-scale on the left applies to the $0.5-1.5$ keV panel only, while the right scale applies to the other two panels.

Most intriguing, however, is the very significant excess seen in the 4-8 keV band from $2''-4''$ (Fig. B.3). In Figure B.4 we see that this lies in quadrants 2 & 4,

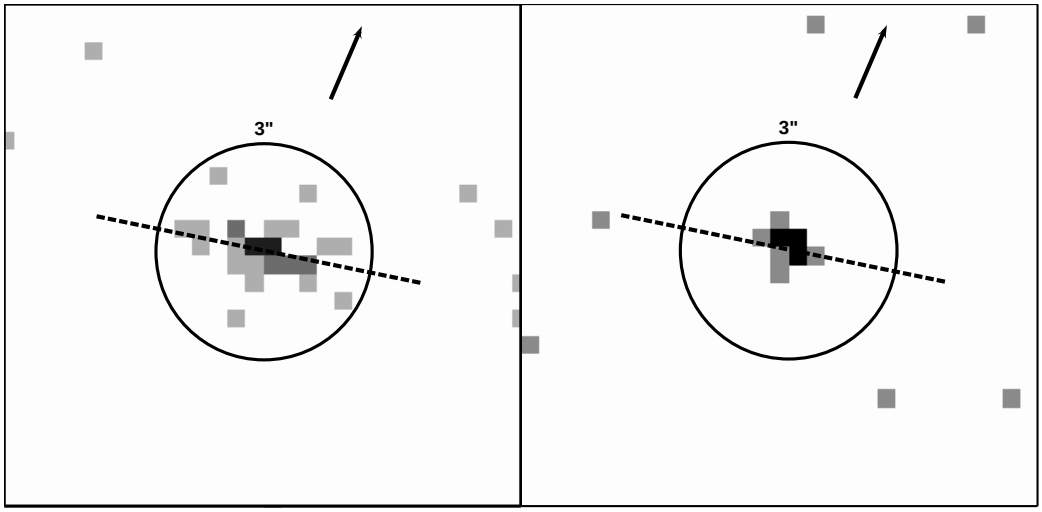

Figure B.5 *Left:* ACIS-I 4-8 keV image with the dashed line showing the best-fit PA of the counts. The arrow indicated the pulsar's proper motion in its LSR. The circle is 3″ in radius. *Right:* Model PSF in the same energy band.

indicating significant structure with a hard spectrum very close to the pulsar. The $4-8$ keV ACIS-I image (Fig. B.5) in fact shows a clear symmetric, almost linear structure extending $\sim 2\farcs5$ from the pulsar. Realizations of the $4-8$ keV model PSF are nearly circular and show no obvious spikes. With only 32 counts, we cannot resolve any details or assign a clear origin for this emission; however, it should be noted that the X-ray images of many other young neutron stars show polar jets or equatorial tori. *If* this is the case for PSR J0538+2817, the symmetry axis could indicate the pulsar spin axis. More importantly, its alignment with the proper motion could constrain the pulsar kick physics (Romani 2005; Ng & Romani 2007, in preparation). In order to measure the PA of the symmetry axis quantitatively, the photon positions were fitted to a straight line passing through the point source. Linear least squares fitting was employed and we obtained the best-fit PA at $79^\circ \pm 4^\circ$.

Although the $4-8$ keV excess is statistically significant, interpretation of such faint compact structure is of course very uncertain. Some information on the pulsar orientation may be gleaned from the radio polarization measurements of Kramer et al. (2003), which suggest a magnetic inclination $\alpha = 95^\circ$ and impact angle $\sigma = 2^\circ$, implying a spin axis inclination of $\zeta = \alpha + \sigma \approx 97^\circ$, i.e. very nearly in the plane of

the sky. This means that both the polar jet interpretation (with the near-orthogonal view implying similar jet/counter-jet fluxes) and the equatorial torus interpretation (with a thin nearly edge-on torus) remain viable. If the extended emission is interpreted as polar jets, then the pulsar spin axis is 78° off the proper motion direction. This is much larger than any of the other PSR/PWN systems. If the axis is the equatorial (torus) plane, then the inferred spin vector is at PA 169°(−11°), i.e. 12° off the velocity vector.

A statistical argument in fact supports the latter interpretation. If the spin axis and proper motion axis are orthogonal in true space, then most observed orientations make the projected angle on the plane of the sky smaller. If they are aligned, the projected angle tends to remain nearly aligned. For completely random orientations, 90% of vectors separated by $0° - 10°$ retain a 2-D angle $\leq 10°$; for vectors separated by $80° - 90°$ only 29% retain $\theta_{2D} \geq 80°$. Thus the observed angle is, *a priori*, $\sim 3\times$ more likely to arise from an aligned system. One additional piece of evidence could be extracted from absolute position angle measurements of the radio polarization (cf. Johnston et al. 2005). Although mode ambiguity allows a 90° jump in the inferred projected field, these authors note that most pulsars appear to emit in the orthogonal mode, which may allow one to discriminate between the jet and torus interpretation.

B.5 Spectral Analysis

We now turn to the spectral analysis of the point source. For the best possible constraints on the spectrum, we have reprocessed both the 18.5 ks cleaned ACIS-S data set and our new 93 ks ACIS-I data with the latest time-dependent gain calibration and charge transfer inefficiency (CTI) correction. The source spectrum was extracted from a 2″ radius aperture with the script `psextract`, and the response matrix files (RMFs) were replaced by the ones built using the tool `mkacisrmf`, which accounts for the CTI. To model the aperture corrections, 10 PSFs with monochromatic energies from 0.5 to 9.5 keV were simulated using ChaRT. The fractional energy encircled by the aperture as a function of energy is obtained, and then used to

correct the ancillary response files (ARFs). As the ACIS-S data suffer 20% pile-up, the CCD pile-up model by Davis (2001) is used in all the spectral fits.

Results from the combined fits of the ACIS-S and ACIS-I datasets are listed in Table B.2. All fits are to the $0.3 - 8$ keV range and the spectral parameter errors reported are projected multidimensional 1σ values. For the uncertainties in flux (and hence stellar radius), as is often the case with low-statistic CCD-quality data, the projected errors are very large due to uncertainties in spectral parameters. Therefore we followed other authors in reporting the single parameter (i.e. 1-D) 1σ error for the flux.

The source spectrum is adequately fitted by an absorbed blackbody. The best-fit $N_{\rm H} = 2.47 \times 10^{21}$ cm^{-2} is lower than the previous *CXO* results, but consistent with the *XMM-Newton* measurements. Comparison with the DM value of 39.7 pc cm $^{-3}$ gives $n_{\rm H}/n_e = 24$, which is relatively large. At the pulsar distance of 1.47 kpc, the best-fit spectral parameters give an effective blackbody radius of $R_\infty^{\rm eff} = 2.19$ km. This is too small to be reconciled with the whole stellar surface, but the flux could be hot $T \sim 2 \times 10^6$ K emission from a small fraction of the stellar surface ($\sim 2.7\%$ for an $R_\infty = 13.1$ km star), possibly due to some heating mechanism such as bombardment of the polar cap regions by relativistic particles from the magnetosphere. The thermal radiation from the neutron star surface could also be described by atmospheric models. Light-element neutron star atmosphere models, such as those dominated by hydrogen, have large Wien excesses. This gives a lower effective temperature and hence larger stellar radius in the fit. We use here a pure H model with $B = 10^{12}$ G (Pavlov, Shibanov, & Zavlin 1992; Zavlin et al. 1996), as the inferred surface magnetic field strength of PSR J0538+2817 is 7×10^{11} G (Anderson et al. 1996). During the fit, the mass of the neutron star is held fixed at $M = 1.4 M_\odot$ and the normalization constant is fixed using the pulsar distance. The best-fit surface temperature and radius are $T_\infty^{\rm eff} = 1.05 \times 10^6$ K and $R_\infty = 11.2$ km. As expected, this model suggests a lower effective temperature covering a large fraction of the neutron star surface for a canonical radius. The fit is statistically slightly worse than that of the blackbody model, but both produce quite acceptable χ^2 values.

The extended emission observed at high energies suggests some flux in the $2''$

Table B.2. Spectral Fits to PSR J0538+2817

		BLACKBODY/ATMOSPHERE				POWER LAW ($\Gamma = 1.5$)		
MODEL	$N_{\rm H}$ (10^{21} cm^{-2})	T_∞ (10^6 K)	R_∞ (km)	Abs. Flux $f_{0.5-8}$ (10^{-13} ergs cm^{-2} s^{-1})	Unabs. Flux $f_{0.5-8}$ (10^{-13} ergs cm^{-2} s^{-1})	Abs. Flux $f_{0.5-8}$ (10^{-13} ergs cm^{-2} s^{-1})	Unabs. Flux $f_{0.5-8}$ (10^{-13} ergs cm^{-2} s^{-1})	χ^2/dof
BB	$2.47^{+0.15}_{-0.14}$	$2.11^{+0.03}_{-0.04}$	2.19 ± 0.01	7.24 ± 0.07	17.4 ± 0.2	...	...	109.7/139
Atm	$2.94^{+0.07}_{-0.06}$	1.05 ± 0.05	11.16 ± 0.02	7.21 ± 0.08	21.4 ± 0.2	...	...	120.7/139
BB+PL	2.50 ± 0.15	$2.10^{+0.04}_{-0.03}$	2.23 ± 0.01	7.15 ± 0.07	17.5 ± 0.2	0.20 ± 0.06	0.24 ± 0.07	99.5/138
Atm+PL	2.95 ± 0.07	$1.06^{+0.06}_{-0.05}$	10.99 ± 0.02	7.14 ± 0.08	21.4 ± 0.2	0.20 ± 0.05	0.24 ± 0.07	110.2/138

aperture is contributed by non-thermal emission. Therefore we tried adding a power law component with fixed $\Gamma = 1.5$ to the models. Although the results are not improved substantially, the non-thermal flux is detected at $> 3\sigma$ level as shown in the table; the effect on the parameters fitted for the thermal component is very small. The best-fit atmosphere+power law model is shown in Figure B.6.

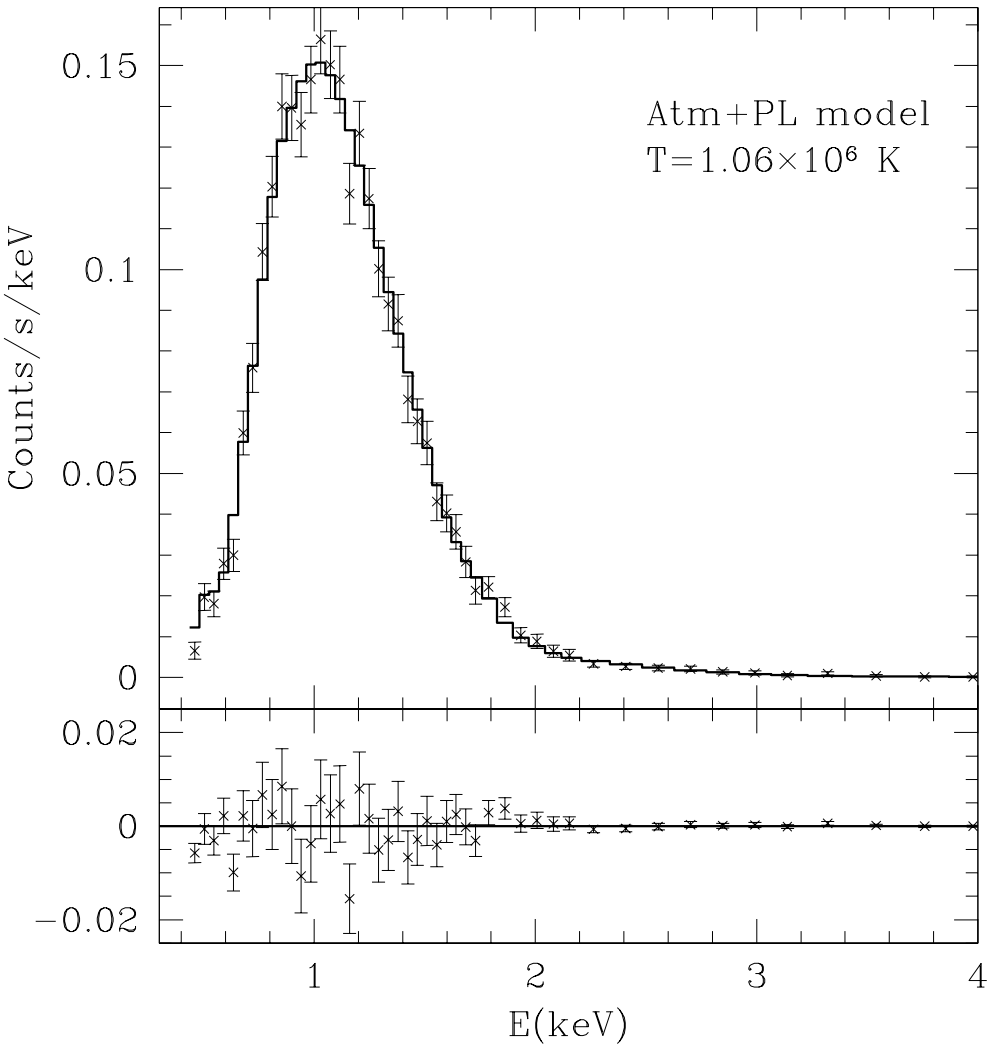

Figure B.6 Point-source spectrum with a pileup-corrected magnetic H model atmosphere + power law spectrum and residuals.

B.6 Discussion

B.6.1 PSR J0538+2817 / S147 Association

The association between PSR J0538+2817 and S147 suggested by Anderson et al. (1996) was based on their positional coincidence and apparent consistency of the distances and ages. In particular, the authors argued that since the pulsar location is near the SNR center, it is unlikely to be a chance association. With our accurate proper motion measurement we can improve this argument. In order to have a quantitative estimate of the chance alignment probability, we did simple Monte Carlo simulations using the model by Faucher-Giguère & Kaspi (2006). Following these authors, we assume the pulsars are born in the Galactic plane with the galactocentric radial distribution from Yusifov & Küçük (2004) and exponential distribution in the scale height, and with birth velocities distributed as a two-component Gaussian model. Acceleration due to Galactic potential was ignored for simplicity. Our results show that in 2×10^5 yr, the most extreme age estimate for S147, only 1 pulsar in 2×10^7 would have a chance passage within $8'$ of the S147 center. We also applied the Maxwellian pulsar velocity distribution suggested by Hobbs et al. (2005), obtaining nearly identical result. With a Galactic neutron star birthrate of 2.8 per century (Faucher-Giguère & Kaspi 2006) and a radio beaming factor of $\sim 1/5$, the probability of finding a random, unassociated radio pulsar younger than 1 Myr which has passed within $8'$ of the SNR center is $\sim 3 \times 10^{-4}$. This estimate is a conservative upper limit to the probability: we believe the true age of S147 is considerably younger, and the high X-ray temperature of PSR J0538+2817 also implies a younger $\leq 10^5$ yr age. Thus a more realistic chance probability is $\geq 10\times$ smaller. To conclude, PSR J0538+2817 is almost certainly associated with S147 and this implies a SNR distance of $\sim$ 1.5 kpc. This value is substantially larger than some previous estimates (e.g. Kundu et al. 1980), thus it calls into question some papers that assume a much closer distance to S147 (e.g. Phillips et al. 1981; Sallmen & Welsh 2004).

B.6.2 S147 as a Cavity Explosion

In standard SNR evolution, the shell radius in the Sedov-Taylor phase is given by $R_{\rm SNR} = 0.31(E_{51}/n_0)^{1/5}t^{2/5}$ pc (e.g. van der Swaluw 2001), where the explosion energy is $E_0 = 10^{51}E_{51}$ ergs, age in t years and external medium of density n_0 cm^{-3}. The observed angular size of S147 $\theta = 83'$ (Sofue et al. 1980) corresponds to a physical radius of 35 pc at 1.47 kpc. For an age of 30 kyr (Kramer et al. 2003), this requires a very energetic explosion of $E_{51} = 20\ n_0$. This suggests S147 probably occurred in a low density stellar wind bubble, likely evacuated by the progenitor star in a WR phase (Kramer et al. 2003; Gvaramadze 2006). Hence the SNR had a long free-expansion phase, only passing to the Sedov-Taylor phase when it reached the cavity boundaries at relatively large radius. This scenario receives further support from the observed low expansion velocity of S147 at 80 km s^{-1} (Kirshner & Arnold 1979). Note that the progenitor's proper motion can make the wind bubble asymmetric, with the cavity extending further behind the star (Gvaramadze 2006). Density gradients in the external medium can also enhance this asymmetry. Indeed gas and dust surveys suggest that the medium to the South of S147 is denser and the shell is flattened with the brightest filaments on this side. Supporting this, the optical observations by Lozinskaya (1976) provides some hint that the expansion rate is faster in the northern half of S147. Thus we generally expect the 'geometrical center' to lie somewhat North of the true explosion site.

B.6.3 Birth-site of the Progenitor

With the inferred distance to S147, it is possible to search for the birth-site of its parent star. O and B stars are the direct progenitors of neutron stars and the minimum mass for supernova explosion is $\sim 8M_{\odot}$. These massive stars are generally formed in OB associations and young open clusters. With their short < 50 Myr lifetimes they do not travel far from the birth-sites. Typical peculiar velocities are a few km s^{-1}; for 10 km s^{-1}, we expect the progenitor to travel ≤ 500 pc. We compiled a list of open clusters and OB associations from the catalogs including Ruprecht, Balazs, & White (1983), Mel'nik & Efremov (1995), Dias et al. (2002)

Table B.3. Open Clusters younger than 50 Myr within 500 pc of S147.

Name	d (kpc)	θ (°)	r (pc)	N*	Age (Myr)
NGC 1960 (M36)	1.32	6.4	217	60	42
OB Gem 1	1.34	9.9	276	···	< 5
NGC 2175	1.63	10.0	311	60	9
Stock 8	1.82	7.1	405	40	41
NGC 2331	1.33	19.3	488	30	?

and Kharchenko et al. (2005) and found only four candidates younger than 50 Myr with a nominal distance to S147 of < 500 pc (Table B.3). Directions to potential birth-sites are shown in Figure B.1.

With a 3-D spatial separation of only 220 pc from S147, NGC 1960 (M36) is the closest candidate. This is a relatively massive ~ 40 Myr-old cluster (Kharchenko et al. 2005) and we consider it the prime candidate birth-site. If correct, the progenitor traveled from this cluster at PA $\sim 175°$ with a 3-D space velocity of $\sim 5(M/10M_{\odot})^{2.5}$ km s^{-1}. We see no evidence in gas maps or the SNR shell that the progenitor wind has disturbed the denser cloud to the South. This and the blowouts of the SNR to the North argue against Gem 1 or NGC 2175 as the parent cluster. Stock 8 to the North remains viable, but is distant at ≥ 400 pc and less massive. Finally, it is intriguing to note that the 5$^{\rm th}$ nearest young cluster, the very poorly studied NGC 2331, lies precisely in the direction of the largest (Eastern) extension of the SNR shell; the Hα shell here extends 40% ($\sim 35'$) further than the main shock front, with wispy emission present up to 10′ further in this direction. It is tempting to associate this blowout with a stellar wind trail extending along the path to NGC 2331, but this cluster appears to be relatively low mass and may be too old, with no remaining B stars.

B.6.4 Explosion Site

From the precise pulsar proper motion, we know that the supernova explosion must have occurred along the line in Figure B.1 with the arrowhead at the present pulsar position. The explosion site is determined by the true age of S147/PSR J0538+2817; tick marks on the line indicate 20, 40 and 60 kyr ages. The simplest interpretation is to infer birth at the closest approach to the geometrical center 36 kyr ago and assign an uncertainty of $\sim 8'/57.6$ mas yr^{-1} = 8 kyr. However, if we can define a second axis for the progenitor motion, we can obtain a more precise age. If we adopt the symmetry axis suggested by Gvaramadze (2006, solid lines in Fig. 1) then the birth-site is to the NW of the geometrical center and the intersection with the proper motion suggests a SNR age near 20 kyr. Given the rather irregular nature of the Northern half of the remnant and the argument that the explosion should be south of the geometrical center, we do not find this axis convincing. The axis to NGC 2331 intersects at a more plausible explosion age of 30 kyr.

If however we adopt NGC 1960 as the birth-site, then a explosion somewhat south of (in front of) the geometrical center becomes natural. Without a blowout identifying an entry site, we cannot set a precise axis, but the path should pass close to the geometric center, implying an intersection with the proper motion vector at ≤ 60 kyr. Our conclusion is that the best estimate of the SNR age is 40 kyr with a maximum plausible range of $20 - 60$ kyr. This is slightly older than the estimate of Kramer et al. (2003). However, the inferred initial spin period of PSR J0538+2817 is not significantly changed. Assuming magnetic spin-down with constant braking index $n = 3$, the initial spin period is given by

$$P_0 = P\left(1 - \frac{n-1}{2}\frac{\tau}{\tau_c}\right)^{\frac{1}{n-1}} ,$$

where τ and τ_c are the kinematic and characteristic ages of the pulsar respectively. We obtained $P_0 = 138 \pm 2.3$ ms; the kinematic age of the pulsar is indeed much smaller than its spin-down age.

B.6.5 Spin-velocity Alignment

Only a few pulsars have estimated initial spin periods; the value for PSR J0538+2817 is the longest among these. Of course, the high space velocity of the pulsar argues for a strong birth kick. Note that with the large parallax distance to the pulsar, the binary break-up scenario described by Gvaramadze (2006) is now even more improbable. If one further accepts a progenitor origin in the Galactic plane near NGC 1960, then the pulsar's present rapid return to the plane further supports a birth kick uncorrelated with its parent's motion.

These considerations make a comparison of this pulsar's kick and spin direction particularly appealing. Unfortunately the morphology of the extended structure near the pulsar is not clear enough to define a definitive spin axis and thus weakens this system's ability to cleanly test the spin-kick models. However, we can turn the question around: if the mechanism that seems to cause spin and kick alignment in other young pulsars acts on PSR J0538+2817, do we expect its spin to be more nearly aligned or orthogonal? To retain a slow spin with a large kick velocity, the net kick vector must be nearly radial, applying little torque to the star.

We have performed a series of simulation of neutron star birth kicks in a range of models where a single thrust is applied to the surface at fixed angle as the proto-neutron star cools, with amplitude proportional to the driving neutrino luminosity (Ng & Romani 2007, in preparation). Comparing with the set of all neutron stars with initial spin and/or speed measurements, we have found (for several models of proto-neutron star evolution and neutrino cooling) the best-fit parameter distributions for the neutron star pre-kick spin, the kick amplitude, normal direction and duration that reproduce the observed pulsar spin and speed distributions. For these parameters (fixed by a set of ~ 50 other pulsars) we can ask whether a pulsar with slow initial spin like PSR J0538+2817 is more likely to have its birth velocity and spin vectors aligned or orthogonal. The simulations find that for $P \sim 140$ ms, the aligned case is produced $30 - 90\times$ more frequently than the orthogonal cases, even though faster spin pulsars do not always show good alignment. Ng & Romani (2007, in preparation) discuss the significance of this result for improving kick constraints.

B.6.6 Pulsar Thermal Emission

From the X-ray spectral results, the neutron star atmosphere fit gives an effective surface temperature of $\gtrsim 10^6$ K. This matches well to the standard cooling curve for the pulsar age of $\lesssim 40$ kyr (cf. Fig. 6 in McGowan et al. 2003). Comparing with the cooling models of Yakovlev & Pethick (2004) we see that our best-fit 1.05×10^6 K surface agrees well with a typical cooling model at age 25 kyr. Even so-called slow cooling neutron stars (low mass stars, with crustal neutron pairing and/or accreted low Z envelopes) drop very rapidly below $T_\infty = 10^6$ K after 10^5 yr. Thus if we interpret the thermal emission as full surface emission, it seems impossible for PSR J0538+2817 to be as old as its characteristic age. In contrast, its thermal surface emission is quite consistent with its young ~ 30 kyr kinematic age, requiring no direct Urca process or any other exotic cooling mechanisms.

XMM observations find a low 18% soft X-ray pulsation with a very broad profile (McGowan et al. 2003). These authors interpret this as a hot polar cap from a nearly aligned rotator (polar cap axis and rotation axis both close to the line of sight). This seems at odds with the radio polarization and PWN data, so a more natural interpretation might be emission from a gradual temperature variation across a light element surface, perhaps caused by magnetic dipole variation in the thermal conductivity (Greenstein & Hartke 1983).

If interpreted as a re-heated cap emission the thermal flux would be a surprisingly large 1% of the full spin-down power. On the other hand, the non-thermal emission from the PSR/PWN system as a whole is close to that expected. In an aperture of radius 15″, the observed count rate in the $2-10$ keV band is 5×10^{-3} cts s^{-1}. After subtracting the background and thermal emission from the pulsar, the non-thermal contribution gives 2.8×10^{-3} cts s^{-1}. For a power law of $\Gamma = 1.5$, this converts to the luminosity of $10^{31.26}$ ergs s^{-1}. Possenti et al. (2002) found an empirical relation between the X-ray flux in the $2-10$ keV band and spin-down luminosity: $\log L_{\mathrm{X},(2-10)} = 1.34 \log L_{\mathrm{sd}} - 15.34$. For the case of PSR J0538+2817, the spin-down luminosity derived from the radio parameters (Anderson et al. 1996) is $L_{\mathrm{sd}} = 5 \times 10^{34}$ ergs s^{-1}, which predicts an X-ray luminosity of $L_{\mathrm{X},(2-10)} = 10^{31.2}$ ergs s^{-1}, very close to the observed value.

B.6.7 Conclusions

We have reported VLBA astrometric measurements and *Chandra* ACIS-I observation of PSR J0538+2817. The VLBA astrometry gives the pulsar distance of $1.47^{+0.42}_{-0.27}$ kpc with a precise model independent transverse velocity $V_{\perp} = 400^{+114}_{-73}$ km s^{-1}. These observations strengthen the association with S147 and suggest NGC 1960 as plausible birth-site for the progenitor star. It seems likely that the supernova occurred in a stellar wind bubble some 40 kyr ago. The X-ray observations of the pulsar show that the thermal point source has a high temperature consistent with the 40 kyr age and imply that it was the source of the observed SNR. Our deep *Chandra* pointing reveals extended emission around the pulsar with a very compact symmetric structure observed in the $4 - 8$ kev range. The overall PWN flux is broadly consistent with the emission expected from this relatively low $\dot{E}$ spin-down pulsar, but the physical origin of the hard emission in these innermost regions is not clear. Statistical arguments suggest that the symmetric emission is an equatorial structure, viewed edge-on, so that the pulsar spin and motion are roughly aligned as for many other young pulsars. However, further observations are needed to reach definitive conclusions.

Bibliography

Aharonian, F., et al. 2005, A&A, 432, L9

Anderson, S. B., Cadwell, B. J., Jacoby, B. A., Wolszczan, A., Foster, R. S., & Kramer, M. 1996, ApJ, 468, L55

Anderson, J., & King, I. R. 1999, PASP, 111, 1095

Anderson, J., & King, I. R. 2000, PASP, 112, 1360

Anderson, J., & King, I. R. 2003, PASP, 115, 113

Arras, P., & Lai, D. 1999a, ApJ, 519, 745

Arras, P., & Lai, D. 1999b, Phys. Rev. D, 60, 043001

Arzoumanian, Z., Chernoff, D. F., & Cordes, J. M. 2002, ApJ, 568, 289

Aschenbach, B., Egger, R., & Trümper, J. 1995, Nature, 373, 587

Baade, W., & Zwicky, F. 1934, Phys. Rev., 45, 138

Baggett, S., et al. 2002, in HST WFPC2 Data Handbook, v. 4.0, ed. B. Mobasher (Baltimore: STScI)

Bailes, M. 1989, ApJ, 342, 917

Blaauw, A. 1961, Bull. Astron. Inst. Netherlands, 15, 265

Blondin, J. M., Chevalier, R. A., & Frierson, D. M. 2001, ApJ, 563, 806

Blondin, J. M., & Mezzacappa, A. 2006, ApJ, 642, 401

Bock, D. C.-J., & Gvaramadze, V. V. 2002, A&A, 394, 533

Boersma, J. 1961, Bull. Astron. Inst. Netherlands, 15, 291

Brisken, W. F., Benson, J. M., Goss, W. M., & Thorsett, S. E. 2002, ApJ, 571, 906

Brisken, W. F., Carrillo-Barragan, M., Kurtz, S., & Finley, J. P. 2006, ApJ, 652, 554

Brisken, W., Thorsett, S. E., Golden, A., & Goss, W. M. 2003, ApJ, 593, L89

Burrows, A., Klein, D., & Gandhi, R. 1992, Phys. Rev. D, 45, 3361

Camilo, F., Ransom, S. M., Gaensler, B. M., Slane, P. O., Lorimer, D. R., Reynolds, J., Manchester, R. N., & Murray, S. S. 2006, ApJ, 637, 456

Caraveo, P. A., & Mignani, R. P. 1999, A&A, 344, 367

Castor, J., McCray, R., & Weaver, R. 1975, ApJ, 200, L107

Chadwick, P. M., et al. 1997, in Proc. 26th Cosmic Ray Conf., 3, 189

Chatterjee, S., et al. 2005, ApJ, 630, L61

Chevalier, R. A. 2005, ApJ, 619, 839

Cordes, J. M., & Chernoff, D. F. 1998, ApJ, 505, 315

Cordes, J. M., & Lazio, T. J. W. 2002, preprint (astro-ph/0207156)

Cordes, J. M., Romani, R. W., & Lundgren, S. C. 1993, Nature, 362, 133

Davis, J. E. 2001, ApJ, 562, 575

Dehnen, W., & Binney, J. J. 1998, MNRAS, 298, 387

Deshpande, A. A., Ramachandran, R., & Radhakrishnan, V. 1999, A&A, 351, 195

Dewey, R. J., & Cordes, J. M. 1987, ApJ, 321, 780

Dodson, R., & Golap, K. 2002, MNRAS, 334, L1

Dodson, R., Legge, D., Reynolds, J. E., & McCulloch, P. M. 2003, ApJ, 596, 1137

Dodson, R., Lewis, D., McConnell, D., & Deshpande, A. A. 2003, MNRAS, 343, 116

Drew, J. E., et al. 2005, MNRAS, 362, 753

Dias, W. S., Alessi, B. S., Moitinho, A., & Lepine, J. R. D. 2002, A&A, 389, 871

Efron, B., & Tibshirani, R. J. 1993, An Introduction to the Bootstrap (New York: Chapman and Hall)

Faucher-Giguère, C.-A., & Kaspi, V. M. 2006, ApJ, 643, 332

Fich, M., Blitz, L., & Stark, A. 1989, ApJ, 342, 272

Frater, R. H., Brooks, J. W., & Whiteoak, J. B. 1992, JEEE, 12, 103

Fryer, C., Burrows, A., & Benz, W. 1998, ApJ, 496, 333

Fryer, C. L., 2004, ApJ, 601, L175

Fryer, C. L., & Kusenko, A. 2006, ApJS, 163, 335

Fuller, G. M., Kusenko, A., Mocioiu, I., Pascoli, S. 2003, Phys. Rev. D, 68, 103002

Gaensler, B. M., Chatterjee, S., Slane, P. O., van der Swaluw, E., Camilo, F., & Hughes, J. P. 2006, ApJ, 648, 1037

Gaensler, B. M., van der Swaluw, E., Camilo, F., Kaspi, V. M., Baganoff, F. K., Yusef-Zadeh, F., & Manchester, R. N. 2004, ApJ, 616, 383

Giacani, E. B., Frail, D. A., Goss, W. M., & Vietes, M. 2001, AJ, 121, 3133

Gilmozzi, R, Ewald, S., & Kinney, E. 1995, WFPC2 Instrument Science Report 95-02 (Baltimore: STScI)

Gold, T. 1968, Nature, 218, 731

Gotthelf, E. V. 2001, in AIP Conf. Proc. 586, 20th Texas Symposium on Relativistic Astrophysics, ed. J. C. Wheeler & H. Martel (Melville: AIP), 513

Gotthelf, E. V. 2003, ApJ, 591, 361

Gotthelf, E. V., Halpern, J. P., & Dodson, R. 2002, ApJ, 567, L125

Gotthelf, E. V., Helfand, D. J., & Newburgh, L. 2006, ApJ, in press

Greenstein, G., & Hartke, G. J. 1983, ApJ, 271, 283

Gvaramadze, V. V. 2002, in ASP Conf. Ser. 271, Neutron Stars in Supernova Remnants, ed. P. O. Slane & B. M. Gaensler (San Francisco: ASP), 23

Gvaramadze, V. V. 2006, A&A, 454, 239

Harrison, E. R., & Tademaru, E. 1975, ApJ, 201, 447

Helfand, D. J., Gotthelf, E. V., & Halpern, J. P. 2001, ApJ, 556, 380

Helfand, D. J., Taylor, J. H., & Manchester, R. N. 1977, ApJ, 213, L1

Hessels, J. W. T., Roberts, M. S. E., Ransom, S. M., Kaspi, V. M., Romani, R. W., Ng, C.-Y., Freire, P. C. C., Gaensler, B. M. 2004, ApJ, 612, 389

Hester, J. J. 2000, BAAS, 32, 1542

Hester, J. J., et al. 2002, ApJ, 577, L49

Hewish, A., Bell, S. J., Pilkington, J. D. H., Scott, P. F., & Collins, R. A. 1968, Nature, 217, 709

Hobbs G., Lyne A. G., Kramer, M., Martin, C. E., & Jordan, C. A. 2004, MNRAS, 353, 1311

Hobbs, G., Lorimer, D. R., Lyne, A. G., & Kramer, M. 2005 MNRAS, 360, 974

Hughes, J. P., Slane, P. O., Park, S., Roming, P. W. A., & Burrows, D. N. 2003, ApJ, 591, L139

Janka, H.-Th., Buras, R., Kifonidis, K., Plewa, T., & Rampp, M. 2003, in Proc. of the ESO/MPA/MPE Workshop, From Twilight to Highlight: The Physics of Supernovae, ed. W. Hillebrandt & B. Leibundgut (Berlin: Springer), 39

Janka, H.-Th., Buras, R., Kifonidis, K., Rampp, M., & Plewa, T. 2004, in Stellar Collapse, ed. C. L. Fryer (Dordrecht: Kluwer), 66

Janka, H.-Th., Scheck, L., Kifonidis, K., Müller, E., & Plewa, T. 2005, in ASP Conf. Ser. 332, The Fate of the Most Massive Stars, ed. R. Humphreys & K. Stanek (San Francisco: ASP), 372

Johnston, S., Hobbs, G., Vigeland, S., Kramer, M., Weisberg, J. M., & Lyne, A. G. 2005 MNRAS, 364, 1397

Johnston, S. Lyne, A. G., Manchester, R. N., Kniffen, D. A., D'Amico, N., Lim, J., & Ashworth, M. 1992, MNRAS, 255, 401

Johnston, S., Nicastro, L., & Koribalski, B. 1998, MNRAS, 297, 108

Kaplan, D. L., van Kerkwijk, M. H., & Anderson, J. 2002, ApJ, 571, 447

Kharchenko, N. V., Piskunov, A. E., Roeser, S., Schilbach, E., & Scholz, R.-D. 2005, A&A, 438, 1163

Kifune, T., et al. 1995, ApJ, 438, L91

Kirshner, R. P., & Arnold, C. N. 1979, ApJ, 229, 147

Komissarov, S. S., & Lyubarsky, Y. F. 2003, MNRAS, 344, L93

Koribalski, B., Johnston, S., Wiesberg, J., & Wilson, W. 1995, ApJ, 441, 756

Kotake, K., Sato, K., & Takahashi, K. 2006, Rep. Prog. Phys. 69, 971

Kothes, R., Reich, W., & Uyaniker, B. 2006, ApJ, 638, 225

Kramer, M., Lyne, A. G., Hobbs, G., Löhmer, O., Carr, P., Jordan, C., & Wolszczan, A. 2003, ApJ, 593, L31

Krishnomohan, S., & Downs, G. S. 1983, ApJ, 265, 372

Krist, J. 1995, in ASP Conf. Ser. 77, Astronomical Data Analysis Software and Systems IV, ed. R. A. Shaw, H. E. Payne, & J. J. E. Hayes (San Francisco: ASP), 349

Kundu, M. R., Angerhofer, P. E., Fürst, E., & Hirth, W. 1980, A&A, 92, 225

Kusenko, A. 2004, Int. J. Mod. Phys. D, 13, 2065

Lai, D., Chernoff, D. F., & Cordes, J. M. 2001, ApJ, 549, 1111

Lozinskaya, T. A. 1976, Soviet Ast., 20, 19

Lyne, A. G., & Manchester, R. N. 1988, MNRAS, 234, 477

Lyne, A. G., Pritchard, R. S., Graham-Smith, F., & Camilo, F. 1996, Nature, 381, 497

Maeder, A. 1981, A&A, 102, 401

Manchester, R. N., Mar, D. P., Lyne, A. G., Kaspi, V. M., & Johnston, S. 1993, ApJ, 403, L29

Manchester, R. N., & Taylor, J. H. 1977, Pulsars (San Francisco: Freeman)

McAdam, W., Osborne, J., & Parkinson, M. 1993, Nature, 361, 516

McGowan, K. E., Kennea, J. A., Zane, S., Córdova, F. A., Cropper, M., Ho, C., Sasseen, T., & Vestrand, W. T. 2003, ApJ, 591, 380

McGowan, K. E., Zane, S., Cropper, M., Kennea, J. A., Córdova, F. A., Ho, C., Sasseen, T., & Vestrand, W. T. 2004, ApJ, 600, 343

Migliazzo, J. M., Gaensler, B. M., Backer, D. C., Stappers, B. W., van der Swaluw, E., & Strom, R. G. 2002, ApJ, 567, L141

Mignani, R. P., Caraveo, P. A., & de Luca, A. 2000, in STSci Symp. Ser. 14, A Decade of HST Science, ed. M. Livio, K. Noll, & M. Stiavelli (Cambridge: Cambridge Univ. Press), 65

Mel'nik, A. M., & Efremov, Y. N. 1995, Astron. Lett., 21, 10

Mori, K., Tsunemi, H., Miyata, E., Baluta, C. J., Burrows, D. N., Garmire, G. P., & Chartas, G. 2001, in ASP Conf. Ser. 251, New Century of X-Ray Astronomy, ed. H. Inoue & H. Kunieda (San Francisco: ASP), 576

Murray, S. S., Slane, P. O., Seward, F. D., Ransom, S. M., & Gaensler, B. M. 2002, 568, 226

Muslimov, A., & Harding, A. K. 2003, ApJ, 588, 430

Nardi, E., & Zuluaga, J. I. 2001, ApJ, 549, 1076

Ng, C.-Y., & Romani, R. W. 2004, ApJ, 601, 479

Ng, C.-Y., & Romani, R. W. 2006, ApJ, 644, 445

Ng, C.-Y., Romani, R. W., Brisken, W. F., Chatterjee, S., & Kramer, M. 2007, ApJ, in press

Nicastro, L., Johnston, S., & Koribalski, B. 1996, A&A, 306, L49

Ord, S. M., Bailes, M., & van Straten, W. 2002, ApJ, 574, L75

Pavlov, G. G., Kargaltsev, O. Y., Sanwal, D., & Garmire, G. P. 2001, ApJ, 554, L189

Pavlov, G. G., Sanwal, D., Garmire, G. P., Zavlin, V. E., Burwitz, V., & Dodson, R. G. 2000, BAAS, 32, 733

Pavlov, G. G., Shibanov, Yu. A., & Zavlin, V. E. 1992, MNRAS, 253, 193

Pavlov, G. G., Teter, M., Kargeltsev, O., & Sanwal , D. 2003, ApJ, 591, 1157

Pavlov, G. G., Zavlin, V. E., & Sanwal, D. 2002, in Proc. of 270th Heraeus Symp, 273

Pelling, R. M., et al. 1987, ApJ, 319, 416

Phillips, A. P., Gondhalekar, P. M., & Blades, J. C. 1981, MNRAS, 195, 485

Possenti, A., Cerutti, R., Colpi, M., & Mereghetti, S. 2002, A&A, 387, 993

Press, W. H., Flannery, B. P., Teukolsky, S., & Vetterling, W. 1992, Numerical Recipes (Cambridge: Cambridge Univ. Press)

Radhakrishnan, V., & Shukre, C. S. 1986, Ap&SS, 118, 329

Rampp, M., & Janka, H.-T. 2002, A&A, 396, 361

Rees, M. J., & Gunn. J. E. 1974, MNRAS, 167, 1

Reynolds, S. P. 1985, ApJ, 291, 152

Romani, R. W. 1996, ApJ, 470, 469

Romani, R. W. 2005, in ASP Conf. Ser. 328, Binary Radio Pulsars, ed. F. A. Rasio & I. H. Stairs (San Francisco: ASP), 337

Romani, R. W., & Ng, C.-Y. 2003, ApJ, 585, L41

Romani, R. W., Ng, C.-Y., Dodson, R., & Brisken, W. 2005, ApJ, 631, 480

Romani, R. W., & Yadigaroglu, I.-A. 1995, ApJ, 438, 314

Ruprecht, J., Balazs, B., & White, R. E. 1983, Soviet Ast., 27, 358

Sallmen, S., & Welsh, B. Y. 2004, A&A, 426, 555

Scheck, L., Kifonidis, K., Janka, H.-Th., & Müller, E. 2006, A&A, 457, 963

Scheck, L., Plewa, T., Janka, H.-Th., Kifonidis, K., & Müller, E. 2004, Phys. Rev. Lett., 92, 011103

Serafimovich, N. I., Shibanov, Yu. A., Lundqvist, P., & Sollerman, J. 2004, A&A, 425, 1041

Shapiro, S. L., & Teukolsky, S. A. 1983, Black Holes, White Dwarfs, & Neutron Stars (New York: John Wiley & Sons)

Shibata, S, Tomatsuri, H, Shimanuki, M, Saito, K, & Mori, K. 2003, MNRAS, 346, 841

Socrates, A., Blaes, O., Hungerford, A., & Fryer, C. L. 2005, ApJ, 632, 531

Sofue, Y., Fürst, E., & Hirth, W. 1980, PASJ, 32, 1

Souvageot, J. L., Ballet, J., & Rothenflug, R. 1990, A&A, 227, 183

Spruit, H., & Phinney, E. S. 1998, Nature, 393, 139

Sun, X., et al. 1996, in X-Ray and Gamma-Ray Observations of the Pulsar PSR J0538+2817, ed. H. U. Zimmerman, J. Trümper & H. Yorke (MPE Rep. 263; Garching: MPE), 195

Sun, X. H., & Han, J. L. 2004, MNRAS, 350, 232

Tauris, T. M., & Takens, R. J. 1998, A&A, 330, 1047

Thompson, C., & Duncan, R. C. 1993, ApJ, 408, 194

Thorsett, S. E., Benjamin, R. A., Brisken, Walter F., Golden, A., & Goss, W. M. 2003, ApJ, 592, L71

van der Swaluw, E. 2001, PhD Thesis, Proefschrift Universiteit Utrecht

van der Swaluw, E., Achterberg, A., Gallant, Y. A., & Keppens, R. 2003, A&A, 397, 913

van der Swaluw, E., Achterberg, A., Gallant, Y. A., & Toth, G. 2001 A&A, 380, 309

van der Swaluw, E., Downes, T. P., & Keegan, R. 2004, A&A, 420, 937

van der Swaluw, E., & Wu, Y. 2001, ApJ, 555, L49

Wang, Q. D., Gotthelf, E. V., Chu, Y.-H., & Dickel, J. R. 2001, ApJ, 559, 275

Wang, C., Lai, D., & Han, J. L. 2006a, ApJ, 639, 1007

Wang, C., Lai, D., & Han, J. L. 2006b, ApJ, in press

Wang, Q. D., & Gotthelf, E. V. 1998, ApJ, 494, 623

Weisskopf, M. C., et al. 2000, ApJ, 536, L81

Wychoff, S., & Murray, C. A. 1977, MNRAS, 180, 717

Yakovlev, D. G., & Pethick, C. J. 2004, ARA&A, 42, 169

Yusifov, I., & Küçük, I. 2004, A&A, 422, 545

Zavlin, V. E., Pavlov, G. G., & Shibanov, Yu. A. 1996, A&A, 315, 141

Zou, W. Z., Hobbs, G., Wang, N., Manchester, R. N., Wu, X. J., & Wang, H. X. 2005, MNRAS, 362, 1189